STATE DEPENDANCE OF QUANTUM RATCHETS

By

JIATING NI

Bachelor of Arts/Science in Physics
Zhejiang Normal University
Jinhua, Zhejiang, China
2005

Master of Arts/Science in Physics
Hangzhou Normal University
Hangzhou, Zhejiang, China
2009

Submitted to the Faculty of the
Graduate College of the
Oklahoma State University
in partial fulfillment of
the requirements for
the Degree of
DOCTOR OF PHILOSOPHY
May, 2017

STATE DEPENDANCE OF QUANTUM RATCHETS

Dissertation Approved:

Gil Summy

Dissertation Adviser

John W. Mintmire

Albert T. Rosenberger

Wouter Hoff

ACKNOWLEDGEMENTS

I would like to begin by expressing my gratitude to my advisor Gil Summy from the bottom of my heart. Gil is a very nice advisor with great patience. He gives his students enough freedom to learn from the practice and always encourage us to try something new with a creative way. In the lab it has always amazed and inspired me how Gil does find a way to simply make things work.

I would like to thank my committee members, Prof. John Mintmire, Prof. Albert Rosenberger, and Prof. Wouter Hoff for their time, help and advice. I would also like to thank our collaborators, Dr. Sandro Wimberger from University of Heidelberg Germany and Prof. Mario Borunda from OSU. They give me a lot of suggestions which are very helpful.

Without the love and continued support from my father Yonghui Ni and mother Lijuan Chen, I would not be where I am today. Another important person who has supported and encouraged me throughout this time is my husband Yu Fu. I appreciate all of them for what they did for me.

I would like to thank the physics faculty for helping me pursue my research. Especially, I wish to thank Prof. John Mintmire, our head of the department, Prof. Robert Hauenstein, our former graduate coordinator, and Prof. Albert Rosenberger, our current graduate coordinator, for their support towards achieving the degree.

During my stay at OSU I worked with several incredible people. Rajendra Shrestha is an excellent physicist and a great individual. Even after he graduated, Raj has been in regular contact whenever I needed a discussion with him. Wakun Lam is an outstanding programmer and theorist who helped me a lot in simulation and data analysis. Siamak Dadras is a very conscientious and hard working person and helped me a lot in maintaining the lab running normally. Finally I would like to thank Jerry Clark and Amruthaa Sundararaj who joined the lab much later.

I would like to thank our best stuff members in physics department office at OSU. Susan, Tamera, Alisha and Charles are extremely helpful and friendly. I would also like to thank Melissa Edwards, the undergraduate lab coordinator, for her consideration of my schedules.

Finally, I want to extend my acknowledgment to all of my friends in Stillwater for their love and support.

Name: JIATING NI

Date of Degree: JULY, 2016

Title of Study: STATE DEPENDANCE OF QUANTUM RATCHETS

Major Field: PHYSICS

Abstract: This dissertation reports on the experimental investigation of quantum state evolution using the atomic-optical quantum delta kicked rotors (AOQDKR) with a Bose-Einstein condensate (BEC) of 87Rb atoms. To achieve the AOQDKR, a BEC was periodically exposed to short pulses of a horizontal optical standing wave which was formed from the interference of two off-resonant laser beams. In the first set of experiments, the fidelity (overlap) between the perturbed and unperturbed quantum states was studied. To study the fidelity of quantum state evolution, ε-classical maps with different kicking strength was given. It shows that as the kicking strength gets stronger, the area of the island is smaller while the chaotic region gets bigger. Experimentally a perturbation was introduced to the system by applying different kicking strength, the overlapping of the momentum distribution of these two sets of experiments decays with the perturbation. The effect of finite pulse length was also discussed: the fidelity decay rate is proportional to the pulse length. In the second set of experiments, the quantum ratchet with different initial states was studied. The theoretical analysis of the intrinsic mechanism of a quantum ratchet illuminates that peaks in the wave function of the initial state containing more than one plane waves arise at positions where the gradient of the standing wave happens to be the greatest. The more of the plane waves, the higher and narrower of the peaks. Experiments were carried out to observe an on-resonant atomic ratchet by exposing an initial atomic state which was a superposition of two or more momentum states to the AOQDKR. The dispersion of the momentum of ratchet current was measured as a function of kick number t. The strong ratchet current gives a small dispersion. It was verified that the ratchet current was stronger with an initial state containing more consecutive momentum states.

TABLE OF CONTENTS

Chapter Page

LIST OF FIGURES

Figure Page

CHAPTER I

INTRODUCTION

1.1 Bose-Einstein condensate

Bose-Einstein condensation (BEC) is one of the most special properties for bosonic atoms. At very low temperatures, a large fraction of these atoms can rapidly enter the very lowest motional energy state. Atoms in such state are undistinguishable from one another. Because they are similar to each other and cannot be distinguished, this state of matter is sometimes called a "super atom". Temperature is really describing the range of speeds of the bunch of atoms together. Since atoms in a BEC stay in the lowest energy level, the temperature of BEC is the one closest to "absolute zero", which is about 10^{-9}K for Alkali atoms in a typical optical trap. In 2001 Eric Cornel and Carl Wieman from JILA, University of Colorado (Anderson *et al.*, 1995) and Wolfgang Ketterle from MIT (Davis *et al.*, 1995a) won the Nobel Prize for realizing a BEC in a dilute gas.

The history of BEC begins with Satyendra Nath Bose in the early 1920s. Bose assumed certain rules for deciding when two photons should be counted up as either identical or different. We now call these rules "Bose statistics" (Bose, 1924). This concept attracted Einstein's attention and later was applied on the case of noninteracting atoms by Einstein which is now known as "Bose-Einstein Statistics" (Einstein, 1924, 1925).

It is difficult to realize BEC: on the one hand we want atoms to have a very low temperature, while on the other hand we need atoms to stay in a gaseous state. Perhaps the first step

along the road to achieving BEC was the creation of the magnetio-optical trap (MOT). Migdall, *et al.* first suggested the idea of the (MOT) in 1985 (Migdall *et al.*, 1985). Chu, *et al.* observed optically trapped atoms by applying six laser beams from six directions in 1986 (Chu *et al.*, 1986). Robb, *et al.* realized the first MOT in 1987 (Raab *et al.*, 1987). Davis, *et al.* and Petrich, *et al.* firstly demonstrated evaporative cooling in 1994 (Petrich *et al.*, 1994; Davis *et al.*, 1994).

In general, to make a BEC one should prepare a source of cold atoms, load the atoms into a magnetic or far-off-resonant optical trap (FORT) and evaporate the hot atoms or atoms with high energy to reduce the temperature to get BEC. For preparing a source of cold atoms, almost all of the research groups use a MOT. A MOT utilizes the combination of magnetic fields and laser light to trap and cool the atoms. However, the lowest temperature and highest phase space densities (a space in which all possible states of a system are represented) achievable with a MOT are not good enough to realize a BEC. That is the reason to use a FORT and evaporation. A FORT is used to increase the density of cold atoms and has the advantage that constituent light is too far from resonance to heat the atoms up by spontaneous emission.

1.2 Thesis organization

Two important aspects of the atom optics kicked rotor are investigated in this thesis: fidelity of quantum state and quantum ratchet. In order to provide a theoretical and experimental backdrop for these two studies, we start Chapter 2 with a review of the atom-optics quantum delta kicked rotor. In this Chapter we discuss the connections between the classical delta kicked rotor and quantum delta kicked rotor as well as the differences. Phenomena quantum resonance and quantum anti-resonance are also discussed. The nonlinearity of the system which is because of the interaction of the atoms is also discussed in this Chapter.

The quantum delta kicked rotor in experiments is sending a pulsed standing wave of light detuned from atomic resonance to a BEC. Thus an overview of the realization of BEC is

discussed in Chapter 3. The theoretical background including laser cooling, magneto-optical trapping, far-off-resonance trapping, and evaporative cooling is given in this Chapter.

A detailed description of the components used in the experiments and their purpose are given in Chapter 4, which is organized in a manner that gives a step by step by tour in the lab. The experimental set up includes rubidium dispenser, vacuum system, laser optical system, MOT beam alignment, polarization of the MOT beam, magnetic coil, CO_2 laser, imaging system, BEC procedure, and kicking system.

The evolution of quantum state under a small perturbation is the the subject of Chapter 5. In order to study how stable are the quantum states under the application of a small perturbation, experiments with and without the small perturbation are conducted. The overlap of perturbed and unperturbed quantum states which is known as fidelity is studied. The ϵ-classical maps with different kicking strength is also given in this Chapter.

In Chapter 6, the theoretical intrinsic mechanism of quantum ratchet is discussed. Different quantum ratchet with different initial states are given theoretically and experimentally. The sensitivity of the ratchet to the phase of the initial state is also investigated. Some other experiments with different time between pulses is performed too.

Finally, in Chapter 7 the summary of the thesis and the outlook for the future work are laid out.

CHAPTER II

THE ATOM-OPTICS QUANTUM DELTA KICKED ROTOR

One of the most important questions in physics that needs to be solved is to understanding the crossover between classical and quantum behavior. In a classical nonlinear system, the boundary between the two paradigms becomes clear. Classically, the nonlinear system exhibits chaos and it is impossible to predict its long term behavior. However, because of linearity of the Schrödingier equation, an equivalent quantum mechanical system is completely determined. The atom-optical delta kicked rotor is one tool to study this behavior and can be realized with a sample of ultra-cold atoms kicked by short pulses of an optical standing wave.

2.1 Classical δ-kicked rotor

The δ-kicked rotor is a quantum pendulum exposed to a potential which is on and off periodically in time (Haake; Stöckmann; Izrailev, 1990; Fishman, 1996). The model can be defined as a particle of mass M with linear momentum $\hat{p}$, constrained to move in circle of radius R, which is driven by a periodic constant force referred to as kicks. The model is sketched in Figure 2.1, together with the train of periodic δ-like kicks. The Hamiltonian of the kicked rotor is

$$H = \frac{J'^2}{2I} + V_0 \cos(\theta) \sum_q \delta(t - qT). \tag{2.1}$$

Here $J' = |\vec{R} \times \vec{p}|$ is the angular momentum and $I = MR^2$ is the moment of inertia, θ is the angular displacement, V_0 is the kick strength, t is the time and q is the number of the kicks which are switched on at time intervals of T. The Hamiltonian equations of motion can be written as

$$\frac{\partial H}{\partial \theta} = -\dot{J'} = V_0 \sin(\theta) \sum_q \delta(t - qT) \tag{2.2}$$

$$\frac{\partial H}{\partial J'} = \dot{\theta} = \frac{J'}{I}. \tag{2.3}$$

Integrating equation 2.2 and 2.3 over one period between $t = N$ and $t = N + 1$, one get

$$\theta_{q+1} - \theta_q = \frac{J'_{q+1} T}{I} \tag{2.4}$$

$$J'_{q+1} - J'_q = V_0 \sin \theta_q. \tag{2.5}$$

By applying the rescaled variables $J = \frac{J'T}{I}$ and $K = \frac{TV_0}{I}$, equation 2.4 and 2.5 can be written as

$$\theta_{q+1} = \theta_q + J_{q+1} \tag{2.6}$$

$$J_{q+1} = J_q + K \sin \theta_q. \tag{2.7}$$

This is known as the Chirikov-Taylor standard map where the dynamics are completely determined by the stochasticity parameter K (Gutzwiller, 1990; Chirikov, 1979). As shown in Figure 2.2, the phase space (θ, J) is dominated by stable closed curves for small values of K, while chaotic regions dominate the phase space for large values of K. The transition from stability to global chaos occurs at $K \approx 0.9716$ (Greene, 1979; MacKay, 1983).

2.2 Atom optics δ-kicked rotor

The quantum δ-kicked rotor is the quantum mechanical analogue of the classical δ-kicked rotor. It can be realized by exposing a sample of atoms to short periodic pulses of far-

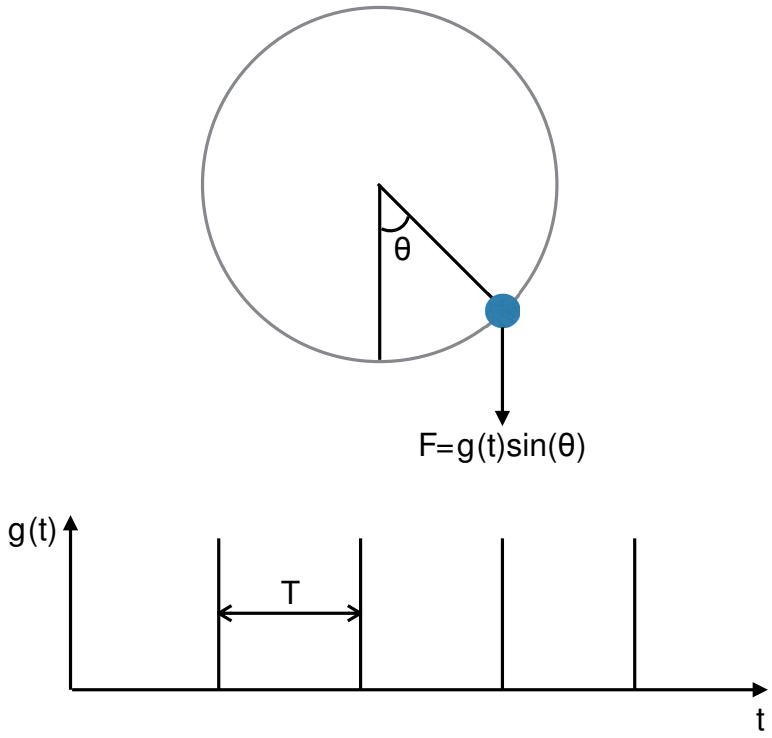

Figure 2.1: Periodically kicked quantum pendulum, where the kicking force $F(t)$ is periodic with time interval T and in the angle variable θ.

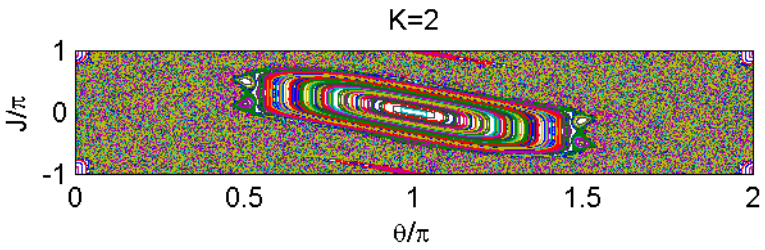

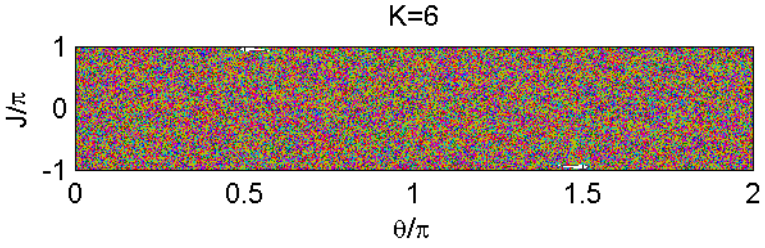

Figure 2.2: Classical δ-kicked rotor phase space for different kick strengths K. As K increases, the chaotic region gets bigger.

detuned light (Moore *et al.*, 1994). The Hamiltonian is

$$H = \frac{\hat{P}^2}{2M} + \hbar\phi_d \cos(G\hat{X}) \sum_{q=0}^{t} \delta(t - qT), \tag{2.8}$$

here $\hat{P}$ is the momentum, M is the mass of an atom, $G = \frac{4\pi}{\lambda} = \frac{2\pi}{\lambda_G}$ is the grating wave vector with λ_G the spatial period of the standing wave, $\hat{X}$ is the position, t is the continuous time variable, q is the number of kicks with time interval T, and $\phi_d = \frac{\Omega^2 \triangle t}{8\delta_L}$ is the strength of the kick, where Ω is the Rabi frequency between the ground and excited states, $\triangle t$ is the length of a pulse and δ_L is the detuning of the laser frequency from the atomic transition.

Writing the above Hamiltonian in dimensionless units is more convenient, which is

$$\mathcal{H} = \frac{\hat{p}^2}{2} + \phi_d \cos(\hat{x}) \sum_{q=1}^{t} \delta(t' - q\tau). \tag{2.9}$$

Here $\mathcal{H} = \frac{MH}{\hbar^2 G^2}$ and $t' = \frac{2\pi t}{T_{\frac{1}{2}}}$. $\hat{p} = \frac{\hat{P}}{\hbar G}$ is the scaled momentum in unit of two photon recoils. $\hat{x} = G\hat{X}$ is the scaled position in units of spatial period of the standing wave. $\tau = \frac{2\pi T}{T_{\frac{1}{2}}}$ is the scaled pulse period, where $T_{\frac{1}{2}} = \frac{2\pi M}{\hbar G^2}$ is the half Talbot time. When the pulse period is an integer multiple of the Talbot time ($T_T = \frac{4\pi M}{\hbar G^2}$), the free evolution of the wave between application of the kicking force can be neglected (Deng *et al.*, 1999; Lepers *et al.*, 2008). The periodic potential provides the connection between the particle propagating along it and the kicked rotor: the position of the particle can be folded into an angular coordinate $\theta = x \mod 2\pi$. From the quantum mechanical perspective the periodicity of the potential allows one to use Bloch's theorem on the atomic de-Broglie wave (Kittel and McEuen, 1976). The solutions are then invariant under translations by one period of the particle quasimomentum. If we write the momentum as $p = n + \beta$, where n is the integer part and β is the fractional part. β is also called the quasimomentum. In terms of photon exchange, each atom absorbs a photon from one of the standing wave beams followed by its subsequent stimulated emission into the other beam. The net result is that the atomic momentum can only change by two photon recoils ($\hbar G$) leaving the fractional part of its momentum (quasimomentum) unchanged.

2.3 Quantum resonance and anti-resonance

The Standard map can be quantized and the state evolution from one kick to immediately before the next kick is determined by the unitary Floquet operator

$$\begin{aligned} \hat{U} &= \hat{U}_{free}\hat{U}_{kick} \\ &= e^{-i\frac{\hat{p}^2}{2}\tau}e^{-i\phi_d\cos(\hat{x})}. \end{aligned} \tag{2.10}$$

$\hat{U}$ describes a free evolution given by $e^{-i\frac{\hat{p}^2}{2}\tau}$, followed by the kick operator $e^{-i\phi_d\cos(\hat{x})}$. The wave function after t kicks is given as

$$|\psi(t\tau)\rangle = \hat{U}^t|\psi(0)\rangle. \tag{2.11}$$

When the time period τ is an integer multiple of 4π, $\tau = 4\pi\ell$, the free evolution factor is unity. The system evolves freely over the kicking period with phases that are determined by the eigenenergies $\frac{n^2}{2}$. The free evolution is that $e^{-i\frac{n^2}{2}\tau} = 1$. So the application of t kicks with strength ϕ_d is equivalent to the application of one kick with strength $t\phi_d$. The operator for t kicks is

$$\hat{U}^t = e^{-it\phi_d\cos(\hat{x})}. \tag{2.12}$$

The probability for the atoms on initial momentum state $|0\rangle$ to be transferred to the state $|n\rangle$ by t kicks is

$$\begin{aligned} p_n &= |\langle n|\hat{U}^t|0\rangle|^2 \\ &= J_n^2(t\phi_d). \end{aligned} \tag{2.13}$$

Here the kick operator is expanded in the momentum basis by the Jacobi-Anger relation

$$e^{-it\phi_d\cos(\hat{x})} = \sum_{n=-\infty}^{\infty}(-i)^n J_n(t\phi_d)e^{in\hat{x}}, \tag{2.14}$$

where J_n is the Bessel function of first kind and order n. Then the mean energy at the end of t kicks is

$$\begin{aligned} \langle E \rangle &= \sum_{n=-\infty}^{\infty} n^2 p_n \\ &= \frac{1}{2} t^2 \phi_d^2. \end{aligned} \tag{2.15}$$

This is the very typical characteristic of a quantum rotor resonance: the mean energy grows quadratically in time, as shown in Figure 2.3.

Let's consider the situation that the time period τ is an odd integer multiple of 2π with zero initial momentum state. The wave function after one period evolution is

$$\begin{aligned} |\psi(T = T_{\frac{1}{2}})\rangle &= e^{-i\frac{\hat{p}^2}{2}\tau} e^{-i\phi_d \cos(\hat{x})} |\psi_0\rangle \\ &= \sum_{n=-\infty}^{\infty} (-i)^n J_n(\phi_d) e^{in\hat{x}} e^{-i\pi n^2} |\psi_0\rangle \\ &= \sum_{n=-\infty}^{\infty} (i)^n J_n(\phi_d) e^{in\hat{x}} |\psi_0\rangle \\ &= e^{i\phi_d \cos(\hat{x})} |\psi_0\rangle. \end{aligned} \tag{2.16}$$

The phase factor can be canceled by the next kick operator $\hat{U}_{kick}$ It shows that when the kicking period is an odd integer multiple of 2π, the phase evolution changes the sigh and can be canceled by the next kick with the same kicking period showed in Figure 2.3. This phenomenon is known as quantum anti-resonance.

2.4 Nonlinearity

In the study of atom-optics quantum delta kicked rotor, it is necessary to account for the interaction of the atoms. This is known as the nonlinearity and chaotic behavior can originate from these many-body dynamics. We use the time-dependent Gross-Pitaevskii equation to describe a BEC in a harmonic confinement with nonlinearity. This equation

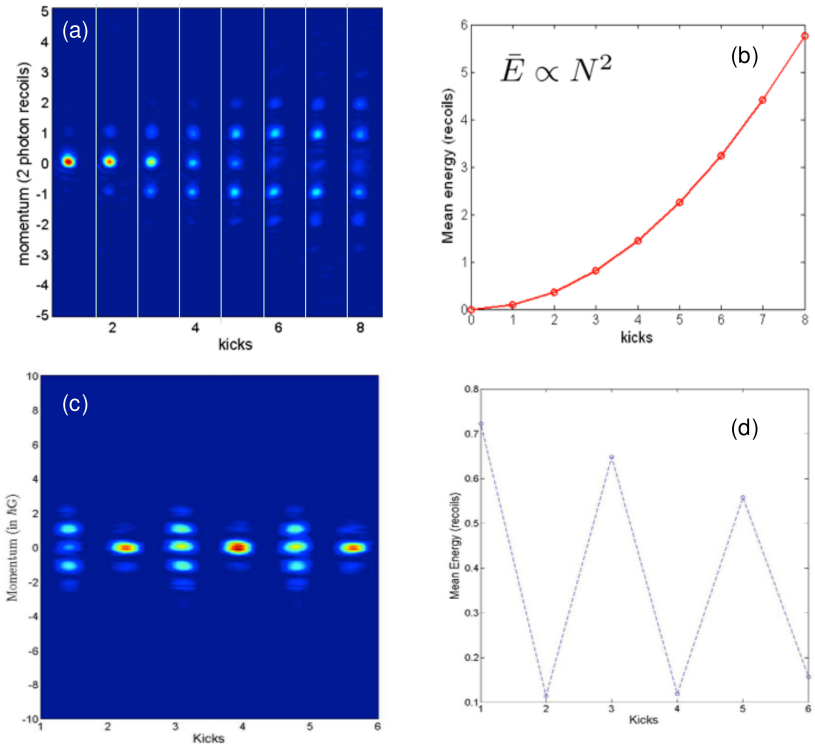

Figure 2.3: Momentum distribution according to number of kicks at quantum resonance (a) with a quadratic growth in mean energy (b) and anti-resonance (c) with an oscillation mean energy (d).

has the following form (Wimberger *et al.*, 2005):

$$i\hbar\frac{\partial\psi(\vec{r},t)}{\partial t}=\left[-\frac{\hbar^2\nabla^2}{2M}+\frac{M\omega_x^2x^2}{2}+\frac{M\omega_r^2\rho^2}{2}+V_0\cos(2k_Lx)\sum_{m=-\infty}^{+\infty}F(t-mT)+gN|\psi(\vec{r},t)|^2\right]\psi(\vec{r},t), \tag{2.17}$$

with $\rho^2=y^2+z^2$. $\psi(\vec{r},t)$ represents the condensate wave function, and M is atomic mass. The nonlinear coupling constant is given by $g=4\pi\hbar^2a/M$, N is the number of atoms in the condensate, a is the s-wave scattering length and k_L is the wave vector of the laser creating the optical potential. Assuming the laser is switched on at time instants separated by T, with maximum amplitude V_0 and periodic pulse shape function $F(t)$ of unit amplitude and duration $\delta T \ll T$. Here the fifth term is the nonlinear term. Therefore the mean field energy for a system is

$$E_{meanfield}=\frac{4\pi\hbar^2a}{M}n', \tag{2.18}$$

with n' represents the density of the atoms in a condensate.

It is not good to look at the nonlinearity isolated from the other energies in the system. We should compare the nonlinearity with other energy like the recoil energy of a laser pulse to determine if the nonlinear effect should be counted. The recoil energy of the laser pulse is

$$E_{recoil}=\frac{V_0\hbar}{\delta T}, \tag{2.19}$$

where δT is the pulse length. It is easy to get the ratio of the mean field energy to the recoil energy:

$$r=\frac{E_{meanfield}}{E_{recoil}}=\frac{4\pi\hbar a\delta Tn'}{MV_0}. \tag{2.20}$$

To determine the density of the atoms n' in a condensate, we need the number of the atoms in a condensate and the volume of the condensate. It is not hard to estimate the number of the atoms in a condensate by using matlab program. In our lab the average number of atoms in a BEC is about $70,000$. However we can't directly measure the volume of a BEC because BEC is generated at the center of a vacuum chamber. What we can do is estimate the diameter of the CO2 beam at the center of the vacuum chamber. The

estimated diameter of the CO2 beam is no less than $20\mu m$, thus the volume of a BEC is no less than $8 \times 10^{-15} m^3$. As a result, the estimated density of the atoms n' is about $10^{19} m^{-3}$. The s-wave scattering length a is $10^{-9} m^3$ for Rubidium atoms, the pulse length δT in our experiments is $0.56 \times 10^{-6} s$, the atomic mass M is $1.44 \times 10^{-25} kg$, and the amplitude of the pulse V_0 is no more 10. Therefore, the reasonable value of the ratio of the mean field energy to the recoil energy in our lab is about 10^{-5}, which means the nonlinearity is negligible and can be ignored.

CHAPTER III

LASER COOLING AND TRAPPING

3.1 Magneto-optical Trap

The technique of a magneto-optical trap uses laser cooling in conjunction with magnetic trapping to create samples of cold, neutral atoms at temperatures around 10^{-6}K. Atoms in MOT are slowed to speeds of 10 centimeters per second.

3.1.1 Laser cooling

The very basic idea of laser cooling is that by shining laser light on atoms, photons bounces off of atoms with more energy than when they hit the atoms which makes atoms slower, in other words colder. Steven Chu and his co-workers won the Nobel Prize in 1997 for experimentally realizing it (Chu *et al.*, 1986).

Photons have very little momentum. Compared to atoms, they are like ping-pong balls compared to a moving train. It is possible to change the speed and direction of a train by shooting enough ping-pong balls at it. Similarly, when an atom absorbs a photon, it is kicked in the direction of the photon before absorption. However, only the light with exactly the right frequency can do this (Allen and Eberly, 2012).

Then Doppler shift is applied to avoid hitting the slow atoms while hitting the fast atoms to slow them down. The Doppler shift says that when the observer is moving toward the source

of the wave, it sees the wave frequency shifted to a bluer color, and when it is going away from the source of the wave, it sees the wave frequency shifted to a redder color (Ballot, 1845). So with the laser light frequency detuned below the atomic resonant frequency, atoms traveling towards the laser source see the laser light shifted closer to resonant frequency. As a result, the atoms scatter more photons and decrease the velocity. If atoms travel away from the laser source, they see the laser light shifted further away from resonant frequency. In that case, the laser light just goes right by the atoms (Chu *et al.*, 1985).

With just one detuned laser beam it can only slow atoms down in one direction. But the atoms in the chamber are bouncing around in all directions. To slow all the atoms down one need to send three pairs of counter propagating laser beams in three orthogonal directions into the chamber. Note that this damping force is velocity-dependent and non-conservative. Then if all the laser beams are detuned below the atomic resonant frequency all the atoms will get cold. Physicists call this optical molasses.

To derive the damping force equation, we start from the quantum mechanical force operator,

$$\hat{F} = -\nabla \hat{H}, \tag{3.1}$$

whose expectation value is the average damping force. Here $\hat{H}(t) = \hat{H}_0 + \hat{H}'(t)$ is the total system Hamiltonian with $\hat{H}_0$, the field free time independent Hamiltonian and $\hat{H}'(t)$, the time dependent interaction Hamiltonian. The expectation value is given by

$$\langle \hat{F} \rangle = Tr(\hat{\rho}\hat{F}), \tag{3.2}$$

where $\hat{\rho}$ is the density matrix. Its time evolution is given by

$$\frac{d\hat{\rho}}{dt} = -\frac{i}{\hbar}[\hat{H}, \hat{\rho}], \tag{3.3}$$

here

$$[\hat{H}, \hat{\rho}] = \hat{H}\hat{\rho} - \hat{\rho}\hat{H}. \tag{3.4}$$

For $\hat{H}_0$, its eigenvalue is $E_n = \hbar\omega_n$ and the eigenfunctions are $\phi_n(\vec{r})$ which are linearly independent and form a complete set. To calculate the force on the atoms by the laser field, it is good to start with the solution of the time dependent Schrödinger equation

$$\hat{H}(t)\psi(\vec{r},t) = i\hbar\frac{\partial\psi(\vec{r},t)}{\partial t}. \tag{3.5}$$

Here the wave function $\psi(\vec{r},t)$ can be expanded in terms of $\phi_n(\vec{r})$, thus

$$\hat{H}(t)\psi(\vec{r},t) = [\hat{H}_0 + \hat{H}'(t)]\sum_k c_k(t)\phi_k(\vec{r}). \tag{3.6}$$

Applying Eq. (3.6) to Eq. (3.5), integrating over spatial coordinates $\vec{r}$ and multiplying by $\phi_j^*(\vec{r})$ one gets

$$i\hbar\frac{dc_j(t)}{dt} = c_j(t)E_j + \sum_k c_k(t)\hat{H}'_{jk}(t), \tag{3.7}$$

where $\hat{H}'_{jk}(t) = \langle\phi_j|\hat{H}'(t)|\phi_k\rangle$. When considering a simple two state atom the problem is known as the Rabi two-level problem and has two coupled differential equations (Allen and Eberly, 2012)

$$i\hbar\frac{dc_g(t)}{dt} = c_g(t)(E_g + \hat{H}'_{gg}) + c_e(t)\hat{H}'_{ge}(t), \tag{3.8}$$

and

$$i\hbar\frac{dc_e(t)}{dt} = c_e(t)(E_e + \hat{H}'_{ee}) + c_g(t)\hat{H}'_{eg}(t). \tag{3.9}$$

Where $\hat{H}'_{ge}(t) = \hat{H}'^{*}_{e.g.}(t)$. The subscripts e and g are excited and ground states respectively. The interaction term is given by $\hat{H}'_{eg}(t) = -\vec{\mu}\cdot\vec{E}(\vec{r},t)$ (Bernath, 2005). Here $\vec{E}(\vec{r},t)$ is the electric field and $\vec{\mu} = q\langle e|\vec{\epsilon}\cdot\vec{r}|g\rangle$ is the induced dipole moment with the light polarization unit vector $\vec{\epsilon}$. Due to the odd parity of $\hat{H}'$, only opposite parity atomic states can couple through the dipole interaction ($\hat{H}'_{ee}(t) = \hat{H}'_{gg}(t) = 0$) giving the final form of the Hamiltonian matrix as

$$\hat{H} = \begin{pmatrix} 0 & -\vec{\mu}\cdot\vec{E}^*(\vec{r},t) \\ -\vec{\mu}\cdot\vec{E}(\vec{r},t) & \hbar\omega_e \end{pmatrix}. \tag{3.10}$$

By applying Eq. (2.10) to Eq. (2.3), the time evolution of the density matrix is

$$\begin{pmatrix} \dot{\rho}_{gg} & \dot{\rho}^*_{eg} \\ \dot{\rho}_{eg} & \dot{\rho}_{ee} \end{pmatrix} = i \begin{pmatrix} \Omega^*(\vec{r},t)\rho_{eg} - \Omega(\vec{r},t)\rho^*_{eg} & \omega_e\rho^*_{eg} - \Omega^*(\vec{r},t)u \\ -\omega_e\rho_{eg} + \Omega(\vec{r},t)u & -\Omega^*(\vec{r},t)\rho_{eg} + \Omega(\vec{r},t)\rho^*_{eg} \end{pmatrix}, \tag{3.11}$$

where $\Omega(\vec{r},t) = \vec{\mu}\cdot\vec{E}(\vec{r},t)/\hbar$ is the Rubi frequency and $u = \rho_{gg} - \rho_{ee}$ is the population difference. For a closed two level system, the total population is conserved so $\rho_{ee} + \rho_{gg} = 1$ and $\rho_{eg} = \rho^*_{ge}$. Thus the optical Bloch equation can be written as (Metcalf and Van der Straten, 1999)

$$\frac{d\rho_{eg}(t)}{dt} = -\frac{\gamma}{2}\rho_{eg} - i\omega_e\rho_{eg} + i\Omega(\vec{r},t)u \tag{3.12}$$

and

$$\frac{du}{dt} = \gamma(1-u) + i\left[\Omega^*(\vec{r},t)\rho_{eg} - \Omega(\vec{r},t)\rho^*_{eg}\right]. \tag{3.13}$$

The spontaneous emission rate is $\gamma = \omega^3_\ell\mu^2/3\pi\epsilon_0\hbar c^3$, where ω_ℓ is the laser frequency. The first term in the equations represent the effect of spontaneous emission in the evolution of the density matrix. By rewriting $\rho_{eg} = \sigma_{eg}e^{-i\omega_\ell t}$ and $\vec{E}(\vec{r},t) = \vec{E}(\vec{r})\cos(\omega_\ell t)$ Eq. (3.12) and Eq. (3.13) reduce to

$$\frac{d\sigma_{eg}}{dt} = -\left(\frac{\gamma}{2} - i\delta\right)\sigma_{eg} + \frac{iu\Omega(\vec{r})}{2} \tag{3.14}$$

and

$$\frac{du}{dt} = \gamma(1-u) + i\left[\Omega^*(\vec{r})\sigma_{eg} - \Omega(\vec{r})\sigma^*_{eg}\right]. \tag{3.15}$$

We ignore the the terms with high frequencies $2\omega_\ell$ because they average to zero. $\delta = \omega_\ell - \omega_e$ is the laser frequency detuning from the atomic transition. The steady solutions of Eq. (3.14) and Eq. (3.15) are

$$\sigma_{eg} = \frac{2\Omega\left(-\delta + i\frac{\gamma}{2}\right)}{\gamma^2\left[1 + \left(\frac{2\delta}{\gamma}\right)^2 + \frac{2\Omega^2}{\gamma^2}\right]} \tag{3.16}$$

and

$$u = \frac{1 + \left(\frac{2\delta}{\gamma}\right)^2}{\left[1 + \left(\frac{2\delta}{\gamma}\right)^2 + \frac{4\Omega^2}{\gamma^2}\right]}. \tag{3.17}$$

For the case where electric field is produced by a traveling wave propagating in z-direction, $E(z) = E_0 \cos(kz - \omega_\ell t)$. By applying Eq. (3.10) in Eq. (3.1), the force operator can be written as

$$\hat{F} = \begin{pmatrix} 0 & \mu\frac{\partial E^*(z)}{\partial z} \\ \mu\frac{\partial E(z)}{\partial z} & 0 \end{pmatrix}. \tag{3.18}$$

Thus Eq. (3.2) can be written as

$$\langle \hat{F} \rangle = Tr(\hat{\rho}\hat{F}) = \mu\frac{\partial E}{\partial z}\sigma^*_{eg}e^{i\omega_\ell t} + \mu\frac{\partial E^*}{\partial z}\sigma_{eg}e^{i\omega_\ell t}. \tag{3.19}$$

Substituting Eq. (3.16) in Eq. (3.19), the force on a stationary atom is

$$F = \frac{\hbar k\gamma s}{2\left[1 + \left(\frac{2\delta}{\gamma}\right)^2 + s\right]}, \tag{3.20}$$

where $s = 2\Omega^2/\gamma^2$ is the saturation parameter.

For the case of an atom moving with velocity v, because of Doppler shift it will see the laser frequency detuned by $\delta \pm kv$. The plus (minus) sign refers to an atom moving in the opposite (same) direction to the laser beam. Thus the force on a moving atom is

$$F = \pm\frac{\hbar k\gamma s}{2\left[1 + \left(\frac{2(\delta \mp kv)}{\gamma}\right)^2 + s\right]}, \tag{3.21}$$

where the plus (minus) refers to the force applied on an atom moving along (opposite) the direction of light field. Considering the case of an atom experiencing two counter propagating beams in z-direction, the total force on the atom will be

$$F = \frac{\hbar k\gamma s}{2\left[1 + \left(\frac{2(\delta - kv)}{\gamma}\right)^2 + s\right]} - \frac{\hbar k\gamma s}{2\left[1 + \left(\frac{2(\delta + kv)}{\gamma}\right)^2 + s\right]}. \tag{3.22}$$

Assuming Doppler shift is smaller than δ, the damping force is a velocity dependent force $F = -\beta v$, where β, the damping coefficient, can be written as

$$\beta = \frac{8\hbar k^2 s\delta}{\gamma\left[1 + \frac{4}{\gamma^2}(\delta - kv) + s\right]\left[1 + \frac{4}{\gamma^2}(\delta + kv) + s\right]}. \tag{3.23}$$

This equation can be understood as with laser frequency detuned below zero i.e., $\delta < 0$, atoms traveling towards the laser source see the laser light shifted closer to resonant frequency while atoms traveling away from the laser source see the laser light shifted further away from resonant frequency (Shrestha, 2013).

With this damping force one may think of slowing atoms down to velocity zero and obtaining temperature zero. This is impossible, because of the recoil effect of a single photon. This is the ultimate limit of temperature for atoms to be cooled using laser beams. The random nature of the photon scattering process causes a diffusion of atoms in momentum space and atoms are heated. When the laser cooling rate is equal to the recoil heating rate, the temperature is the lowest one for optical molasses. This is called Doppler temperature T_D and is given by

$$T_D = \frac{\hbar\gamma}{2k_B}, \tag{3.24}$$

where k_B is the Boltzmann constant and γ is the nature line width. For rubidium 87 the Doppler temperature is 146 μK.

It was surprising that in early experiments a temperature was found which was much lower than the Doppler temperature (Lett *et al.*, 1988). This sub-Doppler temperature can be explained by the theory of multilevel structure of the atomic states and the optical pumping among these sublevels (Phillips, 1998; Gould *et al.*, 1987). Ultimately however, the lowest temperature achievable by laser cooling will be determined by the energy of a single photon. This is known as the recoil temperature and is given by

$$T_r = \frac{\hbar^2\gamma^2}{mk_B}, \tag{3.25}$$

which is 360 nK for rubidium 87.

3.1.2 Magneto-optical Trap

Magneto-optical trapping (MOT) is the most popular approach for setting up an apparatus for trapping neutral atoms. The very basic idea for a MOT is that an appropriate inhomogeneous magnetic field and arrangement of near-resonant laser beams leads to a trapping force. For simplicity, consider atomic transitions where $J_g = 0$ and $J_e = 1$. To further simplify the model let us assume that the atomic motion is only in the z-direction. Atoms are subjected to a linearly inhomogeneous magnetic field $B(z) = B_0 z$, which splits the excited state into its three Zeeman components $M_e = -1, 0$, and $+1$ shown in Figure 3.4. Adding two counter-propagating laser beams of opposite circular polarization, each detuned below the zero field atomic resonance completes the requirements for making the MOT. For $B > 0$, because of the Zeeman shift, the excited state $M_e = +1$ is shifted up while the excited state $M_e = -1$ is shifted down. At position Z', the magnetic field tunes the $\Delta M = -1$ transition closer to resonance (or closer to laser frequency) and the $\Delta M = +1$ transition further away from resonance. The polarization of the laser beam incident from right is chosen to be σ^- and correspondingly for the one incident from left the polarization is σ^+. Thus more photons are scattered form the σ^- beam than the σ^+ beam. As a result, the atoms are driven towards the center of the trap where the magnetic field is zero. On the other side of the center of the trap, for $B < 0$ the shift of the $M_e = \pm 1$ states are reversed, and more photons are scattered from σ^+ beam. So the atoms sitting at the left side are driven towards the center of the trap as well. In the optical molasses, the damping force due to the Doppler shift slows down the atoms and the magnetic field facilitates pushing atom to the center of the trap. A 3D extension of a MOT scheme can be implemented by using three pairs of counter-propagating laser beams in three orthogonal directions.

3.2 Evaporative cooling

In the early days of laser cooling, there was a great hope that atoms could be cooled without any limitations. However people later realize that it is impossible because of the recoil

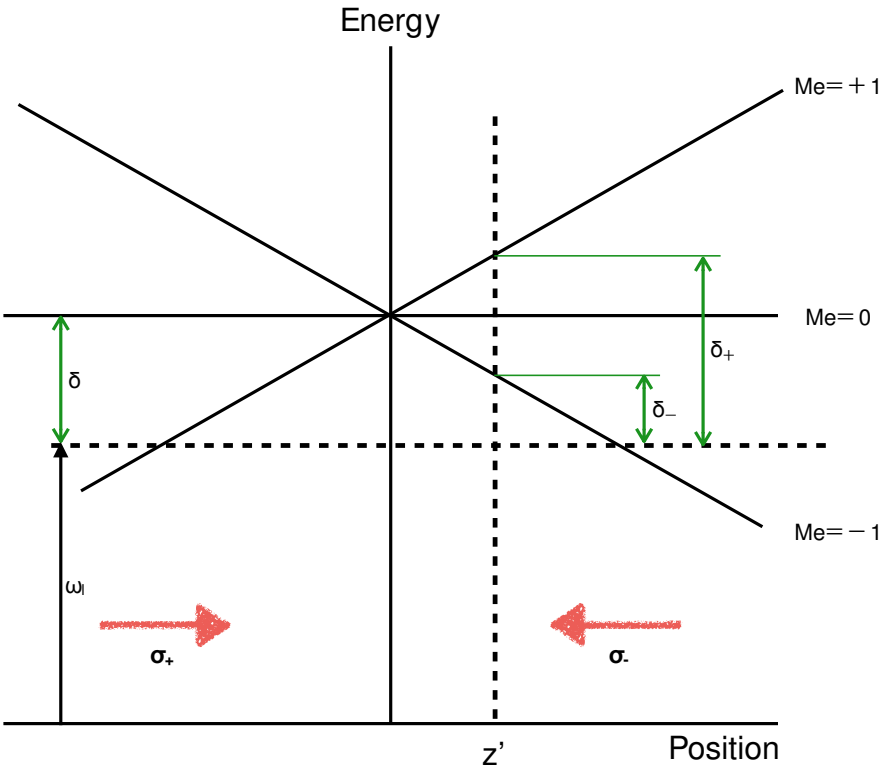

Figure 3.1: ω_ℓ is the laser frequency. For atoms at position Z' the transition $\Delta M = -1$ is closer than $\Delta M = +1$. More photons are scattered form the σ^- beam than the σ^+ beam.

heating which is already discussed in the previous section. Thus the maximum achievable phase space density, $\rho = n\lambda_{dB}^3$, with laser cooling is about 10^{-5} to 10^{-4} (i.e. obtaining μK temperatures), and the density of the atomic gas increases. But as the density increases, the collision rate between atoms with one in the excited state increases as well. Since the energy is inelastic, the energy exchange induces heating effect on the atoms. As a result, near resonance light should be avoided in order to obtain BEC. So laser cooling alone is not enough for BEC. One way to increase phase space density is to use evaporative cooling (Hess, 1985, 1986; Hess *et al.*, 1987). This idea was firstly proposed by Harald Hess for atomic Hydrogen. His idea was based on the preferential removal of atoms with energy higher than the average from a trap, followed by rethermalization of the remaining atoms by elastic collisions. Since both the temperature and volume decrease, the phase space density can increase. In 1994 the technique was extended to alkali atoms by combining evaporative cooling with laser cooling (Anderson *et al.*, 1995).

3.2.1 Far-off-resonance trap

Evaporative cooling of atomic gases requires an environment for the atoms which insulate them from the "hot world". Therefore, a wall-free confinement of the atomic cloud would be ideal. Because of the recoil limit, none of the elements of the MOT can be used. As a result, there are mainly two methods used to provide this kind of confinement: magnetic fields or far-off-resonant optical fields.

A far-off-resonant trap (FORT) is based on the fact that an off-resonant laser creates a potential which is attractive or repulsive depending on whether it is red or blue detuned from an atomic transitions. The trap depth depends approximately on the laser intensity I divided by the detuning δ_ℓ ($U \approx \frac{\hbar I}{4\delta_\ell}$), while the spontaneous scattering rate depends on intensity divided by the square of the detuning ($\gamma \approx \frac{\Gamma I}{4\delta_\ell^2}$, where Γ is the spontaneous-emission rate of the atom) (Miller *et al.*, 1993). Therefore the advantage of a large detuning is that one can reduce the rate of scatter while keeping the same potential well depth.

3.2.2 Evaporative cooling

There are different models for the evaporative cooling process (Doyle *et al.*, 1991; Davis *et al.*, 1995b; Wu and Foot, 1996). We will review a simple but instructive model which is given by Davis *et al.* (Davis *et al.*, 1995b). Evaporative cooling is the same physics that cools a cup of hot coffee. In the coffee, the most energetic water molecules escape from the cup and come off as steam. When they do this, they take away more than their share of heat, and the atoms left behind in the cup are colder because on average they have lost energy. To make BEC, the most energetic atoms are allowed to escape from the FORT. In Davis's model, the trap depth is lowered in one single step to a finite value $\eta k_B T$. The effect of removal of high energy atoms on the thermodynamical quantities is calculated. The remaining fraction of atoms is $\nu = \frac{N'}{N}$. The decrease in temperature which is due to the release of the hot atoms is defined as

$$\gamma = \frac{\log(T'/T)}{\log \nu}. \tag{3.26}$$

Here the primed quantities refer to values after the evaporative cooling process. In a d-dimensional potential, $U(r) \propto r^{\frac{d}{\xi}}$ and the volume $V \propto T^{\xi}$ (Bagnato *et al.*, 1987) where ξ describes the type of the potential. Thus the scaling of the important thermodynamic quantities are $N' = N\nu$, $T' = T\nu^{\gamma}$, and $V' = V\nu^{\gamma\xi}$. The phase space density $\rho = n\lambda_{dB}^3$ scales as $\rho' = \rho\nu^{1-\gamma(\xi+\frac{3}{2})}$. Here the value of ξ describes the type of the potential. For a linear potential like a spherical quadrupole trap $\xi = 3$, while for a harmonic potential as in an optical trap $\xi = \frac{3}{2}$. One can track the evolution of the thermodynamical quantities with the lowering of the trap depth if ξ, $\nu(\eta)$ and $\gamma(\eta)$ are given. The density of states for atoms in a trapping potential $U(x, y, z)$ is

$$D(E) = \frac{2\pi(2M)^{\frac{3}{2}}}{\hbar^3} \int_V \sqrt{E - U(x, y, z)} d^3r. \tag{3.27}$$

After the trap depth has been decreased to $\eta k_B T$, the fraction of atoms remaining in the trap is

$$\nu(\eta) = \frac{1}{N} \int_0^{\eta k_B T} D(E) e^{-\frac{E-\mu}{k_B T}} dE, \tag{3.28}$$

where μ is the chemical potential of the gas. The occupation number is given by the Maxwell-Boltzmann distribution $e^{-\frac{E-\mu}{k_B T}}$ since the effects of quantum statistics can be neglected for a dilute gas. One can rewrite Eq. (3.24) as

$$\nu(\eta) = \int_0^{\eta} \Delta(\epsilon) e^{-\epsilon} d\epsilon \tag{3.29}$$

where $\epsilon = \frac{E}{k_B T}$ is the reduced energy and the reduced density of states is

$$\Delta(\epsilon) = \frac{\epsilon^{\frac{1}{2}+\xi}}{\Gamma(\frac{3}{2}) + \xi}. \tag{3.30}$$

After truncation, the total energy of the atoms is $\alpha(\eta) N k_B T$ where

$$\alpha(\eta) = \int_0^{\eta} \epsilon \Delta(\epsilon) e^{-\epsilon} d\epsilon. \tag{3.31}$$

Therefore the average total energy per atom in units of $k_B T$ is $\alpha(\eta)/\nu(\eta)$. For $\eta -> \infty$, the average total energy is $\alpha(\infty)/\nu(\infty) = (\frac{3}{2} + \xi)/1$. Thus the decrease in temperature is

$$\frac{T'}{T} = \frac{\alpha(\eta)/\nu(\eta)}{\alpha(\infty)/\nu(\infty)}. \tag{3.32}$$

Plugging Eq. (3.28) to Eq. (3.22), one get

$$\gamma(\eta) = \frac{\log\left[\frac{\alpha(\eta)}{\nu(\eta)\alpha(\infty)}\right]}{\log\left[\nu(\eta)\right]}. \tag{3.33}$$

For a specific type of potential one can determine the value of γ. For $\xi = \frac{3}{2}$,

$$\nu(\eta) = \frac{1}{\Gamma(3)} \int_0^{\eta} \epsilon^2 e^{-\epsilon} d\epsilon = 1 - \frac{2 + 2\eta + \eta^2}{2e^{\eta}}, \tag{3.34}$$

and

$$\alpha(\eta) = \frac{1}{\Gamma(3)} \int_0^\eta \epsilon^3 e^{-\epsilon} d\epsilon = 3 - \frac{6 + 6\eta + 3\eta^2 + \eta^3}{2e^\eta}, \tag{3.35}$$

where $\Gamma(n) = (n-1)!$ and $\int u(x)v(x)dx = u\int vdx - \int u' \int vdxdx$. Here it can be seen that for the same truncation, a higher phase space density is achieved with a larger ξ due to a faster shrinking of volume with decreasing temperature ($V \propto T^\xi$) (Talukdar, 2010).

CHAPTER IV

EXPERIMENTAL APPARATUS

A detailed description of the components used in the experiments and their purpose are given in this chapter. It will be organized in a manner that gives a step by step tour in the lab. We choose rubidium 87 as the atom and place them in a chamber which is kept in an ultra-high vacuum by the vacuum system. All the light with the right frequencies is prepared on one optical table, and is then sent to the other table on which the vacuum chamber is placed. The laser beams are sent into the chamber from six directions. With the help of a magnetic field, which is generated by strong currents in a pair of coils, atoms can be trapped when a MOT is formed. Then a CO_2 laser beam is sent right through the cloud of atoms to further cool them down. The BEC is invisible, so we need some imaging beam to make it visible. Thus imaging system is introduced.

4.1 Rubidium dispenser

We use a rubidium dispenser in our lab as the source of atoms. The reasons we use rubidium 87 are:

a) The excitation frequency from the ground state to the first state is in the near IR region, thus it is possible for one to generate the light with a cheap diode laser.

b) Because rubidium has high vapor pressure at room temperature, it is easy to generate enough atomic vapor with a small current.

c) The collision properties make it easy to lower the temperature of the atoms to an ultra cold temperature with evaporative cooling.

Rubidium dispensers are widely used in atomic research to make simple atom sources. In the dispensers, atoms are released from a metal surface as the temperature increases. We send current through the dispenser, and control the temperature by increasing or decreasing the current. Thus, finding the right current is important. With too low a current, the MOT will be too small to generate a BEC. With a too high a current, the possibility of collision between atoms will increase dramatically and the atom energy cannot be lowered further. Also too many background collision makes it hard to hold the atoms in the FORT for very long. Besides, high current will decrease the life expectancy of the dispenser as well. For a new rubidium dispenser, the current can be set at 2 A and be gradually increased to 4 A near the end of its life when the dispenser has been depleted of rubidium atoms. Usually, we choose the current in which the MOT loading time is about 20 seconds. Our rubidium dispenser is a commercial product from SAES Getters (RB/NF/4.8/17FT10+10). To start a new dispenser, it needs to be run at high current for several minutes to remove the oxide layer. During the initial bake out of the vacuum system, it is also necessary to run the dispenser at a high current for several minutes to remove the absorbed water and other impurities. We installed three rubidium dispensers in the vacuum chamber which can support experiments for several years.

4.2 Vacuum system

The vacuum system mainly consists of vacuum chamber and pump. A good vacuum chamber has to attain an ultra-high vacuum and have good optical access. The vacuum chamber is the heart of the BEC experiment and is where the atoms are trapped, BEC generated, and the experiment carried out. Our vacuum chamber consists of a six-way cross with an octagonal multiport chamber from MDC vacuum products attached to one of the flanges. These components are all stainless steel and are shown in Figure 4.1. There are four 2 inch diameter antireflection coated and quartz viewports for directing the MOT beams into

the chamber. There are four 1 inch diameter ZnSe viewports with low absorption at 10.6 μm which are used for directing the high power CO_2 laser beams into the chamber. One 5 inch diameter quartz viewport is attached to one side of the six way cross and another is attached to the large opening on the orthogonal chamber. Each viewport had a conflat flange sealing surface which enabled baking to 200^{o}C.

There is an outlet valve that can be connected to a turbo-molecular pump (model number 151 C) on one side of the six-way cross which is used during the initial pumping of the vacuum system. On another side of the six-way cross there is a two port generic Varian style 8liter/s ion pump powered by Terrenova 751 controller. Three SAES Getter rubidium dispenser sources are installed in the vacuum chamber and are connected to electric feedthrough terminals installed on one side of the six-way cross. The remaining side of the six way cross was sealed. It was very important to reduce stray magnetic fields in the region of the MOT. Thus the vacuum chamber was shielded from the ion pump's magnetic field using magnetic shield.

Prior to assembling the vacuum system, all parts were cleaned with methanol to remove any foreign material. To prevent contamination, gloves were worn to handle the clean components as well. Argon gas was pumped into the system, during the assembly of the viewports, to minimize the build up of normal atmospheric gas (especially water vapor) on the vacuum walls. A Leybold Trivac-b model D1.6B rotary vane roughing pump maintained proper inlet pressure for the turbo pump. This step only takes a few minutes. Then the Turbo-molecular pump is on and maintains a minimum pressure of 8×10^{-9} Torr with an inlet pressure of 10^{-3} Torr. The Varian 0351 vacuum gauge is installed to indicate pressures in the range of atmospheric down to 10^{-4} Torr. Leaks were checked by applying either helium gas or methanol. Its signal is a rapid rise in pressure on the vacuum gauge. While the roughing and turbo pumps were working the vacuum chamber was baked in a tent with insulating sides. The temperature was gradually increased in 20^{o}C increments to a maximum of 200^{o}C over two days. Then the vacuum chamber was left to bake for three days to ensure that most of the water and other impurities outgassed from the chamber's walls. While baking, the turbo-molecular pump was running to keep the pressure about

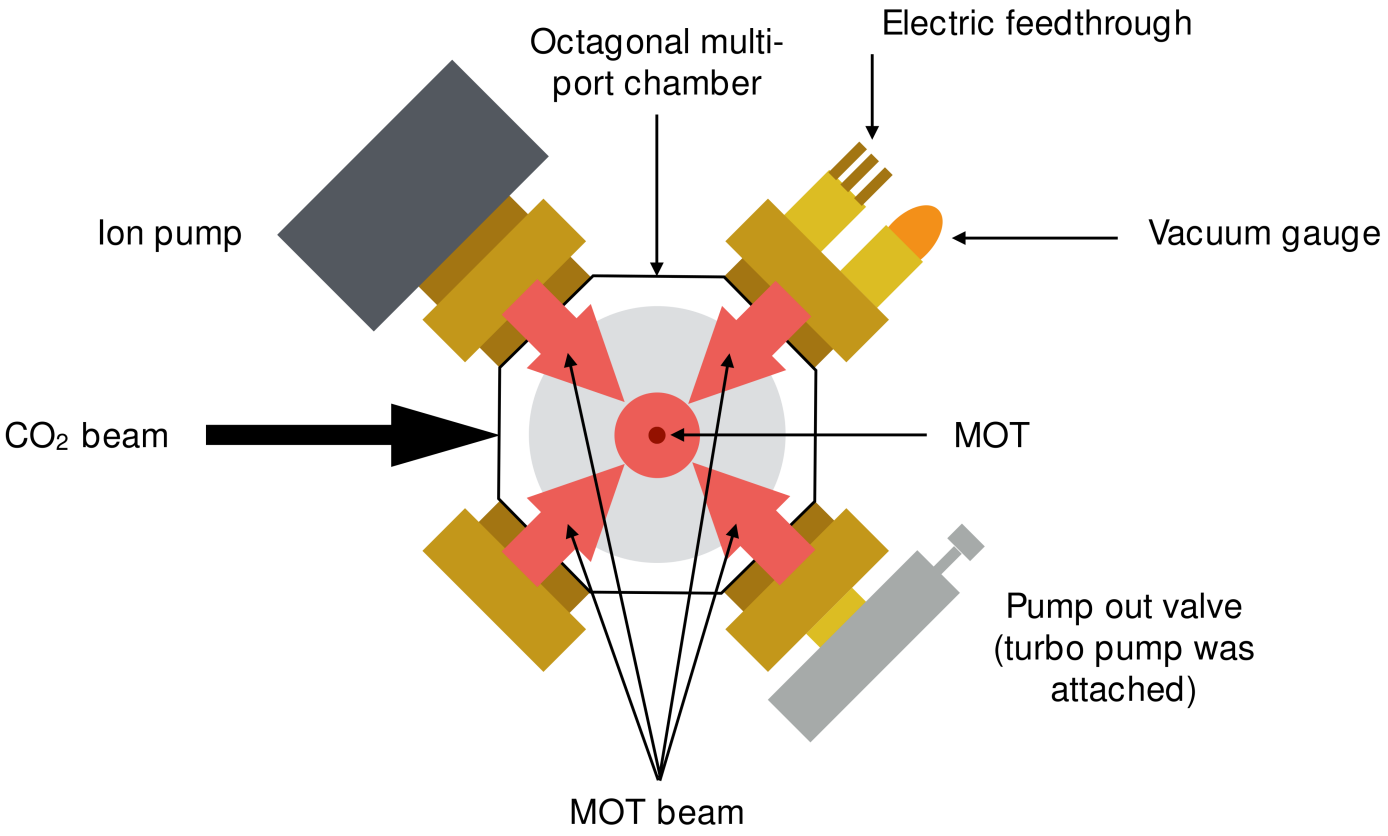

Figure 4.1: Schematic drawing of the vacuum system showing the six-way cross and an octagonal multi-port chamber.

10^{-8} Torr. The temperature was decreased gradually and the heaters were turned off. A Varian Valcon Plus 55 ion pump was used for further pumping the chamber. After a couple of weeks of operation, the vacuum reached the low 10^{-11} Torr.

4.3 Laser optical system

One of the most important parts in generating a BEC is a frequency stabilized laser system. Precise and rapid control of the laser frequencies and powers are required. All of the optics necessary to prepare the laser light to trap and cool the atoms were placed on a single optical table referred to here as the "laser table". There are two sets of lasers set up on this table: the mast laser (and associated injection locked slave lasers), and the repump laser. One grating stabilized DL 100 Toptica laser in a temperature controlled housing was used as the master laser, which was operated in cw mode and had an output power of about 20 mW. Its frequency was locked to a frequency near the transition between the $5^2S_{1/2}$ $F = 2$ ground state and the cross over line between the $5^2P_{3/2}$ $F' = 2$ and $F' = 3$ excited states as shown in Figure 4.2. Because the output power was not sufficient to produce a MOT, three other home built diode lasers were used as slave lasers. The slave lasers were Sharp Microelectronics 784 nm wavelength diode lasers with a 100 mW maximum output power. These slave lasers were powered by Thorlab LDC500 current controllers and the temperature was maintained with a thermoelectric cooler driven by the Thorlab TEC2000 Thermoelectric Temperature Driver. Following the injection locking techniques, the modes of the slave lasers were identical to the mode of the master laser. Another grating stabilized DL 100 Toptica laser in a temperature controlled housing was used as the repump laser. Its frequency was locked to a frequency near the transition between $5^2S_{1/2}$ $F = 1$ ground state and $5^2P_{3/2}$ $F = 2$ excited state. Laser beams from the slave lasers and repump laser were transferred to the BEC vacuum chamber table by optical fibers.

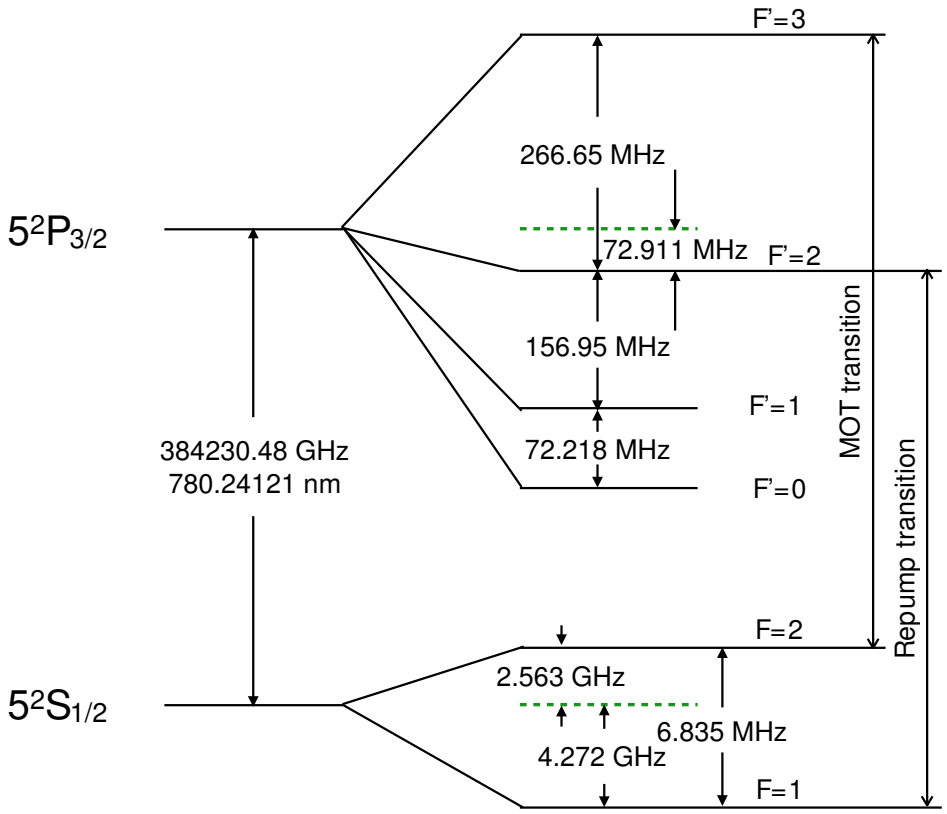

Figure 4.2: Hyperfine splitting of rubidium 87 D2 line (Ye *et al.*, 1996; Bize *et al.*, 1999). The transitions for the MOT light was on resonant between $F = 2$ and $F' = 3$; the transition for repump was on resonant between $F = 1$ and $F' = 2$.

4.3.1 Optical setup

Figure 4.3 shows the optical setup for the lasers and the optical components. The shape of the collimated laser beam out of the master laser head was elliptical initially. The laser beam profile was changed into a circular shape by passing through a pair of anamorphic prisms. A half-wave plane was placed right after the anamorphic prisms and rotated the beam polarization. There was a polarizing beam splitter cube (PBSC) placed after the half wave plane with its rotation axis at 45^o to the vertical. The half wave plane rotated the beam polarization so that all the light went through the PBSC. After the PBSC there was a Faraday rotator (isolator) which rotated the beam polarization from 45^o clockwise to horizontally polarized. Any reflected beam with horizontal polarization, passing from the reverse direction through the Faraday rotator, had its polarization rotated in the other direction and was eliminated by the PBSC in front of laser; while the injected beam with a vertical polarization was not blocked by the PBSC and was sent into the laser head. About 7 mW of light from the master laser was sent into main slave laser for injection locking. To monitor if the laser frequency was correct or not, small amount of light was sent through a rubidium vapor cell and into a Thorlab PDA 400 photodiode to see if there was an absorption dip on the oscilloscope. All the rest of the lasers were setup with similar procedures.

4.3.2 Saturated absorption spectroscopy

In order to lock the lasers, a saturated absorption spectroscopy signal for the master laser and repump lasers was needed for input to the laser circuity. Since the hyperfine structure of the saturated absorption spectroscopy covers a frequency range smaller than the Doppler broadened spectrum, one more laser beam was needed to distinguish the fine spectral lines. The technique of saturated absorption spectroscopy involved splitting the light exiting the laser into a low power “probe” beam and high power “saturating” beam. The low power was below the saturation intensity while the high power was above the saturation intensity. The two beams were approximately counter propagating through a vapor cell. The probe beam

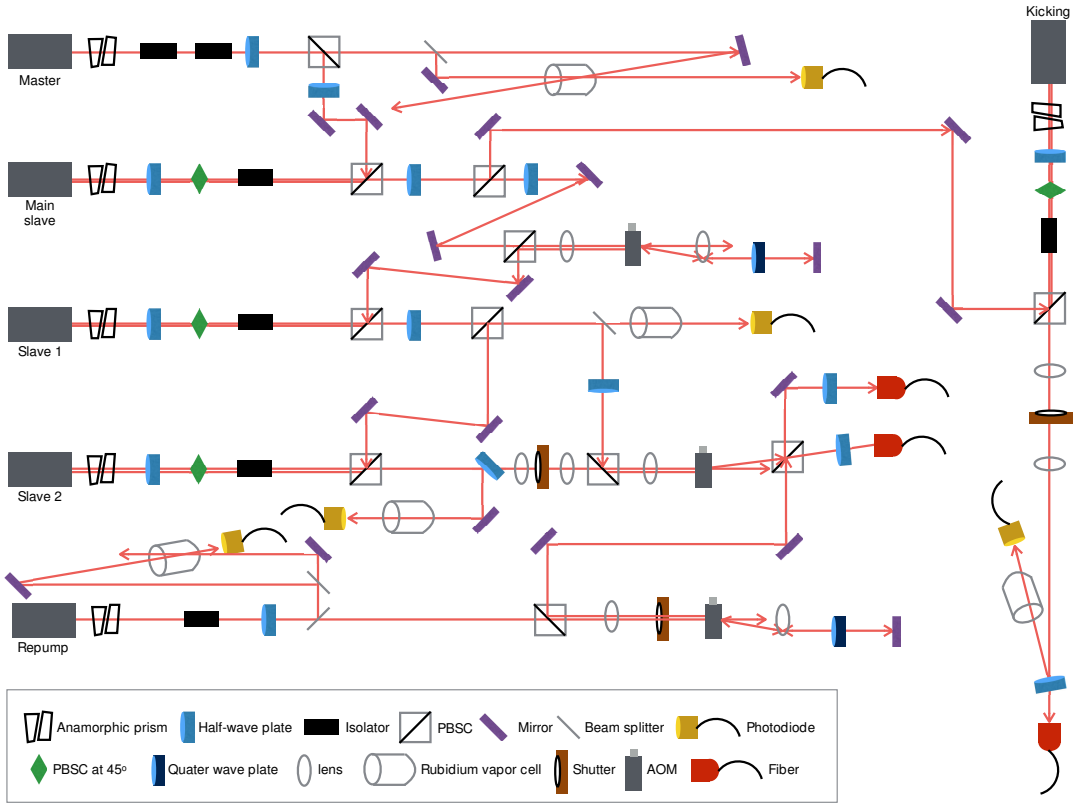

Figure 4.3: Optical setup for laser table shows various optical components and lasers used to prepare the MOT.

was sent into a photodiode which was placed right after the cell as shown in Figure 4.3. The hyperfine structure of rubidium 87 determined by saturation absorption spectroscopy is given in Figure 4.4, where the peak (a) is for the MOT transition and the peak (b) is for the repump transition.

To form a MOT, the lasers needed to be locked near to a spectral line. The laser beam was diffracted from a grating and the first order diffraction was sent back into the diode as optical feedback (Maki *et al.*, 1993). The zeroth order exited the cavity housing and was available for the experiment. Initial adjustment of the laser required the first order diffraction to be aligned back into the diode. We firstly lowered the current using the SC100 current control to about 41 mA to find the first order beam. Secondly by adjusting the horizontal and vertical micrometer screws on the grating mount we aligned the first order diffraction back into the laser. Once they were aligned with each other, the beam should flash, corresponding to a reduction in the laser threshold current. After that, the current can be lowered down to 40 mA. Finally, we turned the laser current back to the normal number (for the master laser it was 87 mA, for the repump laser it was 85 mA), and fine tuned the horizontal micrometer screw to get the mode. Because of the changing of the temperature and humidity, occasionally the laser mode was not good enough to lock the frequency, and we had to fine tune the horizontal screw to get the mode back. A piezo actuator was attached to the grating mount and provided fine tuning of the wavelength through the SC100 scan control in the supply rack.

4.3.3 Acousto-optical modulator

During the experimental process the laser beam frequency was switched through different values. Therefore, having precise control of the laser frequency and intensity was critical for our experiments. The frequencies were:

1. Light with detuning -17 MHz from the $5^2S_{1/2}\ F = 2 \rightarrow 5^2P_{3/2}\ F' = 3$ transition to make the MOT.

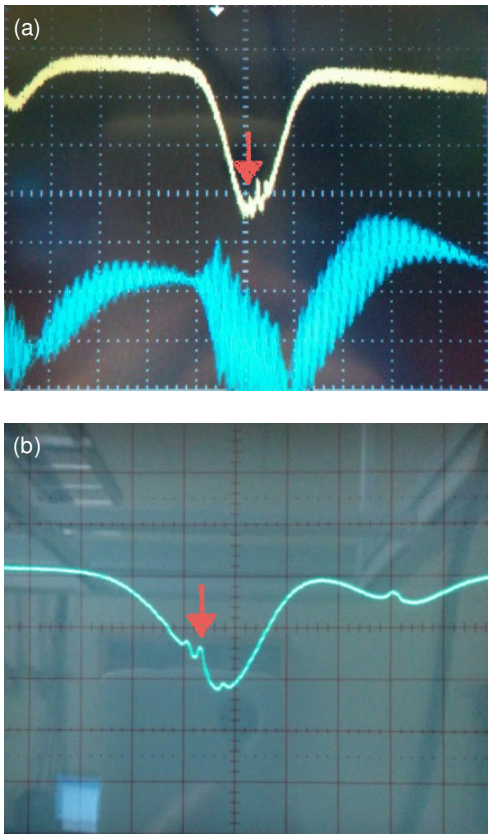

Figure 4.4: (a) The saturated absorption line for the repump beam, where the peak marked by an arrow is the frequency of the transition $5^2S_{1/2}$ $F = 1 \rightarrow 5^2P_{3/2}$ $F' = 2$; (b) The saturated absorption line for the MOT light, where the peak marked by an arrow is the frequency of the transition $5^2S_{1/2}$ $F = 2 \rightarrow$ the cross line between $5^2P_{3/2}$ $F' = 2$ and $F' = 3$.

2. Light with detuning -78 MHz from the $5^2S_{1/2}\ F = 2 \rightarrow 5^2P_{3/2}\ F' = 3$ transition for optical molasses cooling and loading atoms into the optical trap.

3. Light with 0 detuning (on resonance) from the $5^2S_{1/2}\ F = 2 \rightarrow 5^2P_{3/2}\ F' = 3$ transition for imaging.

4. Light for from $5^2S_{1/2}\ F = 1 \rightarrow 5^2P_{3/2}\ F' = 2$ transition for the repump laser.

An cousto-optical Modulator (AOM) was used to switch these frequencies because of its accuracy and fast switching time. To meet the requirements of the first three detunings, we used an ISOMET 1205 C-2 AOM called the "master AOM" which was placed behind the main slave laser. To avoid the deflection of the beam, the AOM was set in a double pass configuration as shown in Figure 4.3. After double passing the AOM, the main slave laser beam was injected into the slave 1 laser head with a frequency $f = f_0 + 2f_{AOM}$. Here f_0 was the master laser frequency and the first order on each pass through the AOM was selected. The light beams from the slave 1 and slave 2 lasers were sent through another ISOMET 1205 C-1 AOM together, which gave frequency -80 MHz by selecting the negative first order. Thus the final detuning from resonance achieved by the light before entering the fiber was given as

$$\delta = -133.3MHz + 2f_{AOM} - 80MHz. \tag{4.1}$$

As a result, for a MOT detuning of -17MHz the master AOM should be driven at frequency 98.15 MHz; for the cooling detuning of -78 MHz, the master AOM should be driven at frequency 67.65 MHz; for the imaging detuning of 0, the master AOM should be driven at frequency 106.65 MHz. It is worth noting that the beam size through the AOM had a significant impact on the switching time. Therefore, all of the AOMs were placed at the focus of an approximately one-to-one telescope.

4.3.4 Repump laser

It was possible that part of the atoms in the $5^2P_{3/2}\ F' = 3$ excited state decayed to the $5^2S_{1/2}\ F = 1$ ground state through spontaneous emission. Such a process eliminated the

atoms from interacting with the trapping beams and destroyed the MOT quickly. To prevent this situation, a repump laser was used. One grating stabilized DL 100 Toptica laser in a temperature controlled housing was used as the repump laser, which was operated in cw mode. Its frequency was locked to the cross over line between the $5^2S_{1/2}$ $F = 1$ ground state and $5^2P_{3/2}$ $F' = 1$ to $5^2P_{3/2}$ $F' = 2$ excited state. This enable the atoms to be exited from the $5^2S_{1/2}$ $F = 1$ ground state to the $5^2P_{3/2}$ $F' = 2$ excited state and then eventually decay back to the $5^2S_{1/2}$ $F = 2$ ground state. Atoms in this state can interact with the main MOT light again. The whole process is like a closed cycle.

The optical alignment of the repump laser was similar to the master laser and is shown in Figure 4.3. The laser was double passed through an ISOMET 1205 C-2 AOM which was driven by an ISOMET301B voltage tunable RF driver. The first order beam after the AOM (about 2.5 mW) was selected to be sent into the fiber which transferred the repump beam to the BEC table together with the MOT beam. After obtaining a MOT, during the process of loading the atoms into the optical dipole trap, the repump beam power was decreased to optimize the loading. We controlled the repump power by changing the RF power in the AOM via a voltage controlled attenuator.

4.4 MOT beam alignment

Laser beams from the laser table were sent to the BEC table through fibers. The laser beams out of the fibers were used as the MOT beams and the imaging beam. The optical setup on the BEC table is shown in Figure 4.5. The beam out of fiber 1, containing the slave beam and repump beam, was split by a PBSC into two beams, one was for MOT beam 1, while the other one was for MOT beam 2. The beam out of fiber 2, containing the slave beam only, was split by a partial reflector into two parts; the main part was for the MOT beam, while the other component was for the imaging system. Using the combination of two lenses, the MOT beams were expanded to about one inch diameter. Furthermore, the MOT beams were separately sent through quarter wave plates to make the light circularly polarized. All of the three MOT beams were sent into the vacuum chamber orthogonally,

and were retro-reflected by mirrors. These six beams were aligned to intersect at the center of the chamber, with the MOT appearing near the intersection of the beams. It is shown in Figure 4.1.

To separately control the laser beams on and off at different times, fast mechanical shutters (UNIBLITZ LS2T2) were used. These shutters were controlled by drivers which were connected to the digital voltage signals of PCI 6713 card on the computer.

4.5 Polarization of the MOT beams

After the alignment of the MOT beams, the next step was to set their polarizations. The sense of the current and orientation of coils which produced the magnetic field gradient determined the orientation of the respective circular polarizations. The four beams propagating in the direction perpendicular to the MOT coil axis should have the same circular polarization. Here the circular polarization was taken relative to the beam direction, and not an external quantization axis. The remaining two beams, propagating along the direction of the MOT coil axis, need to have opposite circular polarization to the first four beams (again relative to the direction of propagation). In principle the beam polarization and the MOT coil current should be determined initially. It is easier in practice to set the polarizations relative to each other first and then try both directions of the MOT coil currents to determine which sign of the magnetic field gradient makes the MOT work.

A polarization analyzer was used to set the circular polarizations. It consisted of a polarizing beam splitter cube (PBSC) and a quarter wave plate. For a quarter wave plate, if the angle between the polarization of the incident linearly polarized beam and the wave plate axis of the quarter wave plate is 45^o, the emergent beam is circularly polarized. Keeping the same waveplate angle, if the light is double passed through the waveplate, i.e. by mirror reflection, the waveplate will rotate the plane of linear polarization to an angle of 90^o. Using this method, the MOT beam was sent through the PBSC and then the quarter wave plate and was reflected by a mirror which was placed right after the wave plate. To initially

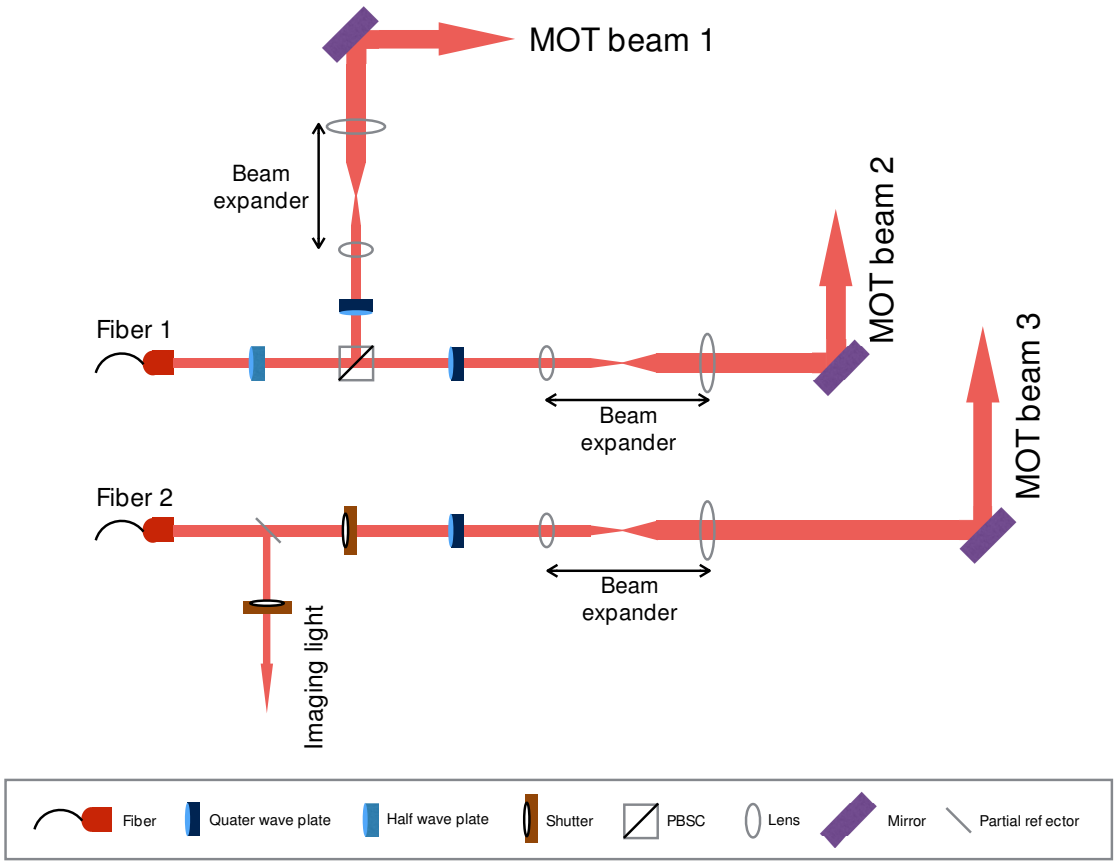

Figure 4.5: Experimental configuration for the three MOT beams on the BEC table.

set the quarter wave plate's orientation, the wave plate was then rotated to maximize the power of the reflected beam out of the PBSC.

To make the MOT beams circularly polarized correctly, the beams were sent through the wave plate of the analyzer. Then the quarter wave plates from Figure 4.5 were rotated to maximize the output beam power from PBSC. The output beam could either pass through the PBSC or reflect from it. Which one depended on which of the two circular polarizations was present.

4.6 Magnetic coil

In the previous chapter, we discussed the necessity of a magnetic field for trapping the atoms. Therefore, a suitable magnetic field gradient was important for making BEC successfully. The MOT magnetic field was provided by a pair of coils called the "main coils" which were 6 inches in diameter, and were setup in an anti-Helmotz configuration (identical coils separated by a distance equal to their diameter with current flowing in opposite directions). The coils had 25 turns of copper tube with a square cross section of external dimension of 0.125 inch and internal dimension of 0.016 inch. They were designed in such way that coolant could circulate internally, so a large current could be applied if needed without worry about the overheating of the coils. In our experiments, a 16 A current was supplied to trap and cool atoms. An inhomogeneous magnetic field between the coils was produced with a field gradient of about 16 G/cm and a zero field at the center of the chamber as shown in Figure 4.6. The current was supplied by a remotely programmable Lambda ESS 45-333-2-D DC power supply which required a three phase 190-250 V, 60 A AC input. The power supply was reconfigured so that it was able to supply up to 400 A DC current controllable with an external 0 V to 5 V analog signal. The resistance of the copper tube in main coils was 2.356 mΩ/m so the total resistance of a coil was only 28 mΩ (L = 12m). With the help of this information, a cooling system can be designed according to the estimation of the heat energy developed in the coil.

Three pairs of nulling coils were positioned on six sides of the chamber to counteract the Earth's magnetic field and any stray field produced by other sources. The coils in a pair had current flowing in the same direction and each pair was controlled by a different DC power supply. The MOT position could be moved with the nulling coil currents because the position of the zero of the magnetic field was changed by the application of an offset field.

4.7 CO_2 laser

The far off-resonance trap (FORT) was realized by a 50 W Coherent GEM Select 50 CO_2 laser. Because of its 10.6 μm wavelength, the laser was far detuned from the atomic resonance and its effect on the atoms could be approximated to that of a static electric field. The output CO_2 laser power, after a 40 MHz RF-driven AOM, was 30 W on the first order which overlapped the MOT for a loading time of typically 20 seconds. The MOT beam detuning was then increased to -78 MHz for optical molasses cooling. Then the repump power was decreased to produce a temporal dark MOT. Atoms started entering into a state that is "dark" to the cooling light during this step. The resultant decrease in the recoil heating and excited state collisions lead to an increase in the phase space density. After about 100 ms, the MOT and repump beams were cut off and the magnetic coil current switched off too.

4.7.1 CO_2 laser configuration and alignment

The CO_2 beam was passed through a water cooled Intra Action Corp. Model AGM-406B1 AOM driven by Intra Action Modulator Driver Model GE-4030H which was electronically controlled by using an analog voltage signal from the computer. We placed the AOM as close as possible to the laser head in order to minimize the diffractive divergence of the beam due to the long wavelength. The zeroth order beam after the AOM was sent into a beam dump, while the first order beam after the AOM which was about 30 W was directed into the chamber through three lenses. The first two lenses formed a beam expender in a

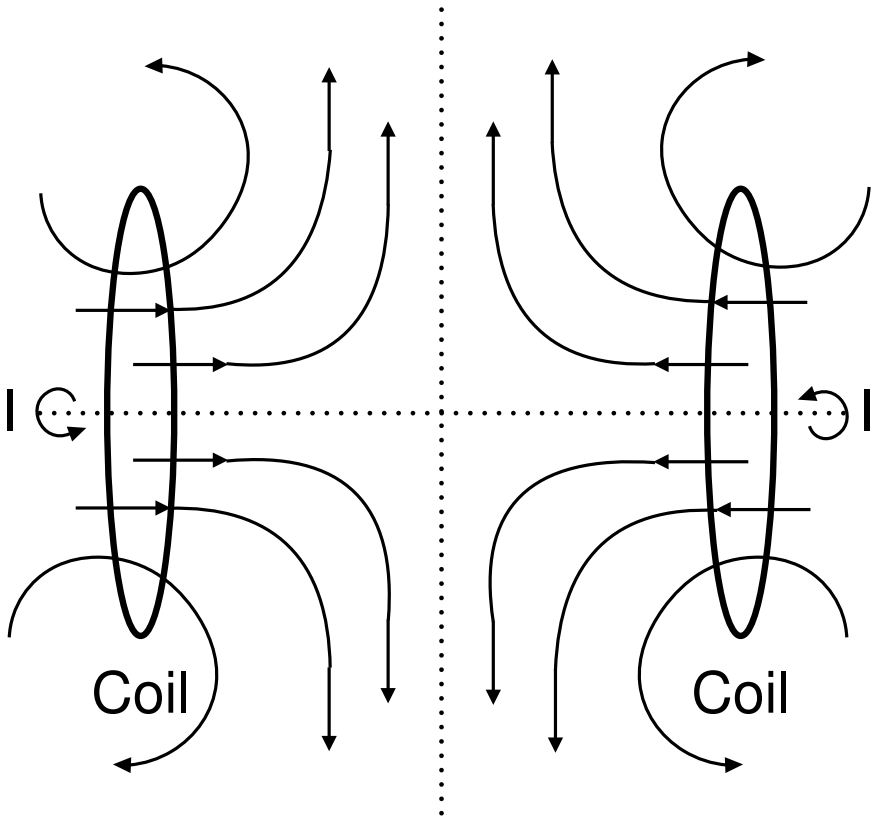

Figure 4.6: Schematic drawing of the coil system. The pair of coils is placed in anti-Helmholtz configuration.

telescopic configuration. The third lens with a focal length of 1.5 inches was installed in the chamber. The beam was directed into the chamber through a 1 inch diameter ZnSe viewport. At the center of the chamber, the final spot size of the beam was $\omega_0 = \frac{\lambda f}{\pi R}$, where f is the focal length of the lens and R is the radius of the beam incident on the third lens. For the processes of loading and evaporation, the beam waist was set large and small respectively. In order to change the beam size in experiments, the second lens was mounted on an Aerotech translation stage Model 101SMB2-HM driven by a Soloist driver interface, as shown in Figure 4.7. The beam emerging from chamber was sent into a dump for safety.

Though the configuration of the CO_2 system was simple, the alignment was not easy because of its invisibility to the eye and the dangerous high power. The method used for CO_2 laser alignment was to send a low power visible laser (HeNe laser) in the reverse direction all the wayback to the CO_2 laser head. Because the MOT was formed at the center of the chamber, the HeNe laser was sent from the dump position through the center of both the ZnSe viewports. Then the HeNe laser was sent through the center of the lenses and back the CO_2 laser by mirrors with two pinhole apertures used to define the beam path. The last step was removing the HeNe laser and sending the CO_2 laser through the same apertures by adjusting the mirrors before the apertures. After this procedure the CO_2 beam almost passed through the center of the ZnSe viewports and hence through the position where MOT was placed. It was important to know that the CO_2 beam center must stay at the same point before and after moving the translation stage. To check if the CO_2 beam was aligned with the MOT, we usually reduced the MOT detuning to about -23 MHz, and turned on and off the light every 500 ms. If we saw a flashing line through the MOT, the beam was at the right position. If not, we slowly modified the three nulling coil currents to move the MOT around until we saw the flashing line through the MOT.

4.7.2 Optics and detection

Because of the high absorption of glass and quartz at the 10.6 μm wavelength of the CO_2 laser, the usual optics were not useful for the CO_2 laser system. One of the materials

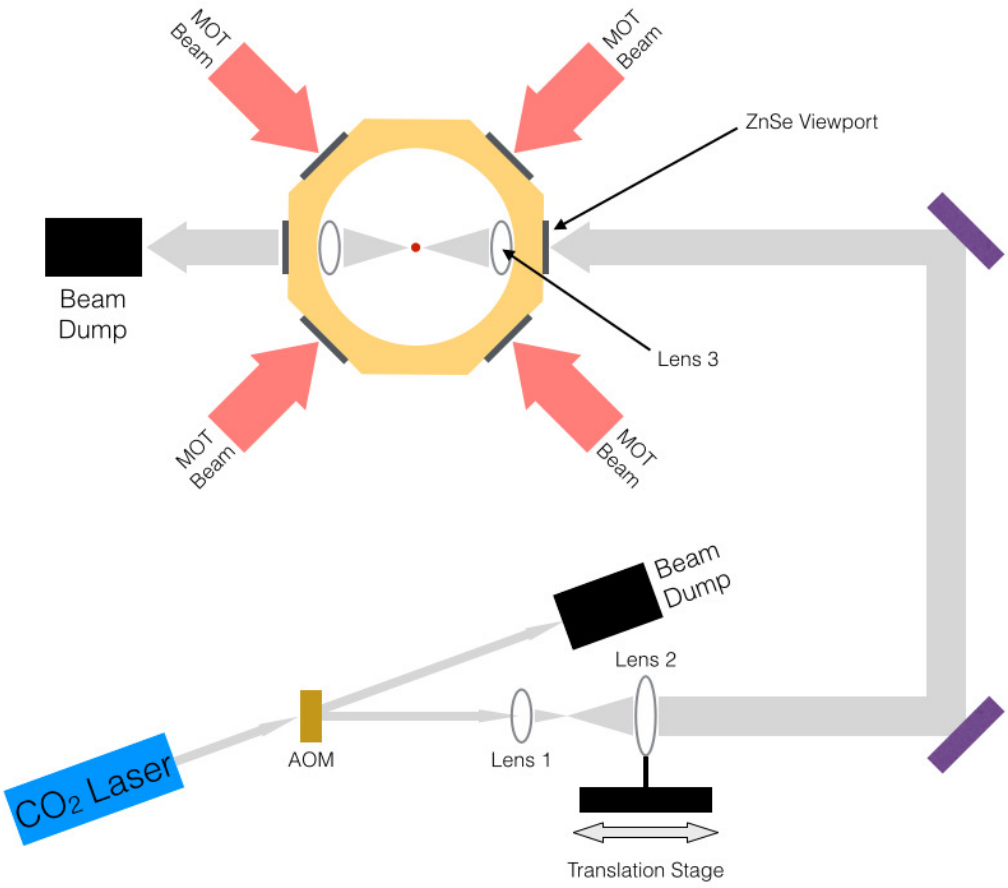

Figure 4.7: CO_2 laser beam setup.

with the lowest absorption coefficient at this wavelength was Zinc-Selenide (ZnSe). We used thermal plates to detect and align the beam. Thermal image plates were made with an anodized aluminum heat sink overlaid with thermal sensitive phosphor. When these thermally sensitive phosphor plates were exposed to infrared laser radiation, the absorbed energy raised the surface temperature and produced corresponding thermal images. These images appeared as dark spots when illuminated by ultraviolet light (3600 nm), and the darkness of the spot increased with laser power. A MACKEN Instruments' Lamp Model 22-UV was used to sensitize the plates.

4.8 Imaging system

In order to observe and measure the number of atoms, we used the method of absorption imaging. The absorptive technique was based on the resonant interaction of the light with the atoms. From fiber 2, a small portion of light known as the "imaging light" (shown on Figure 4.5) was on resonant with the atomic transition from $5^2S_{1/2}$, $F = 2 \rightarrow 5^2P_{3/2}$, $F' = 3$. The beam was expanded to 1 cm diameter by two lenses and was passed through a quarter wave plate to make it circularly polarized. The atoms were exposed to a weak 50 to 60 μs pulse from imaging light. The intensity of the beam is reduced when the atoms scatter photons from the imaging beam. Therefore the atoms cast a shadow in the beam which was imaged onto a high resolution CCD camera ANDOR DV437-BV which was cooled to -20^o to reduce dark count noise. The imaging configuration is shown on Figure 4.8. A 4$\times$ microscopic objective was used to magnify the image (Boiron *et al.*, 1998; Silvera and Walraven, 1980). The other two lenses are used to collimate the imaging beam. Two security CCD cameras were used to monitor the MOT in real time.

In order to calculate the number of the atoms, we calculated the absorption rate for a low power beam ($I \ll I_s$) traveling in the z-direction

$$\frac{dI}{dz} = -\sigma n I, \tag{4.2}$$

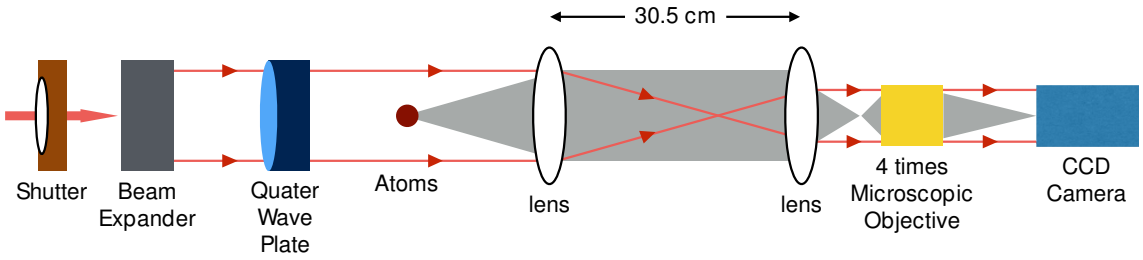

Figure 4.8: The setup of the imaging system.

where n is the density of atoms and I is the imaging beam intensity. $\sigma = \frac{\hbar\omega\gamma}{2I_s} = \frac{3\lambda^2}{2\pi}$ is the scattering cross section, where ω is the laser frequency, γ is the natural linewidth, and I_s is the saturation intensity. From equation 2.2, the intensity is

$$I(x,y) = I'_o(x,y)\exp(-\sigma\tilde{n}), \tag{4.3}$$

where $\tilde{n}$ is the column density (atom number per unit area). In order to find the intensity $I(x,y)$, we usually took two images each time. The two images were taken with and without atoms which gave intensity I_1 and I_0 respectively. The intensity profile is given as

$$I(x,y) = \frac{I_0}{I_1}. \tag{4.4}$$

By integrating over the column density, the atom number is

$$N = -\frac{S}{\sigma}\sum_{pixels}\ln(I), \tag{4.5}$$

where S is $13\mu m^2$ and is the scaled area of a pixel for the CCD camera. A Gaussian fit to the absorption profile determined the atom cloud size.

4.9 Bose-Einstein condensation procedure

Let us now examing the procedure for creating a BEC. To start an experiment about 30 million atoms were trapped in the MOT. The first order diffracted beam from the AOM with a power 30 W was overlapped with the MOT for about 20 seconds. Then the MOT beam detuning was decreased to -78 MHz for optical molasses cooling. This was followed by reduction of the repump intensity by a factor of at least 10 to produce a temporal dark MOT (Kuppens *et al.*, 2000; Ketterle *et al.*, 1993). After about 100 ms, the MOT beams and repump beams were extinguished and the magnetic coil current was turned off simultaneously. After the FORT loading, the FORT beam was compressed such that its waist decreased from 100 μm to 25 μm in a time of about 1 seconds. This increased the

elastic collision rate and hence the efficiency of the evaporative cooling. About 600,000 atoms were loaded in the FORT at this point. The atoms were then subjected to forced evaporative cooling where the trap depth was lowered at an exponential rate by reducing the CO_2 laser beam power to around 1 W. This took 2 seconds and was called "evaporative cooling 1". The following step, "evaporative cooling 2", involved the reduction of laser power in a series of tiny steps, after each of which the atoms were allowed time to rethermalize. The power was reduced to about 50 mW in 3 seconds and a pure condensate with around 40000 atoms in the $5^2S_{1/2}$ $F = 1$ ground state was produced. To take an image of the BEC, the repump beam was turned on again to pump the atoms of the BEC to the $5^2S_{1/2}$ $F = 2$ state. After 9 ms of expansion, a 100 ns pulse of on-resonance imaging light shone on the BEC. Because of absorption, the shadow of the BEC was observed on the CCD camera.

4.10 Kicking system

Kicking was one of the most important research tools for the experiments described in this report. The kicking laser was derived from a slave laser which was injection locked to the transition from the $5^2S_{1/2}$ $F = 2$ ground state to the cross over line between the $5^2P_{3/2}$ $F' = 2$ and $F' = 3$ excited state. The setup of the kicking laser is shown in Figure 4.3. Referenced to the $5^2S_{1/2}$ $F = 1$ ground state of the BEC, this light was 6.835 GHz red detuned (shown in Figure 4.2). The kicking laser was transported to the BEC table by a single mode polarization preserving fiber. On the BEC table, the kicking beam out of the fiber was split into two beams by a non-polarizing beam splitter cube. Each of these beams was separately passed through an Isomet Model 40N AOM. The first order diffracted beams out of the AOMs both had powers of about 5 mW. This light was directed into the vacuum chamber from two sides to form a horizontal standing wave. To increase the standing wave amplitude, lenses were used to focus the beams at the center of the vacuum chamber. Half-wave plates were used to ensure that the electric field vector of the beams was horizontal so they could interfere and produce the standing wave. Each beam was aligned so that it

made 53^o with the vertical forming a standing wave with a spatial periodicity of

$$\lambda_G = \frac{\lambda}{2\sin 53^o}, \tag{4.6}$$

where $\lambda = 780$nm.

The rf waveform driving each AOM was supplied by an arbitrary waveform generator HP8770A which passed through a 1 W amplifier. The first order laser beam diffracted by the AOM was frequency shifted by an amount equal to the frequency of the driving rf signal. One of the AOMs was driven by a function generator HP8770A at a fixed 40 MHz frequency, while the other AOM was driven at a variable frequency by a separate HP8770A which was phase-locked to the first one. Each of these function generators was programmed using a GPIB interface card, so all of the RF waveform properties could be directly controlled from a LabView program. By adjusting the variable part of the frequency

$$\omega_D = \frac{2\pi}{T_{1/2}}\beta + \frac{1}{2}Gat, \tag{4.7}$$

where $G = \frac{2\pi}{\lambda_G}$ was the grating vector of the standing wave and $T_{1/2}$ was the half Talbot time, the initial momentum β, and acceleration a of the standing wave were all controllable.

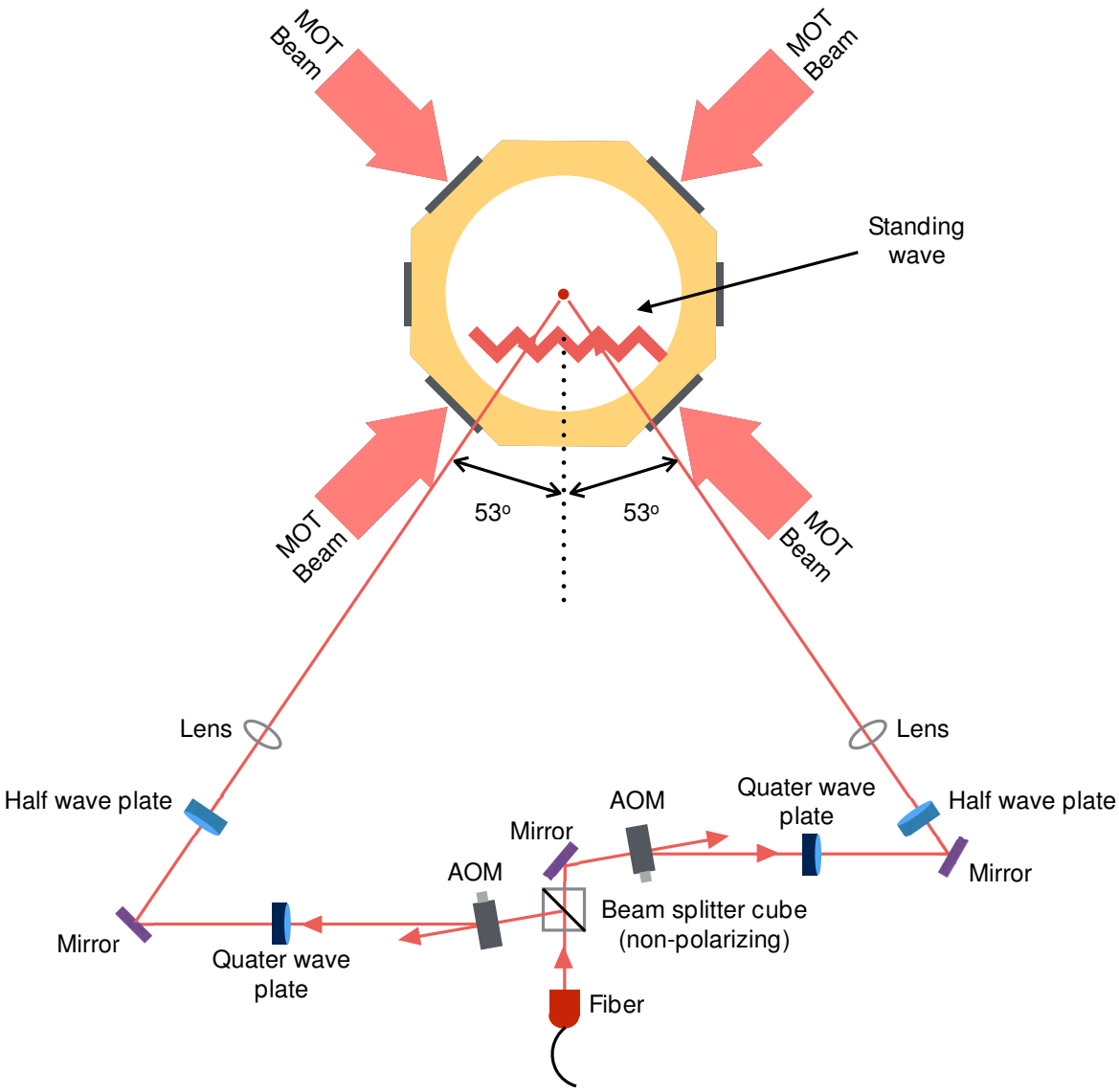

Figure 4.9: The setup of the kicking system. The two laser beams were sent into the vacuum chamber making 53^o to the vertical.

CHAPTER V

FIDELITY OF QUANTUM STATE EVOLUTION

It is interesting to know how stable are quantum states under the application of a small perturbation. Peres was one of the first to discuss the stability of quantum motion in chaotic and regular systems in 1984 (Peres, 1984). The evolution of a quantum state is altered when a small perturbation is added to the Hamiltonian. As time goes on, the overlap of the perturbed and unperturbed states shows an indication of the stability of quantum motion. Peres argued that if a quantum system has a regular classical analog (regular Hamiltonian), the overlap remains appreciable on a time average with large fluctuations. On the other hand, if a quantum system has a chaotic classical analog (chaotic Hamiltonian), the overlap tends to be small and its fluctuations are small too. This research is meaningful for the study of quantum information processing and transmission where the degradation of quantum information is critical. The fidelity of the quantum states with different perturbation is discussed.

5.1 Fidelity of quantum evolution

The quantum δ-kicked rotor (QDKR) has proved to be a paradigmatic model to study the overlap of perturbed and unperturbed quantum states. The Hamiltonian describing the

dynamics of the QDKR in dimensionless units is

$$\mathcal{H} = \frac{\hat{p}^2}{2} + \phi_d[1 + \cos(\hat{x})] \sum_{q=1}^{N} \delta(t - q\tau). \tag{5.1}$$

The wave function after t kicks is given as

$$\begin{aligned} |\psi(t' = t\tau)\rangle &= \hat{U}^N |\psi(t = 0)\rangle \\ &= \sum_n c_n |n\rangle. \end{aligned} \tag{5.2}$$

Here $\hat{U}$ is the Floquet operator as seen in equation 3.25, $|n\rangle$ are momentum eigenstates in units of $\hbar G$.

Another wave function after t kicks with a different kicking strength is given as

$$\begin{aligned} |\varphi(t = N\tau)\rangle &= \hat{U}^N |\varphi(t = 0)\rangle \\ &= \sum_n b_n |n\rangle. \end{aligned} \tag{5.3}$$

The overlap between the eigenstates of the two wave functions is

$$\begin{aligned} F &= |\langle\varphi|\psi\rangle|^2 \\ &= \left| \sum_n b_n^* c_n \right|^2, \end{aligned} \tag{5.4}$$

which is how we define a "fidelity".

For simulation, we should expand the Floquet operator. For the kick operator (as shown in equation 3.29), in the case when a random phase shift is introduced into the model, we need to replace the term $\cos(\hat{x})$ with $\cos(\hat{x} + \phi_{rnd})$. Therefore in the form of a matrix, the

kick operator is

$$\begin{aligned}\hat{U}_{kick} &= e^{-i\phi_d \cos(\hat{x}+\phi_{rnd})} \\ &= e^{i\phi_{rnd}} \sum_{n=-\infty}^{+\infty} i^n J_n(\phi_d) e^{in\hat{x}} \\ &= e^{i\phi_{rnd}} \sum_{n=-\infty}^{+\infty} \sum_{m=-\infty}^{+\infty} i^{n-m} J_{n-m}(\phi_d) |n\rangle\langle m|. \end{aligned} \tag{5.5}$$

For the free-evolution operator, the momentum p can take any value in real space, which can be separated as an integer part n and a fractional part β. Therefore,

$$\begin{aligned}\hat{U}_{free} &= e^{-i\frac{\hat{p}^2}{2}\tau} \\ &= \sum_{\nu=-\infty}^{+\infty} e^{-i\frac{(n+\beta)^2}{2}\tau} \delta_{f\nu} |f\rangle\langle\nu|. \end{aligned} \tag{5.6}$$

By applying the expanded Floquet operator to equation 5.3, the wave functions can be solved and furthermore the fidelity can be determined.

5.2 Simulation and experiment data analysis

In the preliminary experiments, the time between pulses was not chosen to be the Talbot time (or an integer multiple thereof), which meant the dynamics of the kicked rotor in phase space could not be described by classical δ-kicked rotor (equation 3.21 and equation 3.22). For off-resonance time intervals τ ($\tau = 2\pi\ell + \epsilon$), ϵ-classical theory (where the time between pulses is off from but still close to the Talbot time) should be applied. The dynamics can be given as (Fishman *et al.*, 2003; Sadgrove *et al.*, 2005)

$$\theta_{q+1} = \theta_q + J_q \tag{5.7}$$

$$J_{q+1} = J_q + \tilde{k}\sin(\theta_{q+1}), \tag{5.8}$$

where $\tilde{k} = |\epsilon|\phi_d$ is a scaled kicking strength, $J_q = \epsilon p_q + \ell\pi + \tau\beta$ is the scaled momentum variable, and $\theta = X \bmod (2\pi) + \pi[1 - sign(\epsilon)]/2$ is the scaled position, exploiting the spatial

periodicity of the kick potential. Figure 5.1 shows the ϵ-classical maps with different kicking strength ϕ_d. Here the time between pulses was 70 μs, thus $\epsilon = 2.1842$. It is clear that as the ϕ_d increases, the main island at the center of the map is smaller and smaller.

We introduced a perturbation to the system by applying different kicking strength ϕ_d. To see how a perturbation effects the evolution of quantum states, a BEC was kicked by a standing wave with ϕ_{d1}, and another BEC with the same initial momentum $\beta = 0$ was kicked by a standing wave with ϕ_{d2} which was slightly different from ϕ_{d1}. Figure 5.2 shows the simulation with ϕ_{d1} fixed at 0.7 and ϕ_{d2} increased from 0.75 to 1.0. Therefore the $\delta\phi_d$ is from 0.05 to 0.3. The simulation tells us the fidelity decay rate becomes bigger when the ϕ_d difference increases. This can be easily understood by connecting the fidelity to the maps showed in Figure 5.1. When the perturbation is large, i.e. the ϕ_d difference is large, the BEC overlaps more of the chaotic part of the phase space. The islands in Figure 5.1 with a bigger kicking strength are much smaller than those with smaller kicking strength, so the BEC overlaps more chaotic regions of phase space. Thus the fidelity in Figure 5.2 should decay faster. However, when the perturbation is small and the ϕ_d difference is small, the possibility for the system to stay in the island is higher since the island is bigger. Therefore the fidelity is expected to decay slower.

The effect of finite pulse length can also be important. Though the kicking pulse is assumed as a δ-kick, in a real experiment this is not possible. This can result in a different evolution. Figure 5.3 shows the fidelity with different pulse lengths which increase from 1.024 μs to 1.624 μs with interval 0.2 μs. Here $\phi_{d1} = 0.7$ and $\phi_{d2} = 0.85$. From the figure, it can be seen that the fidelity decays faster as the pulse length increases. Figure 5.2 shows the fidelity decays faster with bigger ϕ_d.

Experiments were taken with parameters that matched those of the simulation. The time between pulses was 70 μs, initial momentum $\beta = 0$, and the standing wave pulse length was 1.024 μs. Atoms were kicked out of the $p = 0$ state with kicking strength ϕ_{d1} and diffracted into the other momentum states. Then the atoms were kicked by another set of kicks with kicking strength ϕ_{d2} as shown in Figure 5.4. Fidelity was the quantity to measure

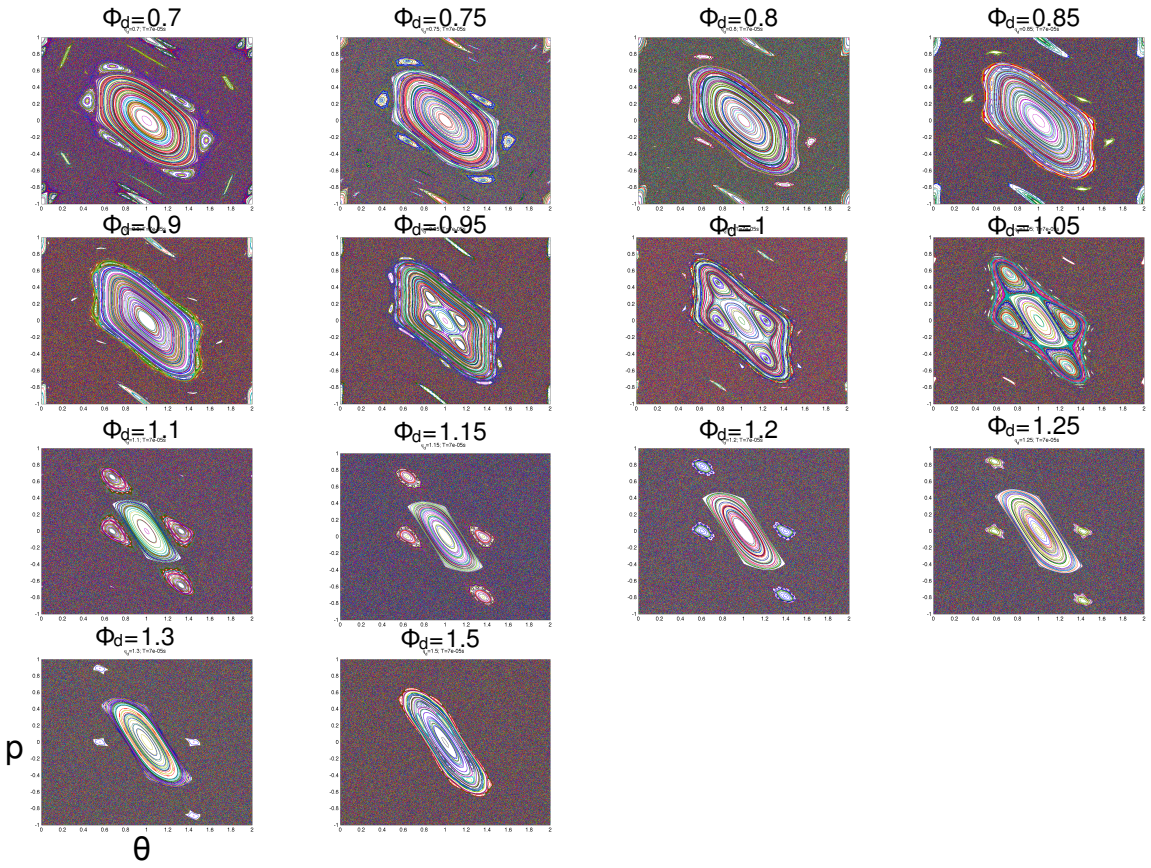

Figure 5.1: T is 70μs for all of the maps here, which means $\epsilon = 2.1842$. The ϕ_d for each of them are from 0.7 to 1.5 with interval 0.05. It is clear that as the ϕ_d increases, the main island at the center of the map is decreasing. The region out of the island is chaotic.

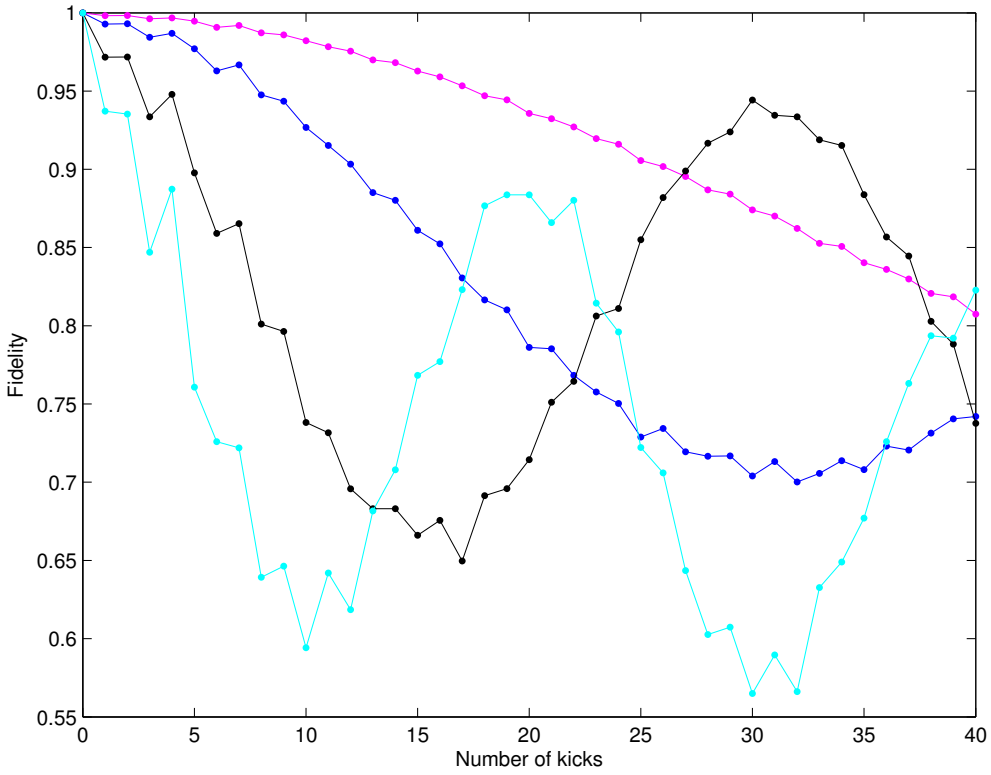

Figure 5.2: ϕ_{d1} is fixed at 0.7, while ϕ_{d2} for the purple curve is 0.75, for the blue curve is 0.8, for the black curve is 0.9, for the cyan curve is 1.0.

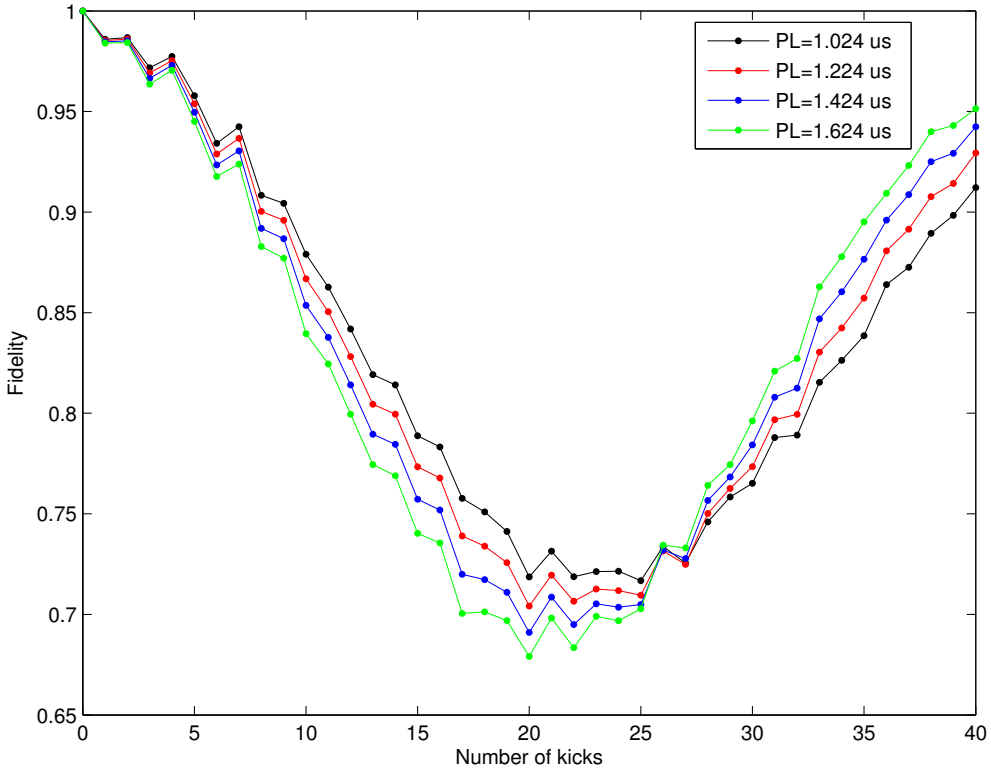

Figure 5.3: With longer pulse length, fidelity decays faster.

the overlap between the two sets of kicking as shown in Figure 5.5. The way we calculate fidelity in the experiment was:

$$F = \sum_n \sqrt{\frac{p_{n1}p_{n2}}{p_{t1}p_{t2}}}, \tag{5.9}$$

where p_{n1} was the number of the atoms on state n with the first set of kicks of ϕ_{d1}, p_{n2} was the number of the atoms on state n with the second set of kicks of ϕ_{d2}, n was the order of the state, and p_{t1} and p_{t2} were the total number of atoms in all the states for the two sets of kicking evolution. It can be seen that the experiment data matches the simulation quite well. The random phase noise due to spontaneous emission $p = \frac{8\Gamma}{\delta}\phi_d = 0.007\phi_d$ was considered in simulation as well.

5.3 Future research

One of the main objects in the future is to prepare a superposition of two identical initial states for the experiment. In the current experiments, we start from a BEC under identical environment. Though the BECs are the same, we cannot assume that they are in the same initial momentum states in phase space. According to the dynamics shown by Eq. (5.7) and Eq. (5.8), maps are different with different kicking strength. Therefore the two BECs are not in the same map and are incomparable. In Peres' proposal, the initial states with and without perturbation are the same, which means the experiment should start from the same point on the phase space. For this reason, to prepare a superposition of two BECs simultaneously Bragg pulse may be used in the future. A Bragg pulse is a long and weak intensity pulse which creates a superposition of two momentum states. Furthermore, to kick the two BECs simultaneously, two optical standing waves from two pairs of kicking beams will be prepared as well. The second pair of kicking beams will be sent into the vacuum chamber with a different angle between the two beams, thus the grating vector can work on the second BEC.

Another thing that needs careful consideration is that the maps shown in Figure 5.1 were drawn assuming ϵ-classical theory. The pulse period T, the time between pulses, was 70 μs

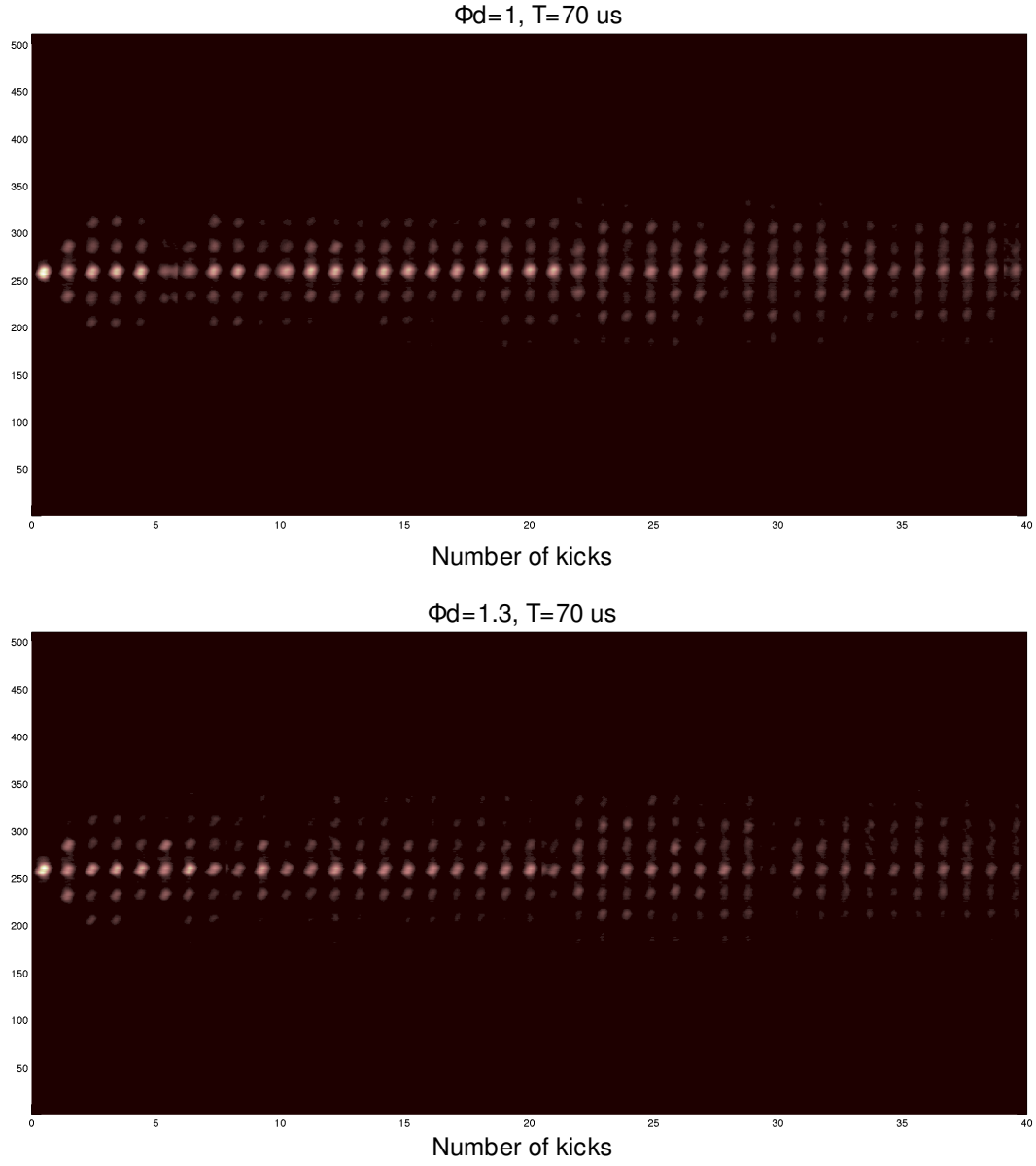

Figure 5.4: The "big pictures" of momentum distribution of the experiments. It shows how atoms evolve as time goes on. For the top picture, kicking strength was 1; for the bottom picture, kicking strength was 1.3. The time between the pulses for both of the picture was 70 μs.

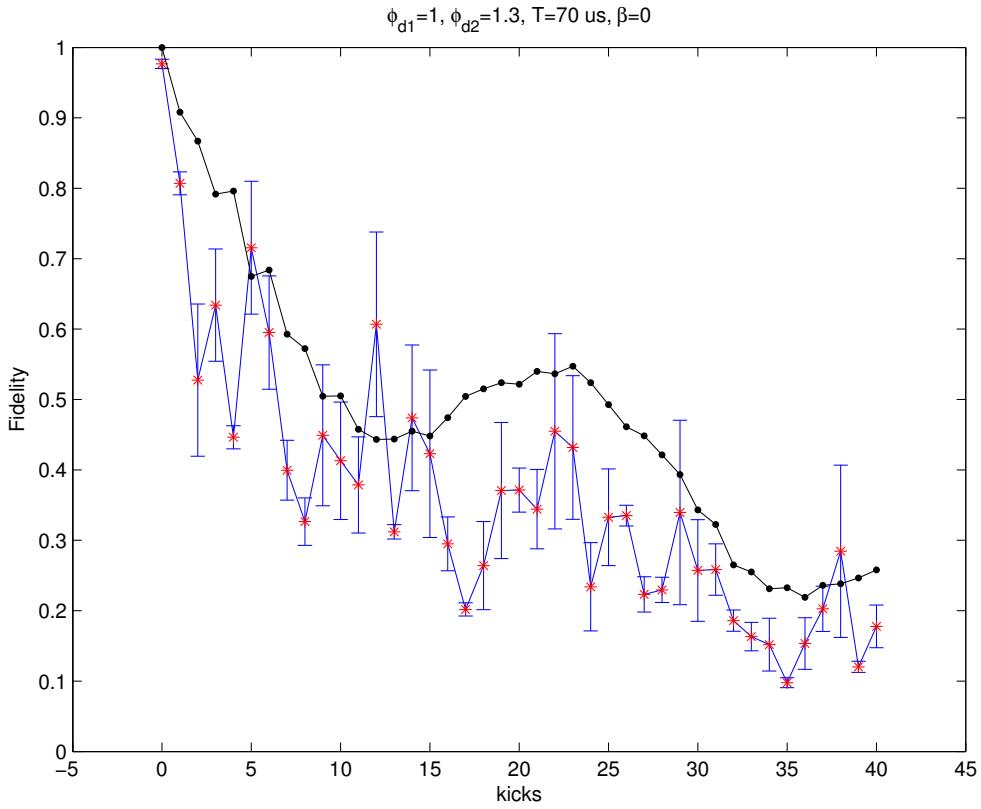

Figure 5.5: Experimental data for fidelity v.s. simulation. Red stars with error bars are experimental data; black dots were simulation.

which is far from the Talbot time of 103 μs. Thus the classical map shown of Eq. (5.7) (5.8) are not really suitable. There is a limitation for the ϵ-classical theory's validity which is $|\epsilon| << 1$. For $T = 70\mu s$, ϵ is 2.26 and is really too large to use ϵ-classical theory. In the future, we will try the very general map without any scaling to plot the dynamics of the atom. We also plan to take more experimental data closer to the Talbot time resonances.

CHAPTER VI

QUANTUM-RESONANCE RATCHETS WITH DIFFERENT INITIAL STATES

6.1 Introduction

Understanding the nature of quantum transport is an important problem in physics especially for quantum chaos. The delta-kicked rotor, an ideal system for studying quantum transport, is realized by exposing a sample of cold atoms to short pulses of an optical standing wave. This is the so-called atom optics quantum kicked rotor (AOQKR) (Moore *et al.*, 1994). The implementation of the AOQKR in experiments was a breakthrough in the study of quantum chaos, and the system has now been widely used in elucidating phenomena like dynamical localization (Moore *et al.*, 1994), quantum resonances (QRs) (Moore *et al.*, 1994; Ryu *et al.*, 2006; Izrailev, 1990), quantum accelerator modes (QAMs) (Fishman *et al.*, 2002, 2003; Behinaein *et al.*, 2006; Ramareddy *et al.*, 2010; Oberthaler *et al.*, 1999; Shrestha *et al.*, 2013b), quantum fidelity (McDowall *et al.*, 2009; Shrestha *et al.*, 2013c; Ullah and Hoogerland, 2011; Talukdar *et al.*, 2010), and quantum ratchets (Monteiro *et al.*, 2002; Dana *et al.*, 2008; Sadgrove *et al.*, 2007a; Salger *et al.*, 2009; Astumian and Hänggi, 2002; Sadgrove *et al.*, 2007b; Dana and Roitberg, 2007; Schanz *et al.*, 2001; Lundh and Wallin, 2005; Wickenbrock *et al.*, 2011; Shrestha *et al.*, 2013a). The later are quantum-mechanical systems where currents of particles are produced without any biasing force. These ratchets have been proposed as mechanisms for Hamiltonian quantum ratchets (Salger *et al.*, 2009). In previous experimental observations of quantum ratchets (Dana *et al.*, 2008; Sadgrove

et al., 2007b; Shrestha *et al.*, 2012), it was found that only a relatively small component of the initial wave function was involved in the momentum current. It is therefore natural to ask if it is possible to improve upon the mode matching between the initial state and the ratchet state so as to increase the participation in the ratchet. One of our motivations for enhancing the efficiency of the quantum ratchet is the possible use of such a system as the walk in experiments on quantum random walks (Ma *et al.*, 2006; Summy and Wimberger, 2016).

The structure of this paper is as follows; we begin by providing a theoretical analysis of the intrinsic mechanism of a quantum ratchet. We then present the experimental realizations of the momentum currents using different initial states that have been prepared using Bragg diffraction with light pulses. We demonstrate how different phases on the initial state wave function can affect the momentum current. Finally, we examine how the momentum current depends on the number of momentum states in the initial wave function. In particular, we present results showing a connection between the number of momentum state components and the dispersion of the ratchet.

6.2 Theory

We start by summarizing the basic dynamics of the AOQKR system (Fishman *et al.*, 2003; Behinaein *et al.*, 2006; Talukdar *et al.*, 2010; Sadgrove *et al.*, 2005; Oskay *et al.*, 1999). The Hamiltonian in dimensionless unit is given by:

$$\hat{H} = \frac{\hat{p}^2}{2} + \phi_d V(\hat{x}) \sum_{t=1}^{N} \delta(t' - t\tau), \tag{6.1}$$

where $\hat{p}$ is the momentum in units of $\hbar G$ (two photon recoils). ϕ_d is the strength of the kicks, and is given by $\phi_d = \Omega^2 \triangle t/8\delta_L$, where $\triangle t$ is pulse length, $\Omega = \vec{\mu} \cdot \vec{E}(\vec{r})/\hbar$ is the Rabi frequency, and δ_L is the detuning of the kicking laser from the atomic transition. $V(\hat{x}) = \cos(Gx + \gamma)$ is the standing wave with a grating vector $G = 2\pi/\lambda_G$. λ_G is the spatial period of the standing wave, and is determined by the direction of the laser beams

as their wavelength. Here, x is position in units of G^{-1}, and γ is an offset phase. t' is the continuous time variable, and t counts the number of kicks. $\tau = 2\pi T/T_{1/2}$ is the scaled pulse period where T is the real pulse period and $T_{1/2} = 2\pi M/\hbar G^2$ is the half-Talbot time for an atom with mass M. The momentum is changed in quanta of $\hbar G$ in this system, and as a result p can be broken down as $p = n + \beta$, where n and β are the integer and fractional parts of the momentum respectively. β, also known as the quasi-momentum, is a conserved quantity .

A convenient picture of the ratchet mechanism can be derived by considering the gradient of the standing wave as the driving force on the wave function. From this standpoint, ensuring that the wave function is greatest at positions with larger gradients should produce stronger forces and the possibility of a ratchet, with the sign of the gradient determining the ratchet's direction. To create a spatially non-uniform atomic distribution, an initial state that is comprised of a superposition of two or more plane waves is used:

$$|\psi\rangle = \sum_n e^{in\pi/2}|n\rangle, \tag{6.2}$$

where $|n\rangle$ is equal to $|n\hbar G\rangle$. As will be seen shortly, the phase prefactors shift the maxima of the spatial wave function distribution to where the potential gradient is greatest.

Considering the case of a single Bose-Einstein condensation (BEC) for the initial state, the wave function in momentum space can be written as

$$|\psi(p)\rangle = e^{-i(p-p_0)^2/2\Delta p^2} \tag{6.3}$$

with $p_0 = 0\hbar G$. Here p_0 is the central initial momentum, Δp is the width of the BEC, and p is the continuous momentum variable. In order to study the wave function in the frame of the standing wave, we transform into position space by using a Fourier transformation. The wave function in position space is

$$|\phi(x)\rangle = Ae^{-2\Delta p^2(Gx)^2}e^{i\beta Gx}, \tag{6.4}$$

where A is the amplitude. For our BEC $\Delta p \ll 1$, so that $|\langle\phi(x)|\phi(x)\rangle|^2$ is close to a uniform distribution. Therefore there is no biased force and hence no ratchet (Moore *et al.*, 1994; Ryu *et al.*, 2006; Izrailev, 1990).

When the initial state contains two or more plane waves, the wave function in momentum space should be:

$$|\psi(p)\rangle = \sum_n e^{in\pi/2} e^{-i(p-p_n)^2/2\Delta p^2}. \tag{6.5}$$

The wave function in position space after a Fourier transform looks like:

$$|\phi(x)\rangle = \sum_n A_n e^{-2\Delta p^2 (Gx)^2} e^{i(\beta+p_n)Gx}. \tag{6.6}$$

By plotting $|\langle\phi(x)|\phi(x)\rangle|^2$ and the standing wave potential together, it is noticeable that peaks in the wave function arise at positions where the gradient of the standing wave happens to be the greatest (see Fig. 6.1). Naturally, the more plane waves contained in the initial state, the more localized the wave function should become. In Fig. 6.1, the bold solid line is the standing wave, the dashed and dotted lines are the wave functions in position space for the initial states with a superposition of seven plane waves: $\sum_{n=-3}^{3} e^{-in\pi/2}|n\rangle$ and two plane waves: $|0\rangle + e^{i\pi/2}|1\rangle$ respectively. The dashed line is much taller and has a reduced full width at half maximum (FWHM). Figure 6.2 shows that as the number of the plane waves in the initial state increases, the corresponding FWHM of the wave function decreases. Since a peak with larger FWHM experiences a smaller overall gradient and a larger variation in the gradient, we expect that a "cleaner" ratchet requires more plane waves in the initial superposition. The effective force

$$\int_{-\pi}^{\pi} |\phi(x)|^2 \, dV(x) \tag{6.7}$$

of the standing wave (integrate the absolute square of wave function with the standing wave gradient) for different initial states was also calculated. The dashed line in Fig. 6.2 shows that the effective force increases with the number of the plane waves in the initial state.

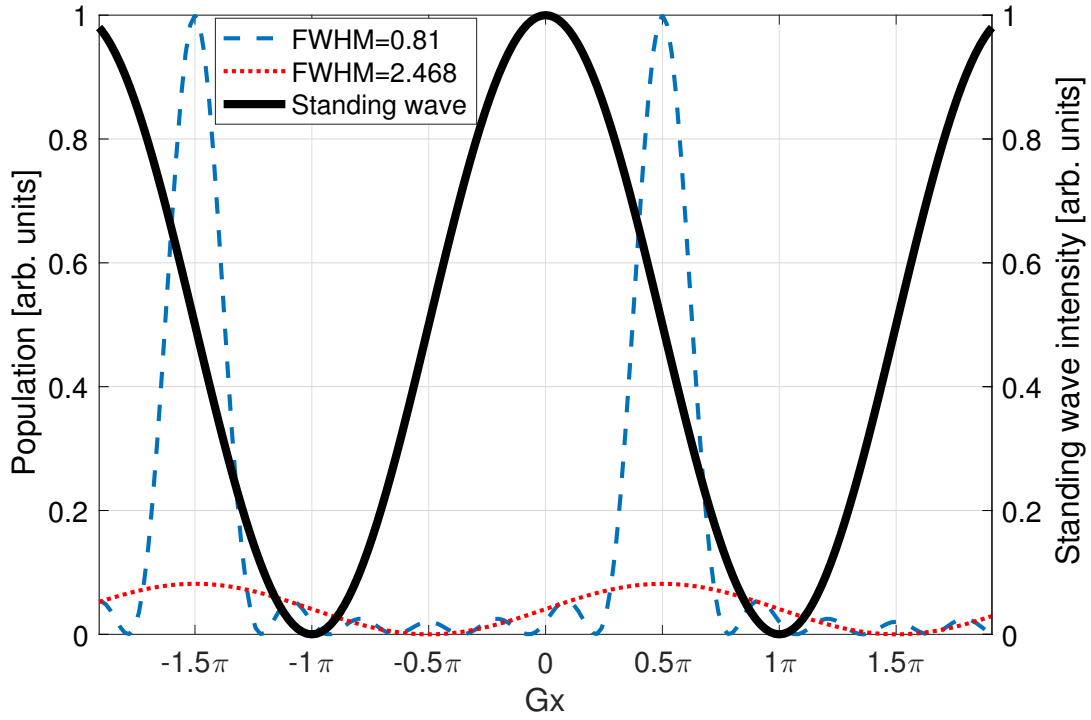

Figure 6.1: The solid line is the standing wave intensity for potential $V(\hat{x})$. The dashed line is the wave function for a superposition of seven plane waves: $\sum_{n=-3}^{3} e^{-in\pi/2}|n\rangle$. The dotted line is the wave function for a superposition of two plane waves: $|0\rangle + e^{i\pi/2}|1\rangle$. All the wave functions here were normalized using the $\sum_{n=-3}^{3} e^{-in\pi/2}|n\rangle$ in arbitrary units.

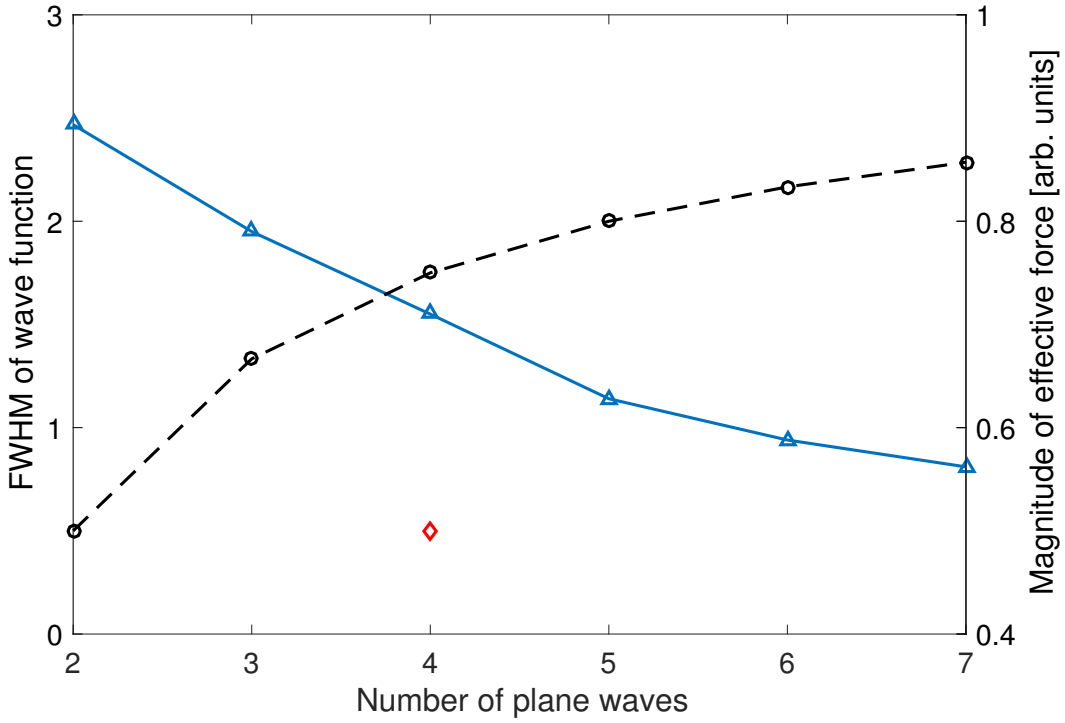

Figure 6.2: The solid line is the theoretical FWHM of wave function in position space vs number of plane waves, while the dashed line is the theoretical effective force of the standing wave. The diamond is the magnitude of effective force for initial state $e^{-i\pi}|-2\rangle + e^{-i\pi/2}|-1\rangle + e^{i\pi/2}|1\rangle + e^{i\pi}|2\rangle$.

To ensure the peak of the wave function appears at the right point of the standing wave: $Gx = \pi/2$, the phase for each plane wave is extremely important. As mentioned previously, it should be set to $e^{in\pi/2}$, where n is the momentum state index. If the phases differ from these values the peak of the wave function in position space will shift away from the greatest gradient and the driving force from the gradient of the standing wave will become weaker.

We also point out that to maximize the ratchet, the momentum states in the initial superposition should be consecutive. In another words, the momentum difference between neighboring momentum states should be $\hbar G$. The diamond in Fig. 6.2 is the magnitude of effective force for the initial state with four nonconsecutive momentum states, which is smaller than the one with four consecutive momentum states. Figure 6.3 shows the wave function in position space for initial states with a superposition of nonconsecutive momentum states. Note that besides the wave function peak at the greatest gradient point, there is also considerable wave function amplitude at positions where the gradient is zero or of opposite sign. This can provide explanation for why the ratchet is weak or even disappears in experiments with there initial states. The dashed line represents the initial state: $e^{-i\pi}|-2\rangle + e^{-i\pi/2}|-1\rangle + e^{i\pi/2}|1\rangle + e^{i\pi}|2\rangle$ and shows a relatively large peak at the greatest gradient point. Thus the ratchet effect should still exist although weaker than the ratchet of initial state with four consecutive momentum states. The dotted line represents the initial state: $e^{-i\pi}|-2\rangle + e^{i\pi}|2\rangle$, and shows no effective force. Finally, the dash-dot line is for the initial state: $e^{-i\pi/2}|-1\rangle + e^{i\pi/2}|1\rangle$. Note that the two wave function peaks appear at points where the positive and negative gradient is greatest on the standing wave. This suggests that we should expect two ratchets with opposite direction simultaneously.

6.3 Experimental setup

Our experimental apparatus is similar to the one described in Ref. [24]. A BEC with about 70,000 ^{87}Rb atoms was created in the $5S_{1/2}$, $F = 1$ hyperfine ground states in a focused CO_2 laser beam using an all-optical trapping technique (Chu *et al.*, 1986). The order of the ratio of the mean field energy to the recoil energy is about 10^{-5}, which put us in the region

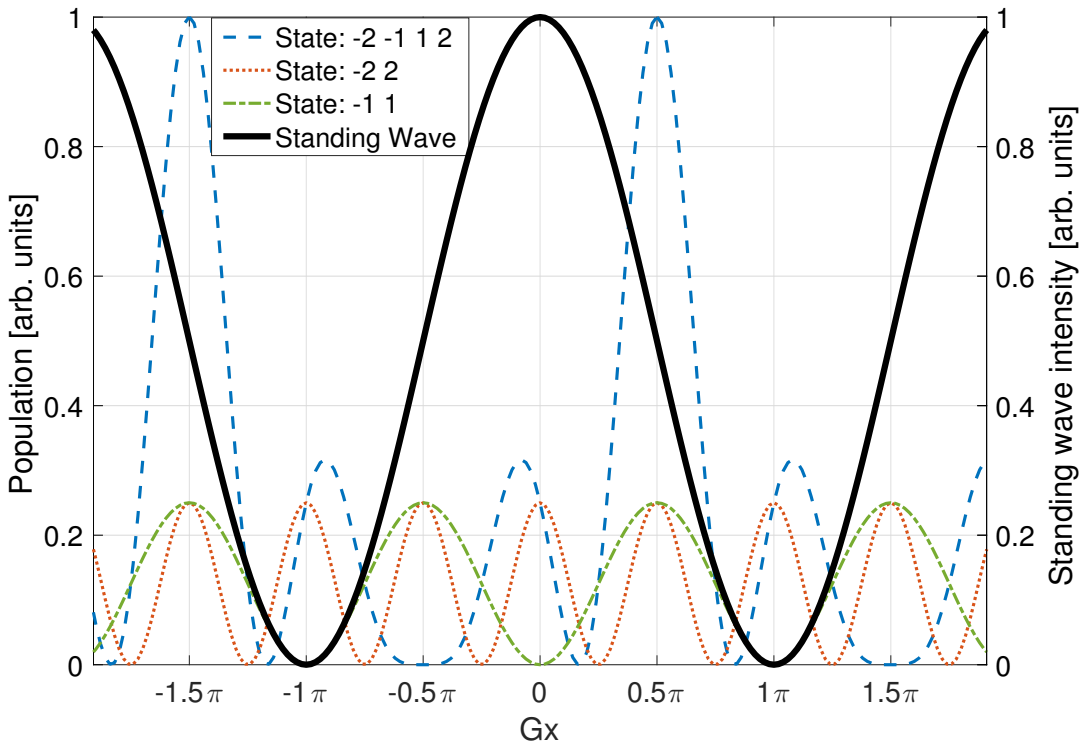

Figure 6.3: The solid line is the standing wave intensity for potential $V(\hat{x})$. The dashed line is the wave function for a superposition of nonconsecutive plane waves: $e^{-i\pi}|-2\rangle + e^{-i\pi/2}|-1\rangle + e^{i\pi/2}|1\rangle + e^{i\pi}|2\rangle$. The dotted line is the wave function for a superposition of nonconsecutive plane waves: $e^{-i\pi}|-2\rangle + e^{i\pi}|2\rangle$. The dash-dot line is the wave function for a superposition of nonconsecutive plane waves: $e^{-i\pi/2}|-1\rangle + e^{i\pi/2}|1\rangle$. All the wave functions here were normalized using the $e^{-i\pi}|-2\rangle + e^{-i\pi/2}|-1\rangle + e^{i\pi/2}|1\rangle + e^{i\pi}|2\rangle$ in arbitrary units.

that the nonlinearity is negligible and can be ignored. Immediately after the BEC was released from the trap, we applied a series of horizontal optical standing wave pulses. This standing wave was formed by two laser beams with a wavelength of $\lambda = 780$ nm, which was 6.8 GHz red detuned from the $5S_{1/2}$, $F = 1$ transition $\longrightarrow$ $5P_{3/2}$, $F' = 3$ transition. Each laser beam was aligned 53° from the vertical to give a standing wave with a spacial period of $\lambda_G = \lambda/(2\sin 53°)$. This led to a half-Talbot time of $T_{1/2} \approx 51.5$ μs, with the primary QRs falling at integer multiples of this time (Moore *et al.*, 1994; Ryu *et al.*, 2006; Izrailev, 1990). To create the necessary standing wave pulses, we controlled the phase, intensity, pulse length, and the relative frequency between the two laser beams. This was achieved by passing each of the standing wave's constituent laser beams through an acousto-optic modulator (AOM) driven by an arbitrary waveform generator. The nodes of the standing wave moved with a velocity given by $v = 2\pi\triangle f/G$ with $\triangle f$ being of the frequency difference of the two beams. The quasimomentum, β, of the BEC relative to the standing wave is proportional to v and therefore β can be controlled through $\triangle f$. The kicking pulse length was fixed at 0.576 μs to ensure that the experiments were performed in the Ramam-Nath regime. In other words, the distance momentum states traveled during a pulse was much smaller than the spatial period of the standing wave.

To prepare an initial state comprised of a superposition of several plane waves, a sequence of longer standing wave pulses were applied in the Bragg configuration (Torii *et al.*, 2000). Such pulses connect two momentum states with an interaction matrix given by

$$U = \begin{pmatrix} \cos(\frac{\Omega_B \tau_B}{2}) & -i\sin(\frac{\Omega_B \tau_B}{2})e^{i\gamma} \\ -i\sin(\frac{\Omega_B \tau_B}{2})e^{-i\gamma} & \cos(\frac{\Omega_B \tau_B}{2}) \end{pmatrix}, \tag{6.8}$$

where Ω_B is the effective Rabi frequency, τ_B is the Bragg pulse length, and γ is the phase. To see how these were utilized in our experiment, consider the preparation of a superposition of five momentum states. As shown in Fig. 6.4, in this case we need four Bragg pulses. The first Bragg pulse with initial quasi-momentum $\beta = 0.5$ diffracts atoms into states $|0\rangle$ and $|1\rangle$. The second Bragg pulse with $\beta = -0.5$ diffracts atoms into states $|0\rangle$ and $|-1\rangle$ without affecting the atoms in state $|1\rangle$. Similarly, the third and fourth Bragg pulses, with

$\beta = 1.5$ and $\beta = -1.5$, diffract atoms into states $|1\rangle$, $|2\rangle$ and $|-1\rangle$, $|-2\rangle$ respectively. All of the Bragg pulses were applied consecutively without dwell time between the pulses. There is considerable freedom in the choice of pulse length, however in our case this was set at 103 μs or a Talbot time. This ensured that the free evolution of each of the prepared states was always $\hat{1}$ while additional Bragg pulses were applied and could thus be ignored. The intensity for different Bragg pulses was carefully adjusted to make the population in each state equal. We complemented this scheme for superpositions comprising up to 7 states. To our knowledge such large superpositions have not been created previously and may have applications in atom interferometry (Kovachy *et al.*, 2010). There are two possible methods to select an appropriate phase for each momentum state so as to maximize the ratchet effect. One is to set the phase on each momentum state $|n\rangle$ according to $n\pi/2$. For example, with five momentum states, the phases on $|-2\rangle$, $|-1\rangle$, $|0\rangle$, $|1\rangle$, $|2\rangle$ should be $-\pi$, $-\pi/2$, 0, $\pi/2$, π. The other method of phase preparation is to set all of the momentum states with a phase of zero and then shift the position of the standing wave by a quarter of its spatial period. Because of the imaginary nature (i factor) of the off-diagonal elements of Eq. 6.8, a phase of $\pm\pi/2$ is automatically added to each state created by a Bragg pulse. This produces a phase of $-n\pi/2$ for states $n = ...-3, -2, -1, 0, 1, 2, 3....$ Therefore, for the first phase preparation method the phases added to the momentum states should be: -2π, $-\pi$, 0, π, 2π. Similarly, for the second methods, the phases added to the momentum states should be: $-\pi$, $-\pi/2$, 0, $\pi/2$, π. For simplicity, in our experiments we chose to set the offset phase of standing wave $\gamma = \pi/2$ and keep the phases of momentum states zero (see Fig. 6.4).

As can be seen from the previous discussion, the phases of the components of the superposition are extremely important for the ratchet dynamics. Hence it is critical that any unknown phases be controlled and if possible eliminated. To this end we implemented a $\pi/2 - \pi - \pi/2$ Mach-Zehnder Bragg interferometer (Torii *et al.*, 2000) with which we could measure such phases. In particular we were able to eliminate extraneous phase shifts due to gravity (non-horizontal standing wave) and ac-Stark shifts due to small amounts of stray light.

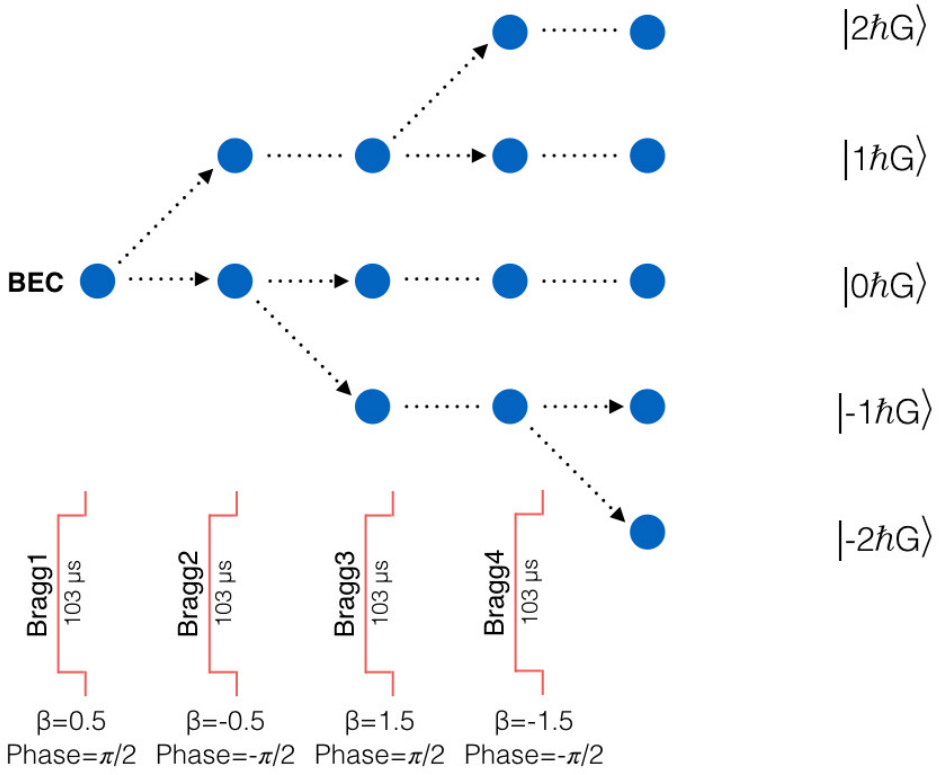

Figure 6.4: Experimental schematic showing preparation of the five component initial state: $\sum_{n=-2}^{2} |n\rangle$.

Following the Bragg preparation, the delta-like kick rotor pulses were immediately applied. These diffracted the atoms into a wide range of momentum states. For the kicking pulses, the pulse length was 0.576 μs, the pulse strength $\phi_d \sim 1.4$, the phase γ in the potential was $\pi/2$. The time between kicking pulses was 51.5 μs (half-Talbot time) with initial momentum $\beta = 0.5$ to maintain QR. In order to measure the momentum distribution after the pulse sequence, atoms were absorption imaged following a free flight time of 9 ms. Several examples of time-of-flight images of the BEC vs t are shown in Fig. 6.5.

6.4 Data analysis and discussion

We have performed a comprehensive experimental study of the dispersion of the momentum of BEC as function of several variables. Normalized dispersion of the momentum of BEC is defined as:

$$D(t) = \frac{\langle p_t^2 \rangle - \langle p_t \rangle^2}{\langle p_0^2 \rangle - \langle p_0 \rangle^2}, \tag{6.9}$$

where $\langle p_t \rangle$ is the mean momentum, $\langle p_t^2 \rangle$ is the mean of momentum square, and t is the kick number. The dispersion is used to describe the quality of the ratchet current: the closer $D(t)$ is to 1 the better the ratchet state maintains its initial form. Reducing change in the dispersion is an important property for applications, such as quantum random walk (Summy and Wimberger, 2016). We now discuss the sensitivity of the ratchet current dispersion to the initial state. Figure 6.6 shows the dependence of the dispersion on kick number t for $\gamma = \pi/2$, $\beta = 0.5$ and the time between kicking pulses $T = T_{1/2}$. The experimental results are in good agreement with the simulation and show that the more momentum states in the initial state, the smaller dispersion. In other words, to improve the quality of the ratchet we need to generate an initial state with a large number of plane waves in its superposition.

As discussed before, the ratchet is highly sensitive to the phase of the initial state. To illustrate this point experiments were carried out with the initial state $\sum_{n=-2}^{2} |n\rangle$ where an

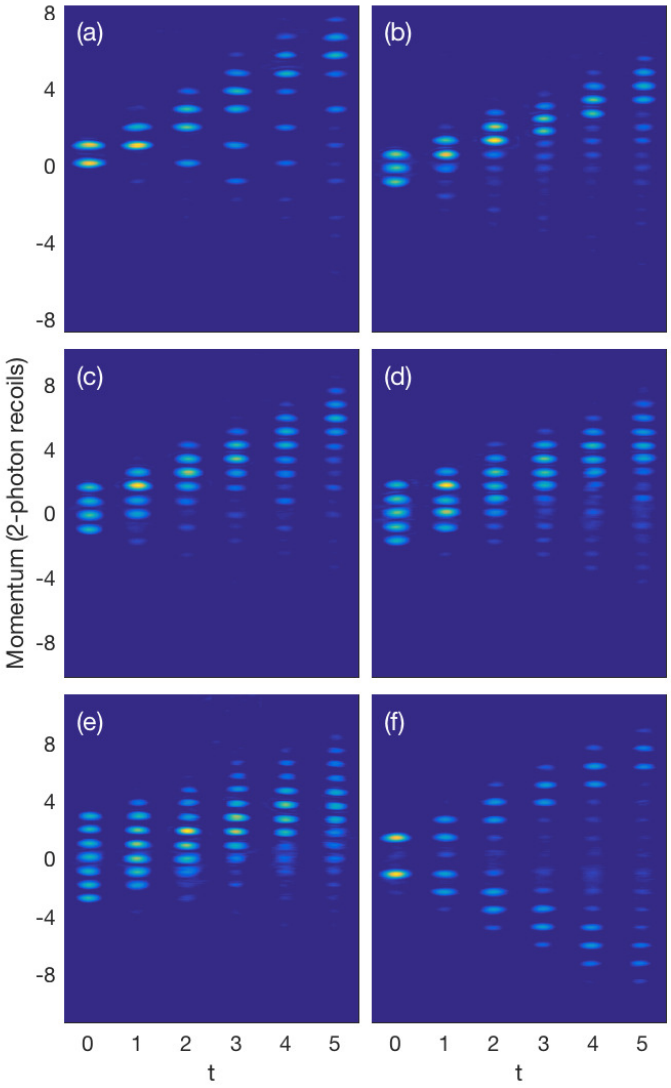

Figure 6.5: Experimental time-of-flight images as a function of t. Overall the relative phases of the momentum components in the initial states were zero. The initial state in (a) was a superposition of two momentum states: $|0\rangle+|1\rangle$. The initial state in (b) was a superposition of three momentum states: $\sum_{n=-1}^{1}|n\rangle$. The initial state in (c) was a superposition of four momentum states: $\sum_{n=-1}^{2}|n\rangle$. The initial state in (d) was a superposition of five momentum states: $\sum_{n=-2}^{2}|n\rangle$. The initial state in (e) was a superposition of seven momentum states: $\sum_{n=-3}^{3}|n\rangle$. The initial state in (f) was a superposition of two momentum states: $|-1\rangle+|1\rangle$. The $t=0$ images show the initial states.

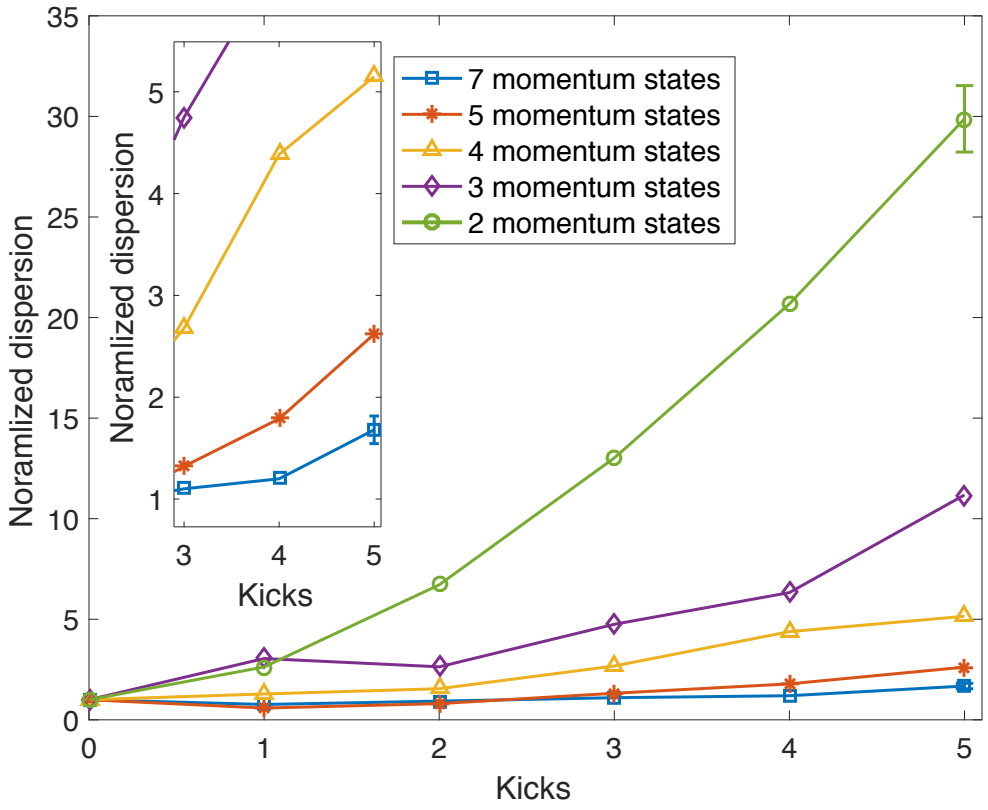

Figure 6.6: Experimental data showing normalized dispersion vs kick number t with the standing wave phase $\gamma = \pi/2$, $\beta = 0.5$, and $T = T_{1/2}$ for initial state $\sum_{n=-3}^{3} |n\rangle$ (squares), initial state $\sum_{n=-2}^{2} |n\rangle$ (asterisks), initial state $\sum_{n=-1}^{2} |n\rangle$ (triangles), initial state $\sum_{n=-1}^{1} |n\rangle$ (diamonds), and initial state $\sum_{n=0}^{1} |n\rangle$ (circles). The inset gives a closer view of the dispersion. Representative error bars are given for: 7 momentum states, kick=5; 2 momentum states, kick=5.

extra phase $\pi/2$ was added to momentum state $|1\rangle$. Figure 6.7 shows that the dispersion grows more quickly when the phase of momentum state $|1\rangle$ differs from the optimal value.

We also investigated the ratchet current using kicks separated by different QR times. In principle kicking pulses separated by $T = 0$ with $\beta = 0$ or $T = T_T$ (Talbot time) with $\beta = 0$ should give the same ratchet current as $T = T_{1/2}$ with $\beta = 0.5$. The experimental results show that with the same initial state, dispersion is smallest with $T = 0$ and largest with $T = T_T$ (see Fig. 6.8). The reason is probably that phase noise from the environment and de-phasing of the initial state are minimized by setting the time $T = 0$. This also supports the observation that the ratchet is sensitive to the phase of the initial state. In addition, the effective finite width in quasi-momentum space can become important as T gets larger. This is because in the ϵ-classical theory, $\epsilon \times \delta\beta$ gives the effective width in quasi-momentum space, so that in case of $T = 0$ $\delta\beta$ is effectively 0 (Wimberger and Sadgrove, 2005). This may have advantages for the practical implementations in interferometry.

Experiments with the initial state $|-1\rangle + |1\rangle$ highly support the idea in Fig. 6.3 that there are two identical peaks appearing at the points of greatest positive and negative gradient. Experimental results in Fig. 6.5(f) show two ratchets with opposite directions. This effect might be applied in atomic interferometry (Mazzoni *et al.*, 2015).

6.5 Conclusions

Experiments were carried out to observe an on-resonant atomic ratchet by exposing an initial atomic state which was a superposition of two or more momentum states to a series of standing wave pulses. We measured the dispersion of the momentum of ratchet current as a function of kick number t. The stronger ratchet current gives a smaller dispersion. We verified that the ratchet current was stronger with a initial state containing more consecutive momentum states. We studied the effect from the phase of the initial state to the ratchet current. A small error on the phase will cause a change in the dispersion which is not negligible. We also performed some other experiments with different time between the

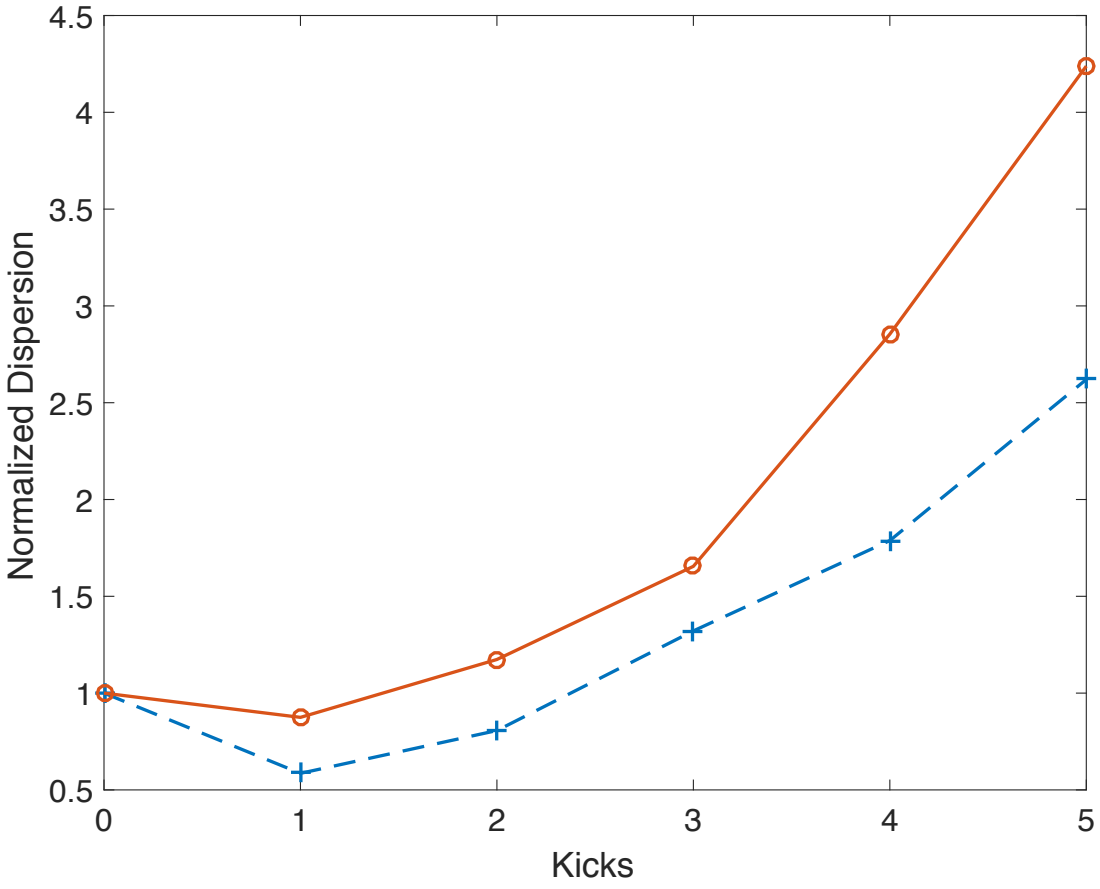

Figure 6.7: Experimental data showing normalized dispersion vs kick number t with the standing wave phase $\gamma = \pi/2$, $\beta = 0$, and $T = T_{T/2}$ for initial state $\sum_{n=-2}^{2} |n\rangle$. The dashed line is for an initial state with optimal phase (net phase on each momentum state is zero). The solid line is for an initial state where the phase of momentum state $|1\rangle$ is $\pi/2$.

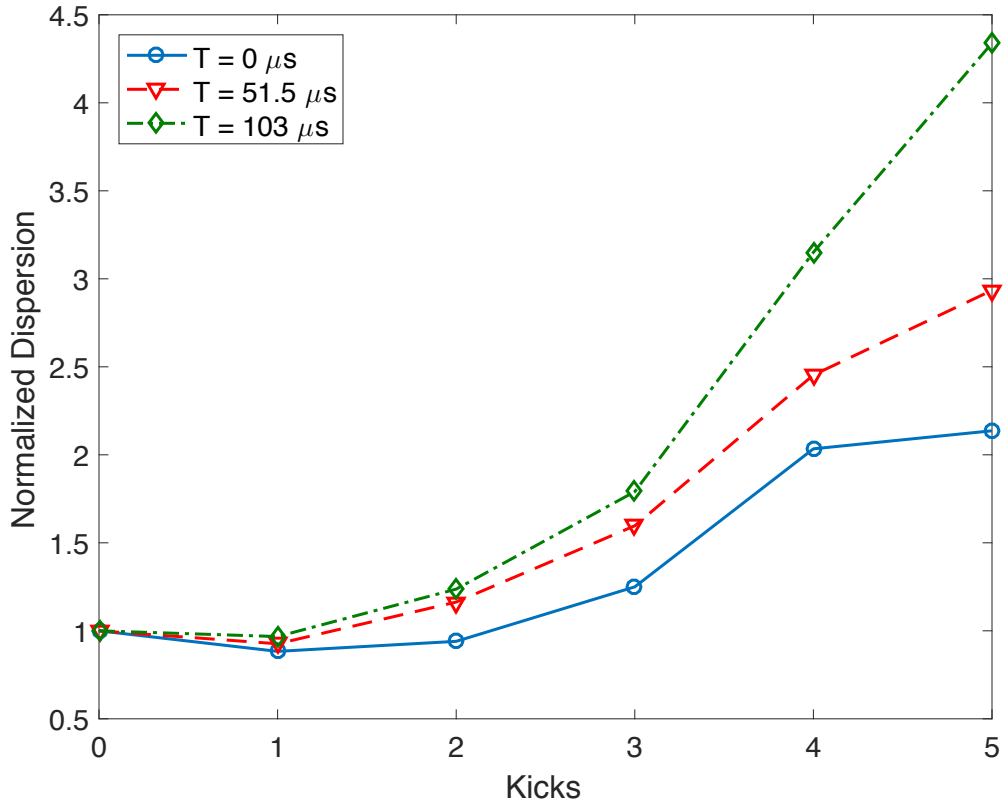

Figure 6.8: Experimental data showing normalized dispersion vs kick number t for initial state $\sum_{n=-2}^{2} |n\rangle$ with the standing wave phase $\gamma = \pi/2$. The solid line is for $\beta = 0$ and $T = 0$. The dashed line is for $\beta = 0.5$ and $T = 51.5$ μs (half-Talbot time). The dash-dot line is for $\beta = 0$ and $T = 103$ μs (Talbot time).

kicking pulses and concluded that shorter time between the pulses was better to minimize perturbation of the environment and re-phasing of the initial state.

CHAPTER VII

CONCLUTION

7.1 Summary

To study the fidelity of quantum state evolution, ϵ-classical maps with different kicking strength was given. It shows that as the kicking strength gets stronger, the area of the island is smaller while the chaotic region gets bigger. Experimentally we introduced a perturbation to the system by applying different kicking strength, the overlapping of the momentum distribution of these two sets of experiments decays with the perturbation. The effect of finite pulse length was also discussed: the fidelity decay rate is proportional to the pulse length.

The theoretical analysis of the intrinsic mechanism of a quantum ratchet illuminates that peaks in the wave function of the initial state containing more than one plane waves arise at positions where the gradient of the standing wave happens to be the greatest. The more of the plane waves, the higher and narrower of the peaks. Experiments were carried out to observe an on-resonant atomic ratchet by exposing an initial atomic state which was a superposition of two or more momentum states to a series of standing wave pulses. We measured the dispersion of the momentum of ratchet current as a function of kick number t. The stronger ratchet current gives a smaller dispersion. We verified that the ratchet current was stronger with an initial state containing more consecutive momentum states. We studied the effect from the phase of the initial state to the ratchet current. A small error

on the phase will cause a change in the dispersion which is not negligible. We also performed some other experiments with different time between the kicking pulses and concluded that shorter time between the pulses was better to minimize perturbation of the environment and re-phasing of the initial state.

7.2 Future work

For the project of the fidelity of quantum state evolution, one of the main objects in the future is to prepare a superposition of two identical initial states for the experiment. In the current experiments, we start from a BEC under identical environment. Though the BECs are the same, we cannot assume that they are in the same initial momentum states in phase space because maps are different with different kicking strength. Therefore the two BECs are not in the same map and are incomparable. In Peres' proposal, the initial states with and without perturbation are the same, which means the experiment should start from the same point on the phase space. For this reason, to prepare a superposition of two BECs simultaneously Bragg pulse may be used in the future. Furthermore, to kick the two BECs simultaneously, two optical standing waves from two pairs of kicking beams will be prepared as well. The second pair of kicking beams will be sent into the vacuum chamber with a different angle between the two beams, thus the grating vector can work on the second BEC. Another thing that needs careful consideration is that the maps shown in Figure 5.1 were drawn assuming ϵ-classical theory. There is a limitation for the ϵ-classical theory's validity which is $|\epsilon| << 1$. For pulse period $T = 70\mu s$, ϵ is 2.26 and is really too large to use ϵ-classical theory. In the future, we will try the very general map without any scaling to plot the dynamics of the atom. We also plan to take more experimental data closer to the Talbot time resonances.

For the on-resonance atomic quantum ratchet which was observed in state $F = 1$, with the slight modification on the existing experimental setup, we have realized that a microwave can be applied between the Bragg pulses and the regular kicking pulses. This microwave can pump half of the atoms to $F = 2$ energy state and keep the rest of the atoms in the $F = 1$

ground state with the same momentum states. By carefully selecting the frequency of the kicking pulses, we can kick the atoms in both $F = 1$ and $F - 2$ states simultaneously. In the imaging procedure, a microwave will be applied again to image the momentum distribution of the atoms in $F = 2$ state. It is interesting of the quantum ratchet for the atoms in $F = 2$ state.

REFERENCES

Allen, Leslie and Joseph H Eberly. *Optical resonance and two-level atoms* (Courier Dover Publications, 2012).

Anderson, Mike H, Jason R Ensher, Michael R Matthews, Carl E Wieman, and Eric A Cornell. "Observation of bose-einstein condensation in a dilute atomic vapor." science **269**, 198–201 (1995).

Astumian, R Dean and Peter Hänggi. "Brownian motors." (2002).

Bagnato, Vanderlei, David E Pritchard, and Daniel Kleppner. "Bose-einstein condensation in an external potential." Physical Review A **35**, 4354 (1987).

Ballot, Buys. *Akustische Versuche auf der Niederlandischen Eisenbahn, nebst gelegentlichen Bemerkungen zur Theorie des Hrn. Prof. Doppler in German*, volume 11 (Annalen der Physik und Chemie, 1845).

Behinaein, G, V Ramareddy, P Ahmadi, and GS Summy. "Exploring the phase space of the quantum δ-kicked accelerator." Physical review letters **97**, 244101 (2006).

Bernath, Peter F. *Spectra of atoms and molecules* (Oxford University Press, 2005).

Bize, S, Y Sortais, MS Santos, C Mandache, A Clairon, and C Salomon. "High-accuracy measurement of the 87rb ground-state hyperfine splitting in an atomic fountain." EPL (Europhysics Letters) **45**, 558 (1999).

Boiron, D, A Michaud, JM Fournier, L Simard, M Sprenger, G Grynberg, and C Salomon. "Cold and dense cesium clouds in far-detuned dipole traps." Physical Review A **57**, R4106 (1998).

Bose, Satyendra Nath. "Plancks gesetz und lichtquantenhypothese." Z. phys **26**, 178 (1924).

Chirikov, Boris V. "A universal instability of many-dimensional oscillator systems." Physics reports **52**, 263–379 (1979).

Chu, Steven, JE Bjorkholm, A Ashkin, and Alex Cable. "Experimental observation of optically trapped atoms." Physical Review Letters **57**, 314 (1986).

Chu, Steven, Leo Hollberg, John E Bjorkholm, Alex Cable, and Arthur Ashkin. "Three-dimensional viscous confinement and cooling of atoms by resonance radiation pressure." Physical Review Letters **55**, 48 (1985).

Dana, I, V Ramareddy, I Talukdar, and GS Summy. "Experimental realization of quantum-resonance ratchets at arbitrary quasimomenta." Physical review letters **100**, 024103 (2008).

Dana, Itzhack and Vladislav Roitberg. "Quantum resonances and ratchets in free-falling frames." Physical Review E **76**, 015201 (2007).

Davis, K B, M O Mewes, M A Joffe, and W Ketterle. "Forteenth international conference on atomic physics." In "Book of Abstracts," volume 1m-7 (1994).

Davis, Kendall B, M-O Mewes, MR van Andrews, NJ Van Druten, DS Durfee, DM Kurn, and Wolfgang Ketterle. "Bose-einstein condensation in a gas of sodium atoms." Physical review letters **75**, 3969 (1995a).

Davis, Kendall B, M-O Mewes, and Wolfgang Ketterle. "An analytical model for evaporative cooling of atoms." Applied Physics B **60**, 155–159 (1995b).

Deng, L, EW Hagley, J Denschlag, JE Simsarian, Mark Edwards, Charles W Clark, K Helmerson, SL Rolston, and WD Phillips. "Temporal, matter-wave-dispersion talbot effect." Physical Review Letters **83**, 5407 (1999).

Doyle, John M, Jon C Sandberg, A Yu Ite, Claudio L Cesar, Daniel Kleppner, and Thomas J Greytak. "Hydrogen in the submillikelvin regime: Sticking probability on superfluid he 4." Physical review letters **67**, 603 (1991).

Einstein, A. "Quantentheorie des einatomigen idealen gases. zweite abhandlung (quantum theory of monatomic ideal gases, part two)." SBd Preuss. Akad. Wiss. Ber **1** (1925).

Einstein, Albert. *Quantentheorie des einatomigen idealen Gases* (Akademie der Wissenshaften, in Kommission bei W. de Gruyter, 1924).

Fishman, Shmuel. "Quantum localisation." Quantum dynamics of simple systems: the Forty-Fourth Scottish Universities Summer School in Physics, Stirling, August 1994 **44**, 115 (1996).

Fishman, Shmuel, Italo Guarneri, and Laura Rebuzzini. "Stable quantum resonances in atom optics." Physical review letters **89**, 084101 (2002).

Fishman, Shmuel, Italo Guarneri, and Laura Rebuzzini. "A theory for quantum accelerator modes in atom optics." Journal of statistical physics **110**, 911–943 (2003).

Gould, PL, PD Lett, and WD Phillips. "New measurements with optical molasses." In "Laser Spectroscopy VIII," pages 64–67 (Springer, 1987).

Greene, John M. "A method for determining a stochastic transition." Journal of Mathematical Physics **20**, 1183–1201 (1979).

Gutzwiller, Martin C. *Chaos in classical and quantum mechanics*, volume 1 (Springer, 1990).

Haake, F. "Quantum signatures of chaos, 1991." (????).

Hess, Harald F. Bull. Am. Phys. Soc. **30**, 854 (1985).

Hess, Harald F. "Evaporative cooling of magnetically trapped and compressed spin-polarized hydrogen." Physical Review B **34**, 3476 (1986).

Hess, Harald F, Greg P Kochanski, John M Doyle, Naoto Masuhara, Daniel Kleppner, and Thomas J Greytak. "Magnetic trapping of spin-polarized atomic hydrogen." Physical review letters **59**, 672 (1987).

Izrailev, Felix M. "Simple models of quantum chaos: spectrum and eigenfunctions." Physics Reports **196**, 299–392 (1990).

Ketterle, Wolfgang, Kendall B Davis, Michael A Joffe, Alex Martin, and David E Pritchard. "High densities of cold atoms in a dark spontaneous-force optical trap." Physical review letters **70**, 2253 (1993).

Kittel, Charles and Paul McEuen. *Introduction to solid state physics*, volume 8 (Wiley New York, 1976).

Kovachy, Tim, Jason M Hogan, David MS Johnson, and Mark A Kasevich. "Optical lattices as waveguides and beam splitters for atom interferometry: An analytical treatment and proposal of applications." Physical Review A **82**, 013638 (2010).

Kuppens, SJM, KL Corwin, KW Miller, TE Chupp, and CE Wieman. "Loading an optical dipole trap." Physical review A **62**, 013406 (2000).

Lepers, Maxence, Véronique Zehnlé, and Jean Claude Garreau. "Kicked-rotor quantum resonances in position space." Physical Review A **77**, 043628 (2008).

Lett, Paul D, Richard N Watts, Christoph I Westbrook, William D Phillips, Phillip L Gould, and Harold J Metcalf. "Observation of atoms laser cooled below the doppler limit." Physical Review Letters **61**, 169 (1988).

Lundh, Emil and Mats Wallin. "Ratchet effect for cold atoms in an optical lattice." Physical review letters **94**, 110603 (2005).

Ma, Z-Y, K Burnett, MB dArcy, and SA Gardiner. "Quantum random walks using quantum accelerator modes." Physical Review A **73**, 013401 (2006).

MacKay, RS. "A renormalization approach to invariant circles in area-preserving maps." Physica D: Nonlinear Phenomena **7**, 283–300 (1983).

Maki, Jeffery J, NS Campbell, CM Grande, RP Knorpp, and DH McIntyre. "Stabilized diode-laser system with grating feedback anf frequency-offset locking." Optics communications **102**, 251–256 (1993).

Mazzoni, T, X Zhang, R Del Aguila, L Salvi, N Poli, and GM Tino. "Large-momentum-transfer bragg interferometer with strontium atoms." Physical Review A **92**, 053619

(2015).

McDowall, P, A Hilliard, M McGovern, T Grünzweig, and MF Andersen. "A fidelity treatment of near-resonant states in the atom-optics kicked rotor." New Journal of Physics **11**, 123021 (2009).

Metcalf, Harold J and Peter Van der Straten. *Laser cooling and trapping* (Springer, 1999).

Migdall, Alan L, John V Prodan, William D Phillips, Thomas H Bergeman, and Harold J Metcalf. "First observation of magnetically trapped neutral atoms." Physical Review Letters **54**, 2596 (1985).

Miller, JD, RA Cline, and DJ Heinzen. "Far-off-resonance optical trapping of atoms." Physical Review A **47**, R4567 (1993).

Monteiro, TS, PA Dando, NAC Hutchings, and MR Isherwood. "Proposal for a chaotic ratchet using cold atoms in optical lattices." Physical review letters **89**, 194102 (2002).

Moore, FL, JC Robinson, C Bharucha, PE Williams, and MG Raizen. "Observation of dynamical localization in atomic momentum transfer: A new testing ground for quantum chaos." Physical review letters **73**, 2974 (1994).

Oberthaler, MK, RM Godun, MB d'Arcy, GS Summy, and K Burnett. "Observation of quantum accelerator modes." Physical review letters **83**, 4447 (1999).

Oskay, WH, DA Steck, BG Klappauf, and MG Raizen. "Quantum chaos with cold cesium atoms." LASER PHYSICS-LAWRENCE- **9**, 265–269 (1999).

Peres, Asher. "Stability of quantum motion in chaotic and regular systems." Physical Review A **30**, 1610 (1984).

Petrich, W, M H Anderson, J R Ensher, and E A Cornell. "Forteenth international conference on atomic physics." In "Book of Abstracts," volume 1m-7 (1994).

Phillips, W D. "Nobel lecture: Laser cooling and trapping of neutral atoms." Rev. Mod. Phys. **70**, 721 (1998).

Raab, EL, M Prentiss, Alex Cable, Steven Chu, and D E Pritchard. "Trapping of neutral sodium atoms with radiation pressure." Physical Review Letters **59**, 2631 (1987).

Ramareddy, V, G Behinaein, I Talukdar, P Ahmadi, and GS Summy. "High-order resonances of the quantum δ-kicked accelerator." EPL (Europhysics Letters) **89**, 33001 (2010).

Ryu, C, MF Andersen, A Vaziri, MB dArcy, JM Grossman, Kristian Helmerson, and WD Phillips. "High-order quantum resonances observed in a periodically kicked bose-einstein condensate." Physical review letters **96**, 160403 (2006).

Sadgrove, Mark, Munekazu Horikoshi, Tetsuo Sekimura, and Ken'ichi Nakagawa. "Coherent control of ballistic energy growth for a kicked bose-einstein condensate." The European Physical Journal D **45**, 229–234 (2007a).

Sadgrove, Mark, Munekazu Horikoshi, Tetsuo Sekimura, and Kenichi Nakagawa. "Rectified momentum transport for a kicked bose-einstein condensate." Physical review letters **99**, 043002 (2007b).

Sadgrove, Mark, Sandro Wimberger, Scott Parkins, and Rainer Leonhardt. "Ballistic and localized transport for the atom optics kicked rotor in the limit of a vanishing kicking period." Physical review letters **94**, 174103 (2005).

Salger, Tobias, Sebastian Kling, Tim Hecking, Carsten Geckeler, Luis Morales-Molina, and Martin Weitz. "Directed transport of atoms in a hamiltonian quantum ratchet." Science **326**, 1241–1243 (2009).

Schanz, Holger, Marc-Felix Otto, Roland Ketzmerick, and Thomas Dittrich. "Classical and quantum hamiltonian ratchets." Physical review letters **87**, 070601 (2001).

Shrestha, Rajendra Kumar. *Application of the atom-optical kicked rotor.* Ph.D. thesis, Oklahoma State University (2013).

Shrestha, RK, WK Lam, J Ni, and GS Summy. "A cold-atom ratchet interpolating between classical and quantum dynamics." Fluctuation and Noise Letters **12**, 1340003 (2013a).

Shrestha, RK, J Ni, WK Lam, GS Summy, and S Wimberger. "Dynamical tunneling of a bose-einstein condensate in periodically driven systems." Physical Review E **88**, 034901 (2013b).

Shrestha, RK, J Ni, WK Lam, S Wimberger, and GS Summy. "Controlling the momentum current of an off-resonant ratchet." Physical Review A **86**, 043617 (2012).

Shrestha, RK, S Wimberger, J Ni, WK Lam, and GS Summy. "Fidelity of the quantum δ-kicked accelerator." Physical Review E **87**, 020902 (2013c).

Silvera, Isaac F and JTM Walraven. "Stabilization of atomic hydrogen at low temperature." Physical Review Letters **44**, 164 (1980).

Stöckmann, HJ. "Quantum chaos: an introduction, 1999." (????).

Summy, Gil and Sandro Wimberger. "Quantum random walk of a bose-einstein condensate in momentum space." Physical Review A **93**, 023638 (2016).

Talukdar, Ishan. *TRANSPORT AND RESONANCES IN KICKED BOSE-EINSTEIN CONDENSATES*. Ph.D. thesis, Oklahoma State University (2010).

Talukdar, Ishan, Rajendra Shrestha, and GS Summy. "Sub-fourier characteristics of a δ-kicked-rotor resonance." Physical review letters **105**, 054103 (2010).

Torii, Yoshio, Yoichi Suzuki, Mikio Kozuma, Toshiaki Sugiura, Takahiro Kuga, Lu Deng, and EW Hagley. "Mach-zehnder bragg interferometer for a bose-einstein condensate." Physical Review A **61**, 041602 (2000).

Ullah, Arif and MD Hoogerland. "Experimental observation of loschmidt time reversal of a quantum chaotic system." Physical Review E **83**, 046218 (2011).

Wickenbrock, Arne, David Cubero, NA Abdul Wahab, P Phoonthong, and Ferruccio Renzoni. "Current reversals in a rocking ratchet: The frequency domain." Physical Review E **84**, 021127 (2011).

Wimberger, Sandro, Riccardo Mannella, Oliver Morsch, and Ennio Arimondo. "Resonant nonlinear quantum transport for a periodically kicked bose condensate." Physical review letters **94**, 130404 (2005).

Wimberger, Sandro and Mark Sadgrove. "The role of quasi-momentum in the resonant dynamics of the atom-optics kicked rotor." Journal of Physics A: Mathematical and General **38**, 10549 (2005).

Wu, Huang and Christopher J Foot. "Direct simulation of evaporative cooling." Journal of Physics B: Atomic, Molecular and Optical Physics **29**, L321 (1996).

Ye, Jun, Steve Swartz, Peter Jungner, and John L Hall. "Hyperfine structure and absolute frequency of the 87 rb 5p 3/2 state." Optics letters **21**, 1280–1282 (1996).

APPENDIX A

STATE DEPENDENCE OF QUANTUM RATCHETS

Initial-state dependence of a quantum resonance ratchet

Jiating Ni,[1] Wa Kun Lam,[1] Siamak Dadras,[1] Mario F. Borunda,[1] Sandro Wimberger,[2,3,4] and Gil S. Summy[1]
[1]*Department of Physics, Oklahoma State University, Stillwater, Oklahoma 74078-3072, USA*
[2]*DiFeST, Università degli Studi di Parma, Parco delle Scienze, 7/A, 43124 Parma, Italy*
[3]*INFN, Sezione di Milano Bicocca, Gruppo Collegato di Parma, Parma, Italy*
[4]*ITP, Heidelberg University, Philosophenweg 12, 69120 Heidelberg, Germany*
(Received 1 September 2016; published 11 October 2016)

We demonstrate quantum resonance ratchets created with Bose-Einstein condensates exposed to pulses of an off-resonant standing light wave. We show how some of the basic properties of the ratchets are controllable through the creation of different initial states of the system. In particular, our results prove that through an appropriate choice of initial state it is possible to reduce the extent to which the ratchet state changes with respect to time. We develop a simple theory to explain our results and indicate how ratchets might be used as part of a matter-wave interferometer or quantum random walk experiment.

DOI: 10.1103/PhysRevA.94.043620

I. INTRODUCTION

Understanding the nature of quantum transport is an important problem for quantum chaos and for many condensed matter systems [1]. The δ-kicked rotor is an ideal system for studying quantum transport and can be realized by exposing a sample of cold atoms to short pulses of an optical standing wave. This is the so-called atom optics quantum kicked rotor (AOQKR) [2]. The implementation of the AOQKR in experiments was a breakthrough in the study of quantum chaos, and the system has now been widely used in elucidating phenomena like dynamical localization [2], quantum resonances (QRs) [2–4], quantum accelerator modes (QAMs) [5–10], fidelity [11–14], and quantum ratchets [15–24]. In contrast to Brownian ratchets [25], quantum ratchets do not experience dissipative processes or a net biasing force [26]. Hence these systems have been proposed as the basis for a Hamiltonian quantum ratchet [18]. In previous experimental observations of quantum ratchets [16,25,27,28], it was found that only a relatively small component of the initial wave function contributed to the ratchet current. It is therefore natural to ask if it is possible to improve the mode matching between the initial state of a system and the ratchet state so as to increase the participation in the ratchet. This could be important for applications in atom optics such as interferometry. Our motivation for enhancing the efficiency of the quantum ratchet is the possible use of such a system as the walk component in experiments on quantum random walks [29–31].

The structure of this paper is as follows: we begin by providing a theoretical analysis of the intrinsic mechanism of a quantum ratchet. This includes the development of a simple classical picture that can explain many of the features of the ratchet. We then present the experimental realization of the momentum currents using initial states that have been prepared using Bragg diffraction with light pulses. We demonstrate how different phases on the initial-state wave function can affect the momentum current and examine how the momentum current depends on the number of momentum states in the initial wave function. In particular, we present results showing a connection between the number of momentum-state components and the "dispersion" of the ratchet.

II. THEORY

We start by summarizing the basic dynamics of the AOQKR system. The Hamiltonian in dimensionless units is given by [32]

$$\hat{H} = \frac{\hat{p}^2}{2} + \phi_d V(\hat{x}) \sum_{t=1}^{N} \delta(t' - t\tau), \tag{1}$$

where $\hat{p}$ is the scaled momentum in units of $\hbar G$ (two photon recoils) and ϕ_d is the strength of the kicks and is given by $\phi_d = \Omega^2 \triangle t / 8\delta_L$, where $\triangle t$ is pulse length, $\Omega = \vec{\mu} \cdot \vec{E}(\vec{r})/\hbar$ is the Rabi frequency, and δ_L is the detuning of the kicking laser from the atomic transition. $V(\hat{x}) = \cos(Gx + \gamma)$ is the potential created by a standing wave with a grating vector $G = 2\pi/\lambda_G$. λ_G is the spatial period of the standing wave and is determined by the direction of the laser beams and their wavelength. Here, x is position, and γ is an offset phase; t' is the continuous time variable, and t counts the number of kicks; $\tau = 2\pi T/T_{1/2}$ is the scaled pulse period where T is the real pulse period and $T_{1/2} = 2\pi M/\hbar G^2$ is the half-Talbot time for an atom with mass M. The momentum is changed in quanta of $\hbar G$ in this system, and as a result p can be broken down as $p = n + \beta$, where n and β are the integer and fractional parts of the momentum, respectively. β, known as the quasimomentum, is a conserved quantity [33].

A convenient picture of the ratchet mechanism can be derived by considering the gradient of the standing wave as the driving force on the wave function. From this standpoint ensuring that the wave function is maximized near positions with larger gradients in the potential should produce a net force and hence the possibility of a ratchet. In this picture the sign of the potential gradient near the wave function's maxima will determine the ratchet's direction. One way to create a spatially nonuniform atomic wave function is to use an initial state that is comprised of a superposition of two or more plane waves: $|\psi\rangle = \sum_n e^{in\pi/2}|n\rangle$, where $|n\rangle$ refers to the state $|n\hbar G\rangle$. As will be seen shortly, the phase prefactors shift the maxima of the spatial wave function to where the potential gradient is greatest.

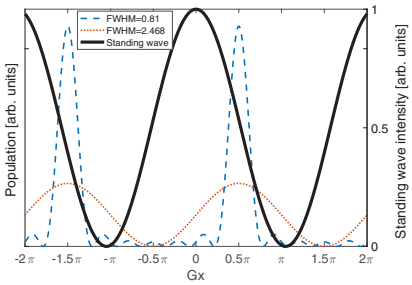

FIG. 1. The solid line is the standing-wave intensity for potential $V(x)$. The dashed line is the wave function for a superposition of seven plane waves: $\sum_{n=-3}^{3} e^{-in\pi/2}|n\rangle$. The dotted line is the wave function for a superposition of two plane waves: $|0\rangle + e^{i\pi/2}|1\rangle$.

Considering the case of a single Bose-Einstein condensate (BEC) for the initial state, the wave function in momentum space can be written as $\psi(p) = \delta(p)$ assuming the BEC has a narrow momentum width. Here p is the continuous momentum variable. In order to study the wave function in the frame of the standing wave, we transform it into position space by using a Fourier transformation. The magnitude of the wave function in position space is $|\phi(x)| = \sqrt{G/2\pi}$. Since this is uniform in x, the average force is zero and according to the simple picture described above no ratchet is formed.

When the initial state contains two or more plane waves, the wave function in position space can be written as

$$\phi(x) = A \sum_{n} e^{-in\pi/2} e^{ip_n x/\hbar}, \tag{2}$$

where A is the normalization factor. By plotting $|\phi(x)|^2$ and the standing-wave potential together, it is noticeable that peaks of the wave function arise at positions where the gradient of the standing wave happens to be the greatest (see Fig. 1). Naturally, the more plane waves composing the initial state, the more localized the wave function should become. In Fig. 1, the bold solid line is the standing wave, and the dashed and dotted lines are the wave functions for the initial states with a superposition of seven plane waves, $\sum_{n=-3}^{3} e^{-in\pi/2}|n\rangle$, and two plane waves, $|0\rangle + e^{i\pi/2}|1\rangle$, respectively. The dashed line is much taller and has a reduced full width at half maximum (FWHM). Figure 2 shows that, as the number of consecutive plane waves in the initial state increases, the corresponding FWHM of the wave function decreases. Since a peak with larger FWHM experiences a smaller overall gradient and a larger variation in the gradient, we expect that a "cleaner" ratchet will require more plane waves in the initial superposition. The effective force $F_{\text{eff}} = \int_{-\pi}^{\pi} |\phi(x)|^2 dV(x)$ of the standing wave (integrate the absolute square of wave function with the standing-wave gradient) for different initial states was also calculated. The dashed line in Fig. 2 shows that F_{eff} increases with the number of the plane waves in the initial state.

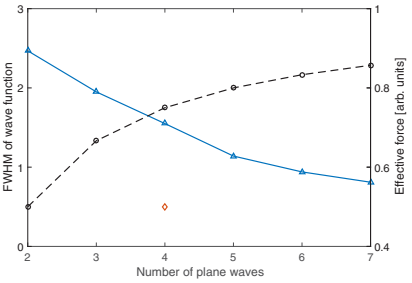

FIG. 2. The solid line is the theoretical full width at half maximum (FWHM) of the wave function in position space vs the number of plane waves, while the dashed line is the theoretical effective force of the standing wave. The diamond is the magnitude of effective force for the initial state $e^{-i\pi}|-2\rangle + e^{-i\pi/2}|-1\rangle + e^{i\pi/2}|1\rangle + e^{i\pi}|2\rangle$. Note that in this case the $n = 0$ state is missing.

To ensure the peak of the wave function appears at a position that will maximize F_{eff} (in this case $Gx = \pi/2$), the phase for each plane wave is extremely important. For this reason the phases should be set to $e^{in\pi/2}$, where n is the momentum-state index. If the phases differ from these values the peak of the wave function in position space will shift away from the greatest gradient and the effective force will become weaker. We also point out that to maximize the ratchet, the momentum states in the initial superposition should be consecutive. In other words, the momentum difference between neighboring momentum states should be $\hbar G$. Figure 3 shows the wave function in position space for initial states with a superposition of nonconsecutive momentum states. Note that besides the

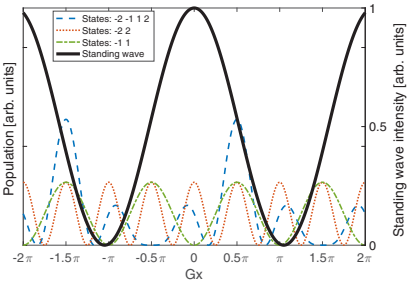

FIG. 3. The solid line is the standing-wave intensity for potential $V(x)$. The dashed line is the wave function for a superposition of nonconsecutive plane waves: $e^{-i\pi}|-2\rangle + e^{-i\pi/2}|-1\rangle + e^{i\pi/2}|1\rangle + e^{i\pi}|2\rangle$. The dotted line is the wave function for a superposition of nonconsecutive plane waves: $e^{-i\pi}|-2\rangle + e^{i\pi}|2\rangle$. The dash-dotted line is the wave function for a superposition of nonconsecutive plane waves: $e^{-i\pi/2}|-1\rangle + e^{i\pi/2}|1\rangle$.

wave function peak at the greatest gradient point, there is also considerable wave-function amplitude at positions where the gradient is zero or of opposite sign. This can provide an explanation for why the ratchet is weak or even absent in experiments with these initial states. The dashed line represents the initial state, $e^{-i\pi}|-2\rangle + e^{-i\pi/2}|-1\rangle + e^{i\pi/2}|1\rangle + e^{i\pi}|2\rangle$, and shows a relatively large peak at the greatest gradient point. Thus the ratchet effect should still exist, although it is weaker than the ratchet from an initial state with four consecutive momentum states. This can be seen in Fig. 2, where the diamond indicates F_{eff} for this state. In Fig. 3 the dotted line represents the initial state: $e^{-i\pi}|-2\rangle + e^{i\pi}|2\rangle$. This has $F_{\text{eff}} = 0$. Finally, the dash-dotted line is for the initial state: $e^{-i\pi/2}|-1\rangle + e^{i\pi/2}|1\rangle$. Note that two wave-function peaks appear at points where the positive and negative gradient is greatest on the standing wave. This suggests that we should expect two simultaneous ratchets with opposite directions.

III. EXPERIMENTAL SETUP

Our experimental apparatus is similar to the one described in Ref. [24]. A BEC with about 70 000 ^{87}Rb atoms was created in the $5S_{1/2}$, $F = 1$ hyperfine ground states in a focused CO_2 laser beam using an all-optical trapping technique [34]. The ratio of the mean-field energy to the recoil energy is approximatively 1×10^{-5}, which puts us in the region where the nonlinearity has a negligible effect on the dynamics. Immediately after the BEC was released from the trap, we applied a series of horizontal optical standing-wave pulses. The standing wave was formed by two laser beams with a wavelength of $\lambda = 780$ nm, which was 6.8 GHz red-detuned from the $5S_{1/2}, F = 1 \longrightarrow 5P_{3/2}, F' = 3$ transition. Each laser beam was aligned 53° from the vertical to give a standing-wave spatial period of $\lambda_G = \lambda/(2\sin 53°)$. This led to a half-Talbot time of $T_{1/2} \approx 51.5\,\mu$s, with the primary QRs falling at integer multiples of this time [3]. To create the necessary standing-wave pulses, we controlled the phase, intensity, pulse length, and relative frequency between the two laser beams. This was achieved by passing each of the standing wave's constituent laser beams through an acousto-optic modulator (AOM) driven by an arbitrary waveform generator. The nodes of the standing wave moved with a velocity given by $v = 2\pi\Delta f/G$ with Δf being the frequency difference between the two beams. The momentum of the BEC, p, relative to the standing wave is proportional to v and therefore p can be controlled through Δf. The kicking pulse length was fixed at 600 ns to ensure that the experiments were performed in the Raman-Nath regime [35,36]. In other words, the evolution of the wave function due to its kinetic energy is ignored during the pulse.

To prepare an initial state comprised of a superposition of several plane waves, a sequence of longer standing-wave pulses were applied in the Bragg configuration [37]. Such pulses connect two momentum states with an interaction matrix given by

$$U = \begin{pmatrix} \cos\left(\frac{\Omega_B \tau_B}{2}\right) & -i\sin\left(\frac{\Omega_B \tau_B}{2}\right)\exp(i\gamma_B) \\ -i\sin\left(\frac{\Omega_B \tau_B}{2}\right)\exp(-i\gamma_B) & \cos\left(\frac{\Omega_B \tau_B}{2}\right) \end{pmatrix}, \tag{3}$$

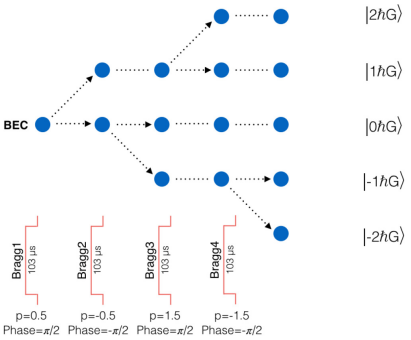

FIG. 4. Experimental schematic showing preparation of the five-component initial state: $\sum_{n=-2}^{2}|n\rangle$.

where Ω_B is the effective Rabi frequency, τ_B is the Bragg pulse length, and γ_B is the offset phase of the standing wave used for a Bragg pulse. To understand how Bragg pulses were utilized in our experiment, consider the preparation of a superposition of five momentum states. Figure 4 shows the procedure for creating this superposition. In the first setup a Bragg pulse with $p = 0.5$ diffracts atoms from $|0\rangle$ to $|1\rangle$. The second Bragg pulse with $p = -0.5$ diffracts atoms from $|0\rangle$ to $|-1\rangle$ without affecting the atoms in state $|1\rangle$. Similarly, the third and fourth Bragg pulses, with $p = 1.5$ and $p = -1.5$, diffract atoms from $|1\rangle$ to $|2\rangle$ and from $|-1\rangle$ to $|-2\rangle$, respectively. All of the Bragg pulses were applied consecutively without dwell time between the pulses. There is considerable freedom in the choice of pulse length; however, in our case this was set at 103 μs or 1× Talbot time. This ensured that the free evolution of each of the prepared states was always $\hat{1}$ during the application of subsequent Bragg pulses. The intensity for the different pulses was carefully adjusted to make the population in each state equal. We implemented preparation schemes like this for superpositions comprising up to seven states. The relative phases between the Bragg prepared states are critically important to the dynamics of the ratchet. We performed the experiments so that all of the phases of the states in the superposition were identical. This was achieved by setting $\gamma_B = -\pi/2$ or $\gamma_B = \pi/2$ depending on whether we were coupling states with $\Delta n = -1$ or $\Delta n = 1$, respectively.

Following the Bragg preparation, the δ-like kick rotor pulses were immediately applied. These diffracted the atoms into a wide range of momentum states. For the kicking pulses, the pulse strength $\phi_d \sim 1.4$, and the phase γ in the potential was $\pi/2$. This is mathematically equivalent to individually setting the phases of the initial momentum states to be $e^{in\pi/2}$, which is required to maximize the ratchet. For all but a few experiments, the time between kicking pulses was 51.5 μs (half-Talbot time) with initial momentum $\beta = 0.5$ to maintain QR. In order to measure the momentum distribution after the pulse sequence, atoms were absorption imaged following a free

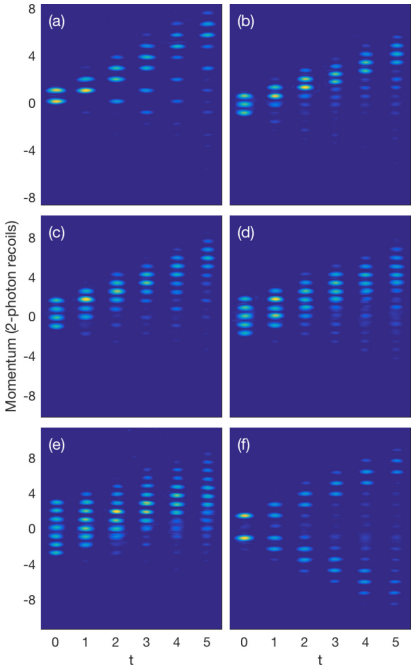

FIG. 5. Experimental time-of-flight images as a function of t. The relative phases of the momentum components in the initial states were zero. The initial states were (a) $|0\rangle + |1\rangle$, (b) $\sum_{n=-1}^{1} |n\rangle$, (c) $\sum_{n=-1}^{2} |n\rangle$, (d) $\sum_{n=-2}^{2} |n\rangle$, (e) $\sum_{n=-3}^{3} |n\rangle$, and (f) $|-1\rangle + |1\rangle$. In each case the $t = 0$ images show the initial state. Panels (a)–(e) show the single ratchets with positive directed currents. In (f) a symmetric double ratchet is seen.

flight time of 9 ms. Several examples of time-of-flight images of the BEC vs t are shown in Fig. 5. Of particular note is the experiment with the initial state $|-1\rangle + |1\rangle$ [Fig. 5(f)]. These data highly support the idea from Fig. 3 that the two identical peaks appearing at the points of greatest positive and negative gradient should produce two ratchets with opposite directions. This effect might be applied in atomic interferometry as a beam splitter [38].

As can be seen from the previous discussion, the phases of the components of the superposition are extremely important for the ratchet dynamics. Hence it is critical that any unwanted phases be controlled and if possible eliminated. To this end we implemented a Mach-Zehnder Bragg interferometer [37] with which we could measure such phases. In particular, we were able to reduce extraneous phase shifts due to gravity

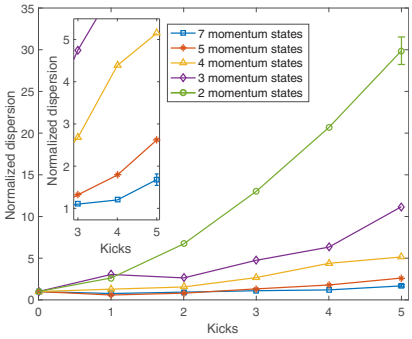

FIG. 6. Experimental data showing normalized dispersion vs kick number t with $\beta = 0.5$ and $T = T_{1/2}$ for initial states $\sum_{n=-3}^{3} |n\rangle$ (squares), $\sum_{n=-2}^{2} |n\rangle$ (asterisks), $\sum_{n=-1}^{2} |n\rangle$ (triangles), $\sum_{n=-1}^{1} |n\rangle$ (diamonds), and $\sum_{n=0}^{1} |n\rangle$ (circles). The inset gives a closer view of the dispersion. Representative error bars are given for seven momentum states, five kicks; two momentum states, five kicks.

(nonhorizontal standing wave) and ac Stark shifts (due to small amounts of stray light) to levels where they were insignificant for the ratchet experiment.

IV. DATA ANALYSIS AND DISCUSSION

A large part of the motivation for the work presented here is to understand the behavior of ratchets with different initial states. To this end we have performed a comprehensive

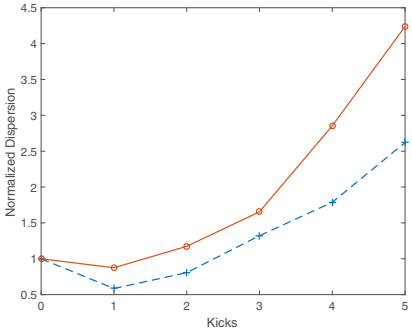

FIG. 7. Experimental data showing normalized dispersion vs kick number t with $\beta = 0.5$ and $T = T_{1/2}$ for initial state $\sum_{n=-2}^{2} |n\rangle$. The dashed line is for an initial state with optimal phase (net phase on each momentum state is zero). The solid line is for an initial state where the phase of momentum state $|1\rangle$ is $\pi/2$.

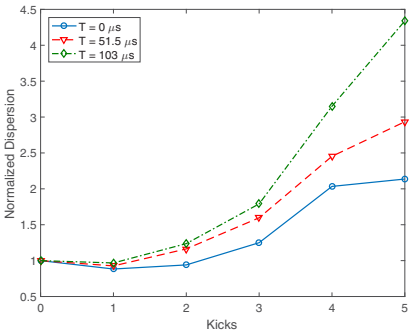

FIG. 8. Experimental data showing normalized dispersion vs kick number t for initial state $\sum_{n=-2}^{2}|n\rangle$ with the standing-wave phase $\gamma = \pi/2$. The solid line is for $\beta = 0$ and $T = 0$. The dashed line is for $\beta = 0.5$ and $T = 51.5\,\mu$s (half-Talbot time). The dash-dotted line is for $\beta = 0$ and $T = 103\,\mu$s (Talbot time).

experimental study of the "dispersion" of a ratchet as a function of several variables. We define the normalized dispersion of a ratchet as

$$D(t) = \frac{\langle p_t^2\rangle - \langle p_t\rangle^2}{\langle p_0^2\rangle - \langle p_0\rangle^2}, \tag{4}$$

where $\langle p_t\rangle$ is the mean momentum, $\langle p_t^2\rangle$ is the mean of momentum squared, and t is the kick number ($t = 0$ corresponds to the initial distribution). The dispersion is an objective way of describing the "quality" of the ratchet current: the closer $D(t)$ is to 1 the closer the ratchet state resembles its initial form. Reducing the amount by which the dispersion increases can be important for applications, such as realizing quantum random walks [30]. We now examine the sensitivity of the ratchet current dispersion to the initial state. Figure 6 shows the dependence of the dispersion on kick number t for $\beta = 0.5$ and $T = T_{1/2}$. The experimental results are in line with what we would expect by looking at the wave-function plots in Fig. 1 and show that a larger number of momentum states in the initial state produces a smaller dispersion. In other words, to improve the quality of the ratchet we need to generate an initial state with a large number of plane waves in its superposition.

As discussed before, the ratchet is sensitive to the phases in the initial state. To illustrate this point, experiments were carried out with an initial state $\sum_{n=-2}^{2}|n\rangle$ in which an extra phase $\pi/2$ was added to momentum state $|1\rangle$. Figure 7 shows that the dispersion grows more quickly when the phase of momentum state $|1\rangle$ differs from the optimal value.

We also investigated the ratchet current using kicks separated by different QR times. In principle, kicking pulses separated by $T = 0$ with $\beta = 0$ or $T = T_T$ (Talbot time) with $\beta = 0$ should give the same ratchet current as $T = T_{1/2}$ with $\beta = 0.5$. The experimental results show that, with the same initial state, dispersion is smallest with $T = 0$ and largest with $T = T_T$ (see Fig. 8). The reason is probably that phase noise from the environment and dephasing of the initial state ($\Delta\beta$, the width of the initial state, is small but not zero and results in phase evolution during T) are minimized by setting the $T = 0$ [39]. This is supported by the observation that the ratchet is sensitive to the phase of the initial state.

V. CONCLUSIONS

Experiments were carried out to create an on-resonant atomic ratchet by exposing an initial atomic state which was a superposition of two or more momentum states to a series of standing-wave pulses. A picture that we used to understand many of the features of the ratchet considers the effective force produced by the standing-wave pulses. When more than one plane wave is present in the initial state this force can be nonzero. We defined and measured the dispersion of the momentum of the ratchet current as a function of kick number t. It was verified that the ratchet dispersion grew more slowly when the initial state contained a large number of consecutive momentum states. We studied the effect from the phase of the initial state to the ratchet current. A small error in the phase causes a change in the dispersion which is not negligible. We also performed experiments with different times between the kicking pulses and concluded that shorter times between were better so as to minimize perturbations from the environment that cause dephasing of ratchet states. We hope that this work will provide the basis for further studies of ratchets, particularly as they pertain to their application for experiments with quantum random walks.

ACKNOWLEDGMENTS

We thank J. Clark and A. Sundararaj for helpful comments and discussions.

[1] C. W. J. Beenakker, Rev. Mod. Phys. **69**, 731 (1997).
[2] F. L. Moore, J. C. Robinson, C. Bharucha, P. E. Williams, and M. G. Raizen, Phys. Rev. Lett. **73**, 2974 (1994).
[3] C. Ryu, M. F. Andersen, A. Vaziri, M. B. d'Arcy, J. M. Grossman, K. Helmerson, and W. D. Phillips, Phys. Rev. Lett. **96**, 160403 (2006).
[4] F. M. Izrailev, Phys. Rep. **196**, 299 (1990).
[5] S. Fishman, I. Guarneri, and L. Rebuzzini, Phys. Rev. Lett. **89**, 084101 (2002).
[6] S. Fishman, I. Guarneri, and L. Rebuzzini, J. Stat. Phys. **110**, 911 (2003).
[7] G. Behinaein, V. Ramareddy, P. Ahmadi, and G. S. Summy, Phys. Rev. Lett. **97**, 244101 (2006).
[8] V. Ramareddy, G. Behinaein, I. Talukdar, P. Ahmadi, and G. S. Summy, Europhys. Lett. **89**, 33001 (2010).
[9] M. K. Oberthaler, R. M. Godun, M. B. d'Arcy, G. S. Summy, and K. Burnett, Phys. Rev. Lett. **83**, 4447 (1999).
[10] R. K. Shrestha, J. Ni, W. K. Lam, G. S. Summy, and S. Wimberger, Phys. Rev. E **88**, 034901 (2013).

[11] P. McDowall, A. Hilliard, M. McGovern, T. Grünzweig, and M. F. Andersen, New J. Phys. **11**, 123021 (2009).
[12] A. Ullah and M. D. Hoogerland, Phys. Rev. E **83**, 046218 (2011).
[13] R. K. Shrestha, S. Wimberger, J. Ni, W. K. Lam, and G. S. Summy, Phys. Rev. E **87**, 020902(R) (2013).
[14] I. Talukdar, R. Shrestha, and G. S. Summy, Phys. Rev. Lett. **105**, 054103 (2010).
[15] T. S. Monteiro, P. A. Dando, N. A. C. Hutchings, and M. R. Isherwood, Phys. Rev. Lett. **89**, 194102 (2002).
[16] I. Dana, V. Ramareddy, I. Talukdar, and G. S. Summy, Phys. Rev. Lett. **100**, 024103 (2008).
[17] M. Sadgrove, M. Horikoshi, T. Sekimura, and K. Nakagawa, Eur. Phys. J. D **45**, 229 (2007).
[18] T. Salger, S. Kling, T. Hecking, C. Geckeler, L. Morales-Molina, and M. Weitz, Science **326**, 1241 (2009).
[19] R. D. Astumian and P. Hänggi, Phys. Today **55**(11), 33 (2002).
[20] E. Lundh and M. Wallin, Phys. Rev. Lett. **94**, 110603 (2005).
[21] A. Wickenbrock, D. Cubero, N. A. Abdul Wahab, P. Phoonthong, and F. Renzoni, Phys. Rev. E **84**, 021127 (2011).
[22] R. K. Shrestha, W. K. Lam, J. Ni, and G. S. Summy, Fluctuation Noise Lett. **12**, 1340003 (2013).
[23] H. Schanz, M.-F. Otto, R. Ketzmerick, and T. Dittrich, Phys. Rev. Lett. **87**, 070601 (2001).
[24] S. Flach, O. Yevtushenko, and Y. Zolotaryuk, Phys. Rev. Lett. **84**, 2358 (2000).
[25] M. Sadgrove, M. Horikoshi, T. Sekimura, and K. Nakagawa, Phys. Rev. Lett. **99**, 043002 (2007).
[26] P. Reimann, M. Grifoni, and P. Hänggi, Phys. Rev. Lett. **79**, 10 (1997).
[27] R. K. Shrestha, J. Ni, W. K. Lam, S. Wimberger, and G. S. Summy, Phys. Rev. A **86**, 043617 (2012).
[28] D. H. White, S. K. Ruddell, and M. D. Hoogerland, Phys. Rev. A **88**, 063603 (2013).
[29] Z.-Y. Ma, K. Burnett, M. B. d'Arcy, and S. A. Gardiner, Phys. Rev. A **73**, 013401 (2006).
[30] G. S. Summy and S. Wimberger, Phys. Rev. A **93**, 023638 (2016).
[31] M. Weiß, C. Groiseau, W. K. Lam, R. Burioni, A. Vezzani, G. S. Summy, and S. Wimberger, Phys. Rev. A **92**, 033606 (2015).
[32] R. Graham, M. Schlautmann, and P. Zoller, Phys. Rev. A **45**, R19 (1992).
[33] M. Sadgrove and S. Wimberger, Adv. At. Mol. Opt. Phys. **60**, 315 (2011).
[34] M. D. Barrett, J. A. Sauer, and M. S. Chapman, Phys. Rev. Lett. **87**, 010404 (2001).
[35] C. V. Raman and N. S. N. Nath, Proc. Indian Acad. Sci. **4**, 222 (1936).
[36] P. L. Gould, G. A. Ruff, and D. E. Pritchard, Phys. Rev. Lett. **56**, 827 (1986).
[37] M. Kozuma, L. Deng, E. W. Hagley, J. Wen, R. Lutwak, K. Helmerson, S. L. Rolston, and W. D. Phillips, Phys. Rev. Lett. **82**, 871 (1999).
[38] T. Mazzoni, X. Zhang, R. Del Aguila, L. Salvi, N. Poli, and G. M. Tino, Phys. Rev. A **92**, 053619 (2015).
[39] S. Wimberger and M. Sadgrove, J. Phys. A: Math. Gen. **38**, 10549 (2005).

VITA

JIATING NI

Candidate for the Degree of

Doctor of Philosophy

Thesis: STATE DEPENDANCE OF QUANTUM RATCHETS

Major Field: Physics

Biographical:

Education:

Completed the requirements for the Doctor of Philosophy in physics at Oklahoma State University, Stillwater, Oklahoma in July, 2016.

Completed the requirements for the Maser of Science in physics at Hangzhou Normal University, Hangzhou, Zhejiang, China in 2009.

Completed the requirements for the Bachelor of Science in physics at Zhejiang Normal University, Jinhua, Zhejiang, China in 2005.

Professional Memberships:

American Physical Society